NASA/CR—2003-212291

Propulsion Health Monitoring for Enhanced Safety

Mark G. Butz
General Electric Company, Aircraft Engines, Cincinnati, Ohio

Héctor M. Rodríguez
General Electric Company, Global Research, Niskayuna, New York

June 2003

The NASA STI Program Office . . . in Profile

Since its founding, NASA has been dedicated to the advancement of aeronautics and space science. The NASA Scientific and Technical Information (STI) Program Office plays a key part in helping NASA maintain this important role.

The NASA STI Program Office is operated by Langley Research Center, the Lead Center for NASA's scientific and technical information. The NASA STI Program Office provides access to the NASA STI Database, the largest collection of aeronautical and space science STI in the world. The Program Office is also NASA's institutional mechanism for disseminating the results of its research and development activities. These results are published by NASA in the NASA STI Report Series, which includes the following report types:

- TECHNICAL PUBLICATION. Reports of completed research or a major significant phase of research that present the results of NASA programs and include extensive data or theoretical analysis. Includes compilations of significant scientific and technical data and information deemed to be of continuing reference value. NASA's counterpart of peer-reviewed formal professional papers but has less stringent limitations on manuscript length and extent of graphic presentations.

- TECHNICAL MEMORANDUM. Scientific and technical findings that are preliminary or of specialized interest, e.g., quick release reports, working papers, and bibliographies that contain minimal annotation. Does not contain extensive analysis.

- CONTRACTOR REPORT. Scientific and technical findings by NASA-sponsored contractors and grantees.

- CONFERENCE PUBLICATION. Collected papers from scientific and technical conferences, symposia, seminars, or other meetings sponsored or cosponsored by NASA.

- SPECIAL PUBLICATION. Scientific, technical, or historical information from NASA programs, projects, and missions, often concerned with subjects having substantial public interest.

- TECHNICAL TRANSLATION. English-language translations of foreign scientific and technical material pertinent to NASA's mission.

Specialized services that complement the STI Program Office's diverse offerings include creating custom thesauri, building customized databases, organizing and publishing research results . . . even providing videos.

For more information about the NASA STI Program Office, see the following:

- Access the NASA STI Program Home Page at ***http://www.sti.nasa.gov***

- E-mail your question via the Internet to help@sti.nasa.gov

- Fax your question to the NASA Access Help Desk at 301–621–0134

- Telephone the NASA Access Help Desk at 301–621–0390

- Write to:
  NASA Access Help Desk
  NASA Center for AeroSpace Information
  7121 Standard Drive
  Hanover, MD 21076

NASA/CR—2003-212291

Propulsion Health Monitoring for Enhanced Safety

Mark G. Butz
General Electric Company, Aircraft Engines, Cincinnati, Ohio

Héctor M. Rodríguez
General Electric Company, Global Research, Niskayuna, New York

Prepared under Contract NAS3–99203

National Aeronautics and
Space Administration

Glenn Research Center

June 2003

Available from

NASA Center for Aerospace Information
7121 Standard Drive
Hanover, MD 21076

National Technical Information Service
5285 Port Royal Road
Springfield, VA 22100

Available electronically at http://gltrs.grc.nasa.gov

Propulsion Health Monitoring for Enhanced Safety

Mark G. Butz
General Electric Company
Aircraft Engines
Cincinnati, Ohio

Héctor M. Rodríguez
General Electric Company
Global Research
Niskayuna, New York

Summary

This report presents the results of the NASA contract "Propulsion System Health Management for Enhanced Safety" performed by General Electric Aircraft Engines (GE AE), General Electric Global Research (GE GR), and Pennsylvania State University Applied Research Laboratory (PSU ARL) under the NASA Aviation Safety Program. This activity supports the overall goal of enhanced civil aviation safety through a reduction in the occurrence of safety-significant propulsion system malfunctions. Specific objectives are to develop and demonstrate vibration diagnostics techniques for the on-line detection of turbine rotor disk cracks, and model-based fault tolerant control techniques for the prevention and mitigation of in-flight engine shutdown, surge/stall, and flameout events. The disk crack detection work was performed by GE GR which focused on a radial-mode vibration monitoring technique, and PSU ARL which focused on a torsional-mode vibration monitoring technique. GE AE performed the Model-Based Fault Tolerant Control work which focused on the development of analytical techniques for detecting, isolating, and accommodating gas-path faults.

For the GE GR radial-mode disk crack detection system, a model predicting the crack-induced unbalance response in rotating disks was developed, and sub-scale model disk and full-scale disk tests were performed to evaluate the crack detection algorithm. During the sub-scale model disk test, vibration data was taken before and after an edge crack was machined into the disk. The test results revealed significant variation in the baseline unbalance vibration signature upon disk re-assembly after the crack was machined into the disk. This increase in the unbalance signal masked the vibration signal shift that was expected from the crack. The full-scale disk test of the system was performed using a CFM56 HPT rotor assembly installed in a spin rig at the U.S. Navy's Patuxent River, Maryland facility. Based on lessons learned from the sub-scale test, the full-scale test plan called for a number of baseline vibration measurements to be performed before a corner crack was machined into the disk. The intent was to quantify and eliminate any major sources of system unbalance variation induced by the disassembly and reassembly of the disk. Unfortunately, unbalance variation was found and although steps were taken to maintain precise uniformity in the reassembly process, the variation could not be eliminated. Additionally, higher than expected vibration amplitude levels were also found which was of concern because it directly affected the sensitivity of the crack detection system. Testing did proceed as planned

with a crack machined into the full-scale disk. Unfortunately, the aforementioned complications prevented the definitive detection and isolation of the crack. Although on-line disk crack detection was not demonstrated, several important lessons were obtained from this work. First, the crack-induced portion of the vibration response is relatively small compared to the overall system response for disks of this category. Any steps that can be taken to reduce the baseline vibration amplitude levels will directly improve the sensitivity of the crack detection algorithms. Also, the disassembly and reassembly of the disk introduced a significant variation in the disk vibration response. As such the technique is better suited to applications where a disk crack initiates and propagates naturally as expected in a real-world environment.

For the PSU torsional-mode disk crack detection system, a desktop spin rig for a sub-scale turbine wheel was designed, manufactured and delivered to ARL for use in the development and demonstration of their crack detection algorithm. There also was a demonstration of their signal processing system during a rig test of a CFM56 High Pressure Turbine (HPT) rotor. There were no cracks or known flaws in the PSU sub-scale turbine wheel and the full-scale HPT rotor. The baseline demonstration of the torsional-mode vibration monitoring technique on the HPT rig revealed encouraging results as torsional-mode natural frequencies close to the HPT blade natural frequencies were found as expected. Unfortunately, funding limitations curtailed the development and demonstration of the torsional-mode vibration monitoring technique planned on the sub-scale turbine wheel.

As part of the Model-Based Fault Tolerant Control task, GE AE conducted a search of revenue service engine shutdown data in order to obtain candidate engine fault events that could be improved using a model-based fault tolerant design. A simulation of one revenue service fault condition (Compressor Inlet Temperature Sensor – T25 Intermittence) was then made and tested with new control logic for the accommodation of the simulated fault condition. As part of this Model-Based Control work, NASA was provided a simplified model of the CFM56-7B engine for development of their analytical techniques.

1.0 Introduction

The “Propulsion System Health Management for Enhanced Safety” contract was performed under the Propulsion System Health Management Element of the NASA Aviation Safety Program. The objective of this contract was to develop and demonstrate candidate engine health management technologies for enhanced aviation safety. The technologies included a General Electric Global Research (GE GR) radial-mode vibration disk crack detection system, a Pennsylvania State University Applied Research Laboratory (PSU ARL) torsional-mode vibration disk crack detection system, and a General Electric Aircraft Engines (GE AE) Model-Based Fault Tolerant Control system. The two disk crack detection technologies are potential diagnostic approaches for the automated on-line detection of turbine rotor disk cracks through the noninvasive monitoring of vibration measurements. The objective of these technologies is the early detection of disk cracks prior to their propagation to a critical size where the engine is at risk of an uncontained rotor failure. Model-Based Fault Tolerant Control (MBFTC) is an advanced form of analytical redundancy consisting of an on-board engine model embedded as part of the control logic. The on-board model is automatically tuned to match the performance of the physical engine and is used within the engine controller for the detection, isolation, and accommodation of gas-path faults such as sensor failures, actuator failures, and/or moderated gas-path damage. Under this contract the MBFTC task is specifically focused on reducing sensor, actuator and gas path faults that can cause engine surge/stall, in-flight engine shutdowns or aborted takeoffs. The following sections of this report will present technical descriptions on each technology as well as development and evaluation results obtained under this contract.

2.0 Radial-Mode Disk Crack Detection System

The GE GR radial-mode vibration system has in the past been developed into an on-line crack-detection system for steam and nuclear power plant field applications. The intent under this contract was to extend this technology for the on-line detection of disk cracks in aircraft gas turbine engines. The technology is based on discerning the additional mass-unbalance effect caused by the opening of a crack. When a radial/axial disk crack develops, it tends to open with speed due to the stresses induced by centrifugal loading. The resulting change in the distribution of the disk mass causes a unique shift in the phase and the amplitude of the once-per-rev unbalance vector versus a previously established baseline. This contract required GE GR to develop and test the radial-mode disk crack detection system on vibration data obtained from sub-scale and full-scale turbine disk tests.

2.1 Principle of Radial-Mode Disk Crack Detection System

Cracks in rotor disks have been identified to cause a distinct behavior in the vibration response of rotor assemblies. Radial-axial cracks induce a unique vibration response as they open due to tensile hoop stresses caused by centrifugal loading. The crack, which opens as a function of rotor speed squared, forces a redistribution of the disk mass. This redistribution results in an additional unbalance that is also proportional to the square of the speed, and hence the resulting crack-induced unbalance force is proportional to the fourth power of the speed. This unique unbalance force characteristic contrasts the force due to standard mass unbalance, which is related to the square value of the speed. The present project seeks to develop an on-line monitoring system to detect early stage disk cracks in aircraft engines. The approach consists of identifying the unique speed-dependence characteristic in the vibration signature of cracked disks by measuring the vibration response at non-invasive locations (e.g., bearings).

Crack-Induced Response in Rotating Disks

The physics of the crack-induced vibration response in rotors can be explained using a simplified shaft-disk assembly. Figure 1 shows a one degree-of-freedom Jeffcott rotor in which the shaft-disk assembly is modeled by a spring-mass system restricted to vibrate along the vertical y-axis. In this model, the disk is represented by its mass M and the stiffness of the shaft is represented by k_s. This simplified representation of the rotor is typically used to model the response of single-disk rotor assemblies under relatively rigid bearings (e.g., ball bearings) at relatively low speeds (i.e., near or below the first bending critical speed). The amplitude of the displacement response Y at the center of the disk (i.e., at the shaft-disk interface) due to mass unbalance is given as (reference 1)

$$Y = \frac{u_m \Omega^2}{M\sqrt{\left(1-\Omega^2\right)^2 + \left(2\xi\Omega\right)^2}} \tag{1}$$

where $u_m = me$ is the unbalance due to a finite mass m at a radius of rotation e, $\Omega = \omega / \omega_{cr}$ is the ratio of the shaft speed ω to the critical speed $\omega_{cr} = \sqrt{k_s / M}$, and ξ is the damping ratio.

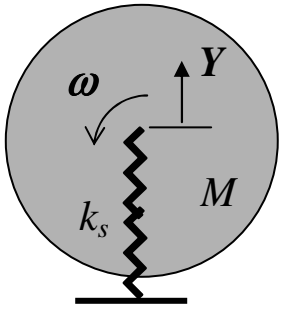

Figure 1. Jeffcott Model of Rotor Assembly

Equation (1) shows that at speeds below the critical speed (i.e., $\Omega < 1.0$), the vibration response due to mass unbalance is proportional to ω^2.

Radial-axial cracks open mainly due to the effect of tensile hoop stresses. In this case, the effect of the hoop stress field induces a further opening of the crack. In the case of a radial-axial crack with length a in a disk rotating at speed ω, the induced unbalanced can be expressed as

$$u_c(a,\omega) = m_c(a,\omega)e_c\,, \tag{2}$$

where the effective change in mass distribution due to the crack opening $m_c(a,\omega)$ is a function of the crack size and speed, and e_c is the effective radius of rotation of $m_c(a,\omega)$. The hoop stress in a rotating disk is a function of the square of the rotating speed ω. Therefore, the effective change in mass distribution due to the crack opening is also a function of the square of the rotating speed. The response of a Jeffcott type rotor with a radial-axial crack can be obtained after substituting $u_c(a,\omega)$ for u_m in Eq. (1). Due to the dependence of $u_c(a,\omega)$ on ω^2, the resulting displacement response in the low-speed regime (i.e., below the critical speed) will be proportional to the fourth power of the speed.

The effect of a radial-axial crack in a disk is investigated using a 2-D FE model of a Jeffcott type rotor assembly. Figure 2 shows a "zoomed" view of the Ansys FE model in the region of the crack. The crack is modeled using Quarter-Point Elements (QPE) (reference 2). The physical characteristics of the disk are diameter D=24-in, thickness t=1-in, Young's modulus E=28x10^6-psi, weight density ρ=0.296-lb/in^3, and Poisson's ratio μ=0.30. This model corresponds to a simplified representation of a CFM-56 disk. The critical speed of the rotor is tuned to 24-krpm to match the fundamental bending critical speed of the CFM-56 disk in the NASA test rig. Three different crack lengths are included in the analysis ranging from a=100-mils to a=300-mils. For simplicity, due to the symmetry of the problem, only half of the disk is analyzed.

Figure 3 shows a comparison between the displacement response at the center of the disk due to a radial-axial crack of a=100-mils and a residual mass unbalance of u_m=0.5g-in, which is representative of a turbine disk residual mass unbalance.

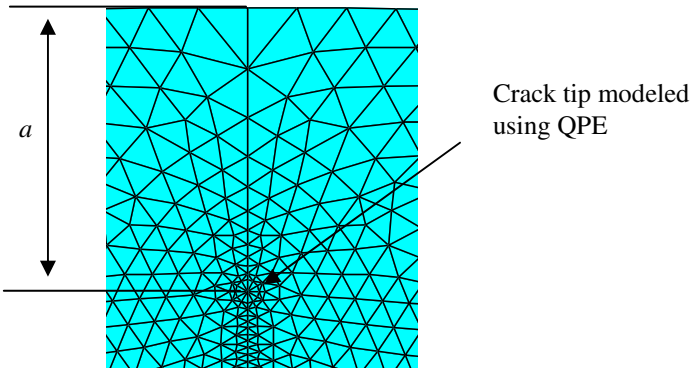

Figure 2. FE Model of Crack Region

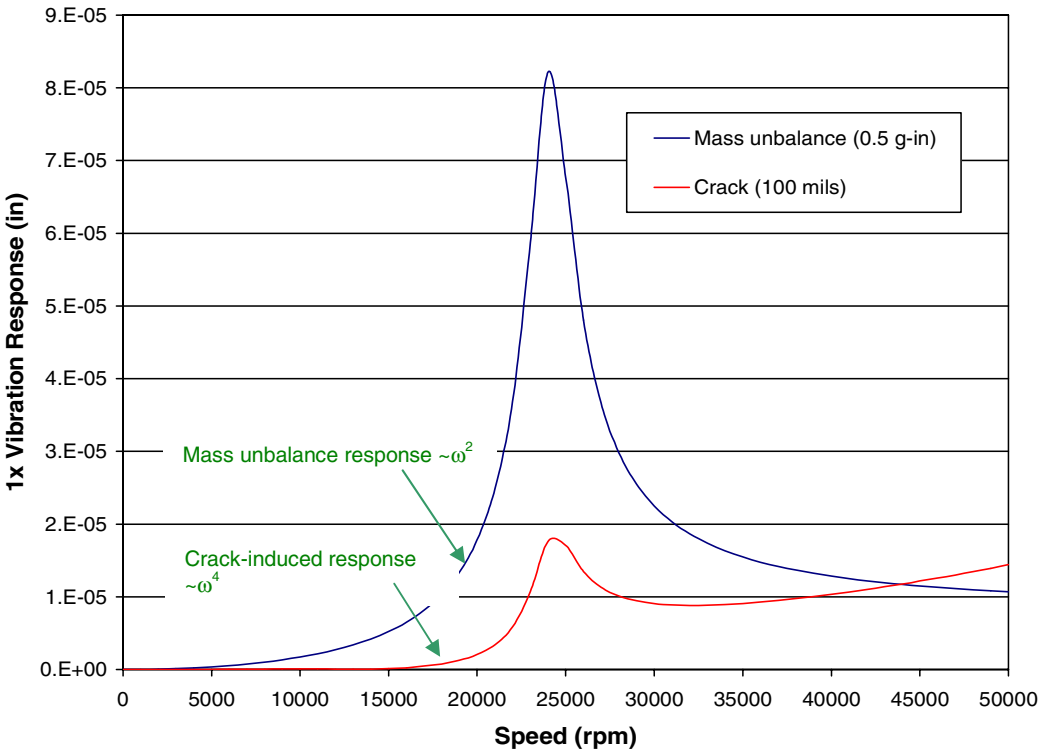

Figure 3. Comparison of Displacement Amplitude Between The Mass Unbalance and Crack-induced Unbalance in Disk

The response due to the unbalance was obtained using Eq. (1). A damping ratio of ξ=0.05 is included in the analysis. As shown in Figure 3, even for a small residual unbalance, the response due to the crack is relatively small in amplitude. The main distinct characteristic of the crack-induced displacement response is that it increases proportional to the fourth power of speed as compared to the mass unbalance that yields a response proportional to the second power of speed. Another feature of the crack-induced response is that it increases with frequency even after passing through the critical speed. Therefore, at speeds higher than the critical speed the effects of the crack-induced response will dominate the total vibration of the rotor. In practice, both signals will be superimposed rather than separated as shown in Figure 3. Therefore, a critical aspect in the proposed crack detection technique is the decomposition of the measured signal in order to differentiate the crack-induced response from the total response. This has been successfully accomplished in practice by using vector subtraction of the baseline (i.e., due to residual unbalance alone) from the total response (reference 3). In the case of a baseline vibration response signal other than displacement (e.g., acceleration), the vector difference response will still be proportional to an equal power plus two.

A comparison between the response amplitude for three different crack lengths is shown in Figure 4. As shown in this figure, the bigger the crack the larger the amplitude of vibration. In general, the increase of amplitude is related to the square value of the increase in the crack length.

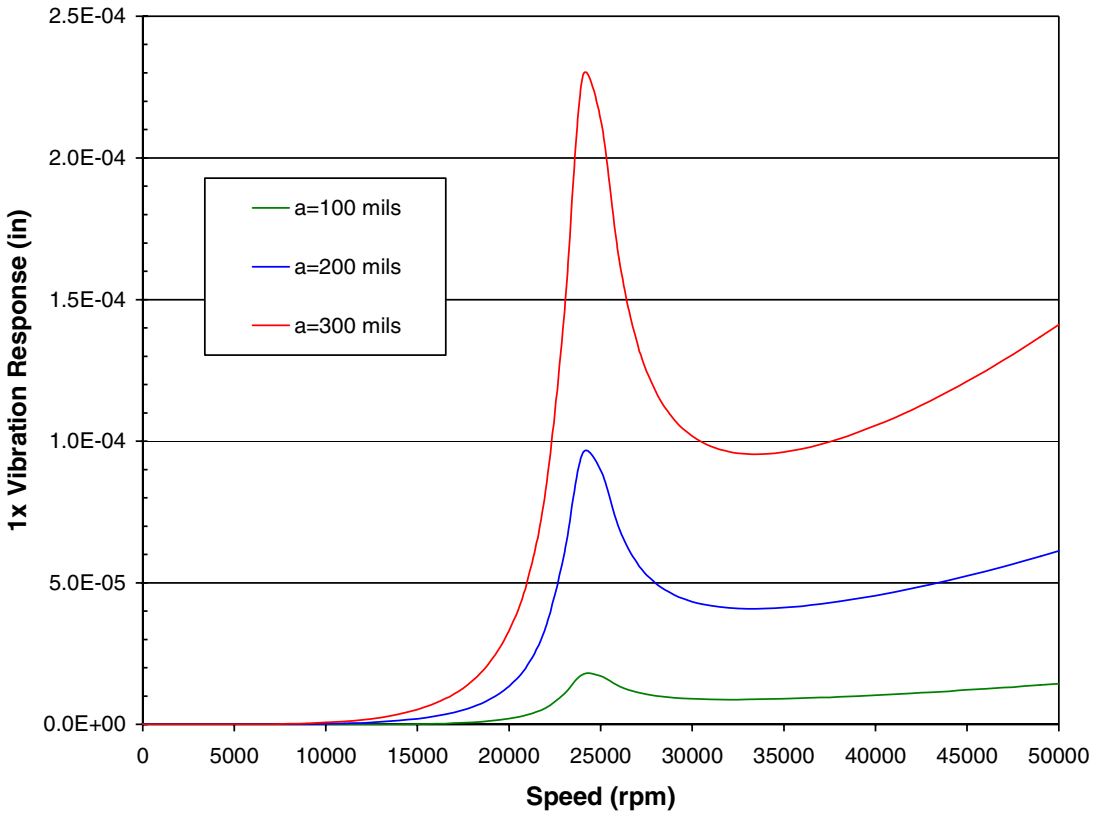

Figure 4. Comparison of Crack-induced Response for Three Different Crack Lengths

Prediction of Crack-Induced Unbalance

An approximate expression for Eq. (2) can be obtained if the effective change in mass distribution due to the crack opening is represented as a "removed" mass while e_c is the radial distance to the crack tip as shown in Figure 5. In the case of a radial-axial crack, the "removed" mass is proportional to the opening of the crack δ as a function of speed. The opening of a small crack in a large-diameter disk can be approximated using the analogy of an edge crack in a plate strip, for which a closed-form solution exists. The opening of the crack due to tensile hoop stress level in the neighborhood of the crack is given as (reference 4)

$$\delta = \frac{4\sigma_h a}{E} V\left(\frac{a}{D}\right), \tag{3}$$

where the empirical function V(a/D) is given as (reference 4)

$$V\left(\frac{a}{D}\right) = \frac{1.46 + 3.42 \times \left(1 - \cos\left(\frac{\pi a}{2D}\right)\right)}{\left(\cos\left(\frac{\pi a}{2D}\right)\right)^2}, \tag{4}$$

where the disk diameter is used instead of the plate's width as considered in the reference. As can be noticed in Eq. (4), $V(a/D)$ approaches the constant value of 1.46 for small ratios of a/D.

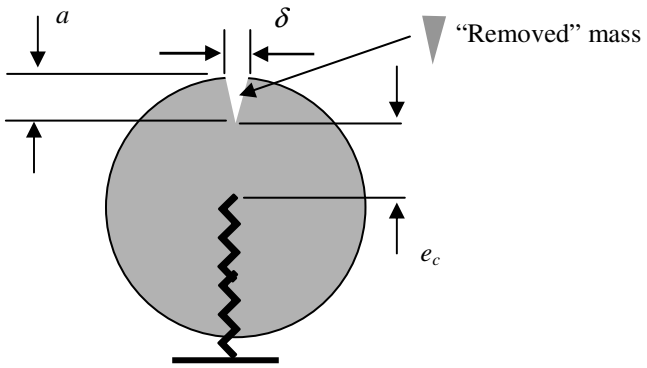

Figure 5. Jeffcott Rotor Showing "Removed" Mass Concept

The hoop stress in a constant thickness disk at a distance e_c is given as (reference 5)

$$\sigma_h = \frac{\rho D^2 \omega^2 (3+\mu)}{32g}\left(1 - \frac{(1+3\mu)}{3+\mu} \times \left(\frac{2e_c}{D}\right)^2\right), \tag{5}$$

where g is the gravity constant. Finally, the "removed" mass can be approximated as

$$m_c = \frac{\delta a t \rho}{2g}. \tag{6}$$

Therefore, the crack-induced unbalance is given as

$$u_c = K\rho^2 a^2 t D^2 \omega^2 e_c, \tag{7}$$

where

$$K = \frac{(3+\mu)}{16g^2 E}\left(1 - \frac{(1+3\mu)}{3+\mu} \times \left(\frac{2e_c}{D}\right)^2\right) V\left(\frac{a}{D}\right). \tag{8}$$

In the case of values of a/D less than 0.05, Eq. (8) becomes K~0.5/E.

Equation (7) clearly establishes the dependence of the crack-induced unbalance on the physical parameters of the disk and the rotational speed. As shown in the equation, the crack-induced unbalance is proportional to the second power of the speed, the weight density, the crack length, and the disk diameter, respectively. In addition, for the case of relatively small cracks, e_c approximates $D/2$ introducing a stronger dependence of the unbalance to the disk diameter.

Figure 6 shows a comparison between the analytical expression in Eq. (3) and the FE analysis for the opening of the crack as a function of rotational speed. As shown in the figure, there is excellent agreement between the analytical and numerical solution.

Figure 7 shows a comparison between the crack-induced unbalance using Eq. (7) and the FE model using customary g-in units. This figure clearly shows the already known relationship between the increase in unbalance to the change in speed and crack size. In general, the increase in the crack-induced unbalance is proportional to the square of the change in speed and the crack length, respectively. This is particularly important to detect small cracks in high-speed machinery. As shown in the figure, the agreement between the "removed" mass approximation and the detailed FE solution improves with the increase in crack size. The discrepancy between the analytical solution and the FE analysis is due to two main differences between both approaches.

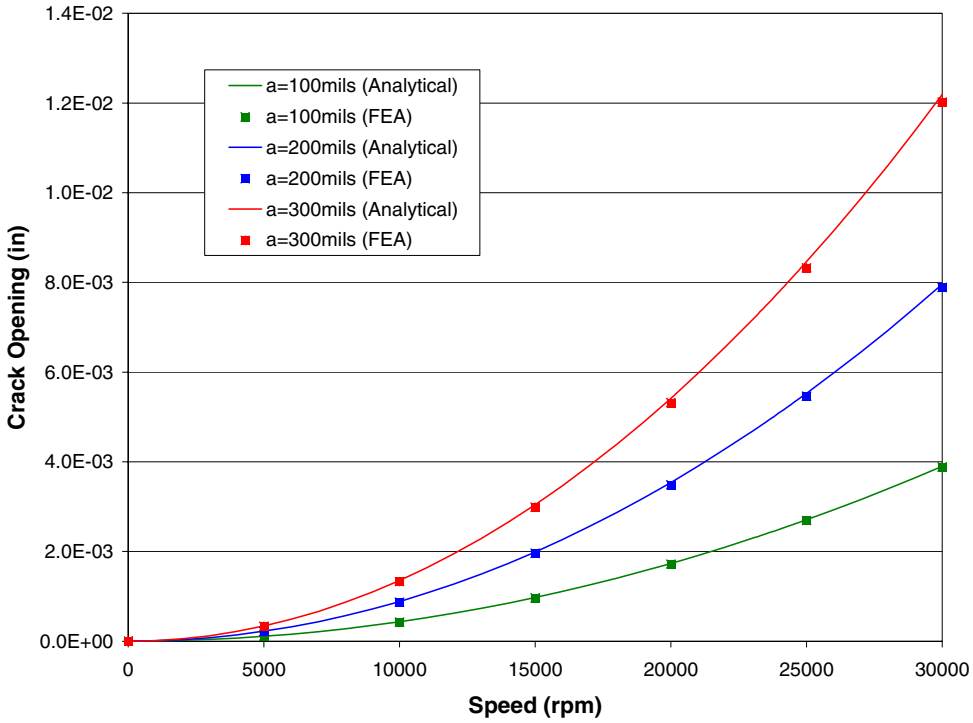

Figure 6. Comparison of Crack Opening Between Analytical Formulation & FE Analysis

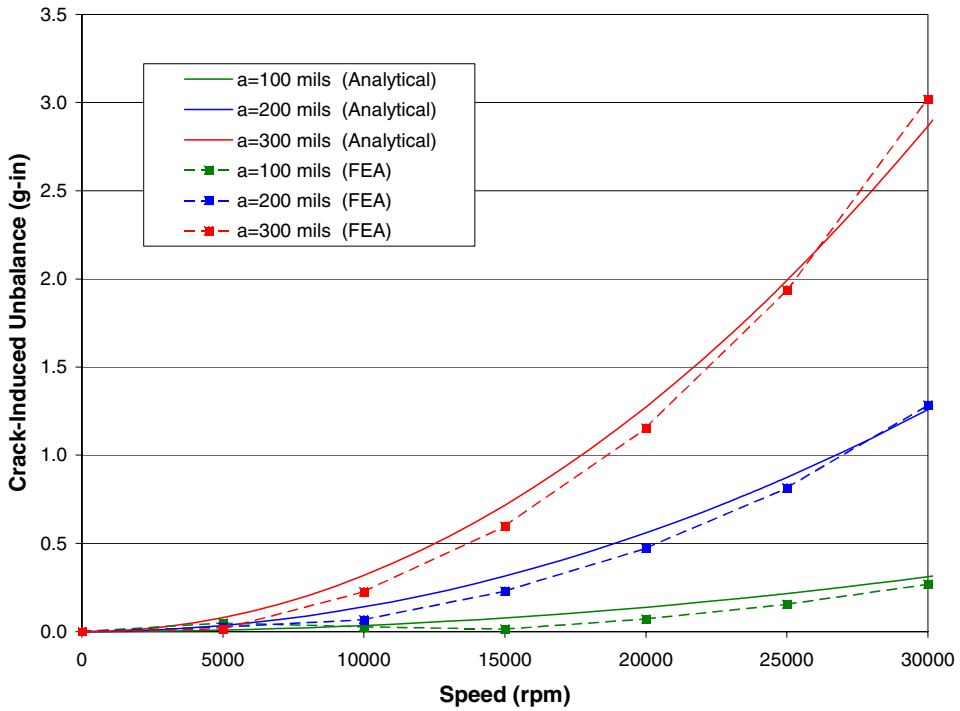

Figure 7. Comparison of Crack-induced Unbalance Between Analytical Formulation & FE Analysis

Firstly, the analytical formulation assumes that the crack opening behaves as if a triangular piece of the disk is removed due to the tensile hoop stress and therefore it behaves as if material is added at 180 degrees from the crack. The FE solution, in addition of having the crack opening due to hoop stresses, also accounts for the disk radial deformation due to radial stresses around the crack. Figure 8 shows a "zoomed" view of the crack opening in the FE analysis. As shown in the figure, the material in the edge of the crack is pulled out of the disk creating an effective mass unbalance that cancels a portion of the "removed" material effect due to the crack opening. The bigger the crack, the "removed" material effect is more dominant than the unbalance due to radial deformation and hence the approximate solution in Eq. (7) becomes a better predictor.

Secondly, the formulation in Eq. (7) assumes that there is no additional mass unbalance in the disk. In practice, due to the approximation of the disk geometry using discrete elements, there will always exist a small unbalance in the FE model. This effect is particularly important in the modeling of disks with large diameter to crack length ratios at relatively low speeds. As the speed increases, the relation of the crack-induced unbalance to the second power of the speed will dominate over the inherent mass unbalance in the model. This approach was the subject of a paper titled "A Physics-Based Approach for the Detection of Cracks in Rotating Disks" presented at the International Society for Air Breathing Engines (ISABE) meeting in Bangalore, India on September 5, 2001 (reference 6).

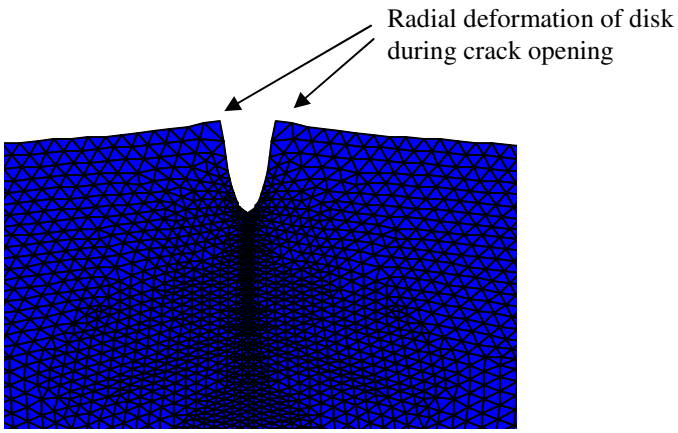

Figure 8. Typical View of Crack Opening During Disk Rotation (FE analysis)

Prediction of Crack-Induced Unbalance for Full Scale CFM56 HPT Disk Test

Based on an approximate approach an estimate for the crack-induced unbalance in the CFM56 disk test was computed. The estimate is based on the results of a 3D model of the disk by GEAE. From the analysis, the hoop stress in the neighborhood of the location of the EDM flaw was used to estimate the opening of an edge crack as a function of stress (i.e., speed). The opening of the crack was used to estimate the change in mass distribution and therefore the increase in rotor unbalance as explained before. Figure 9 shows an estimate of the expected crack-induced unbalance for the CFM56 disk test. Results from the CFM56 balancing indicated that the residual unbalance was on the order of 2.g-in. As shown in the figure, the expected unbalance is relatively small when compared to the expected residual unbalance in the disk. Therefore, even for the largest estimated EDM flaw length, the crack-induced unbalance is expected to be on the order of a small percentage of the mass unbalance.

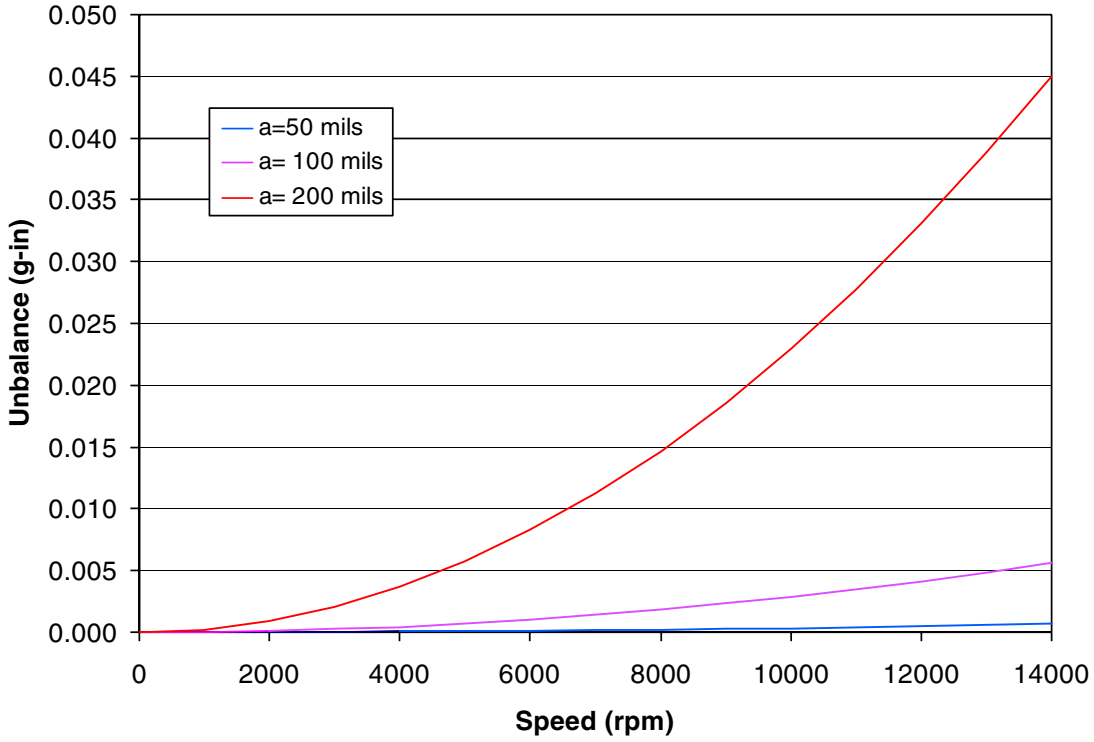

Figure 9. Comparison of Crack-induced Unbalance for Three Different Crack Lengths in CFM56 Rotor

2.2 Sub-scale Model Disk Test

In order to develop the radial-mode disk crack detection algorithm for a full-scale commercial engine application, a test of a sub-scale model disk was performed by GE AE's Component Test organization. The goal of this test was to obtain vibration data before and after a crack was machined into the disk. This data would be used to evaluate the baseline residual unbalance signal level of the rotating disk, and to optimize the signal processing for crack detection. The model disk was made of AMS 4340 steel and had a diameter of 20 inches. A sketch of this disk is shown in Figure 10. This disk was mounted on a spindle capable of 18,000 RPM. The assembly sketch for the hardware used in this test is shown in Figure 11. The test plan required a series of baseline vibration measurements of the rotor assembly before machining an edge crack into the disk. Data from two accelerometers and a once-per-rev sensor was recorded at two steady state conditions, an engine idle speed of 8500 revolutions per minute and an engine takeoff speed of 14200 revolutions per minute. Data was also recorded during transitions from engine-off to idle, and from idle to takeoff. Figure 12 shows the location of the two accelerometers before the disk was installed. Figure 13 shows the model disk installed in the test facility. The baseline vibration and once-per-rev data was recorded on tape and sent to GE GR for their review. The disk was then removed from the spindle and taken to an EDM lab where a 6 mil wire was used to cut a 0.200 inch deep edge crack into the disk's outer circumference. The disk was then returned to the test facility and another set of data was recorded.

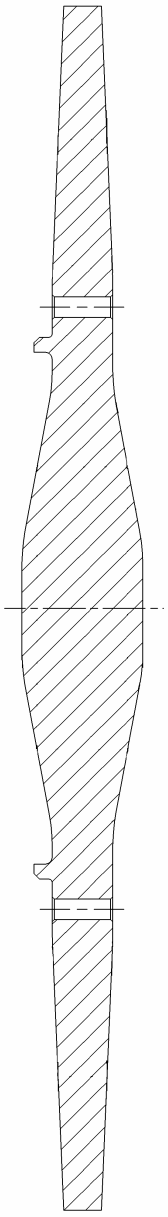

Figure 10. Model Disk Sketch

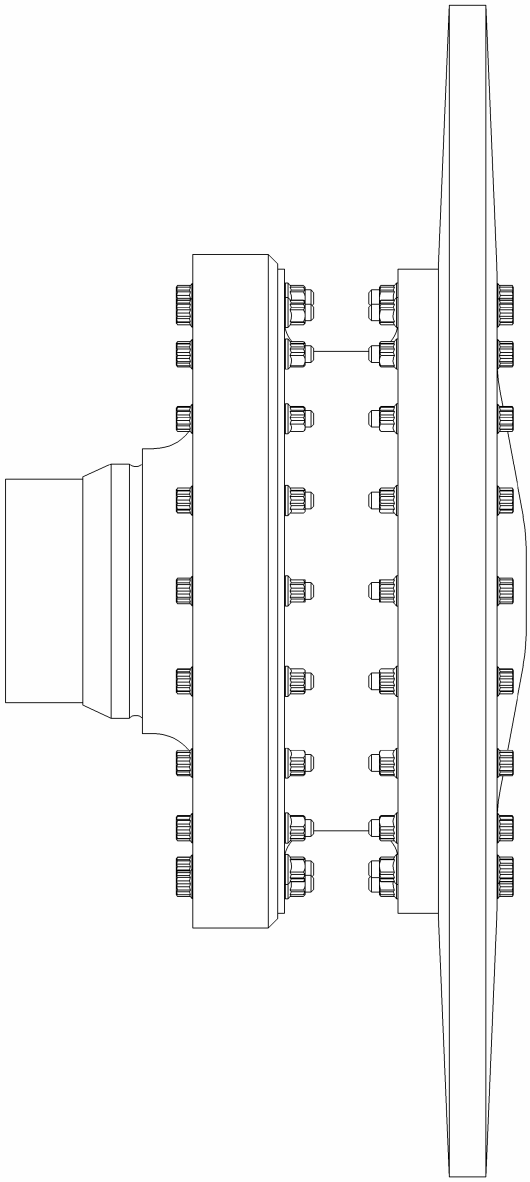

Figure 11. Model Disk Assembly Sketch

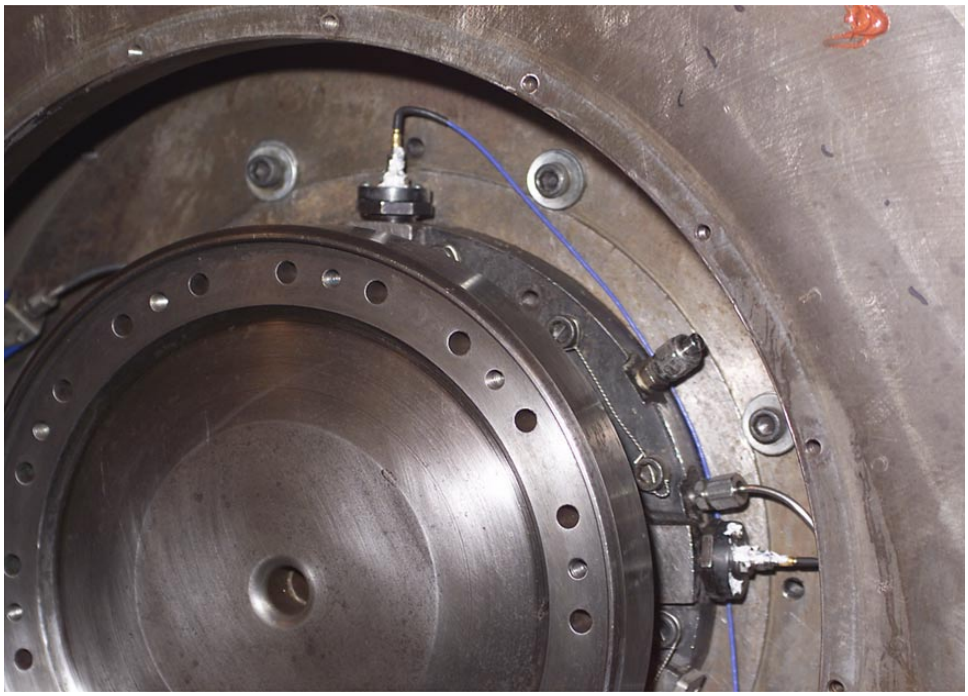

Figure 12. Horizontal and Vertical Accelerometers Installed Over Rig Bearings

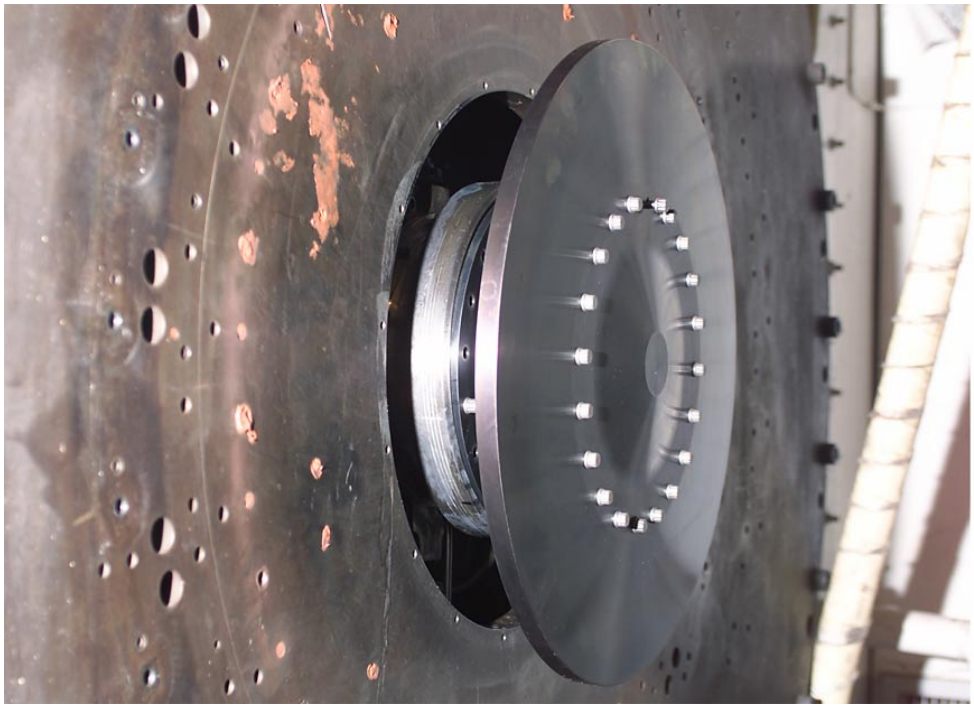

Figure 13. Model Disk Installed In Test Facility

The 0.200-inch depth for the edge crack was selected based upon analyses performed by GE GR and GE AE. The first analysis was performed by GE GR assuming the depth of 0.500 inches. They calculated the Stress Intensity Factor of this crack using a Finite Element Ansys model and by the following formula (reference 4):

$$K_I = f\left(\frac{a}{D}\right)\sigma_h\sqrt{\pi a} \tag{9a}$$

where

$$f\left(\frac{a}{D}\right) = \frac{1.122 + 0.140\left(\frac{a}{D}\right) - 0.545\left(\frac{a}{D}\right)^2 + 0.405\left(\frac{a}{D}\right)^3}{\left(1-\frac{a}{D}\right)^{\frac{3}{2}}} \tag{9b}$$

At the maximum speed of 15,000 rpm, the Ansys Stress Intensity Factor value was 31.6 ksi in^1/2 and the calculated value was 32.3 ksi in^1/2. Based on the typical design handbook fracture toughness value for AMS4340 of 52.0 ksi in^1/2, the factor of safety was 1.64. The analysis also showed that the crack would begin to grow at a disk speed of 19,000 rpm. The GE AE analysis agreed with GE GR's Stress Intensity Factor number, however it was determined that the value for AMS4340 fracture toughness was highly dependent upon the material's strength and purity levels. Since this material property data was not available for the model disk under test, it was decided to be conservative and make the crack depth 0.200 inches.

The vibration data from these tests were analyzed by GE GR. The data from the horizontal accelerometer is shown in Figure 14 and the data from the vertical accelerometer is shown in Figure 15. GE GR made the following observations about this data:

1) The noise at 3600 rpm was assumed to be electrical line frequency interference
2) The change in the fundamental critical speed of the system after the crack was machined in the disk suggests a difference in test setup
3) There was a constant difference in accelerometer response levels in the 6K to 13K rpm range suggesting a difference in test setup.
4) There is a divergence in the accelerometer response in the greater than 13K rpm range for the data after the crack was machined in the disk suggesting that the crack opening effect occurred.

The GE GR crack detection algorithm uses a vector subtraction process in order to extract the vibration signal from the crack unbalance out of the total vibration signal, which includes residual unbalance and crack-induced unbalance. When this algorithm was applied to the data shown in Figures 14 and 15, the increased rotor unbalance signal seen in the data after the crack was machined in the disk prevented the detection of the crack's vibration signature. The crack detection algorithm assumes the rotor unbalance signal does not change as a result of the machining operation. This increase in the unbalance signal masked the vibration signal shift that was expected from the crack.

After reviewing the results with the test facility team, it was learned that during the time that the disk was in the machine shop, another disk test was performed on the same spindle. Although there was no record of a change made to the balancing of the facility for the other disk test, it is

believed that a change did occur in the spindle/rotor system that was significant enough to create the offset in the rotor unbalance vibration signal.

This sub-scale disk test demonstrated the importance of documenting the variation of the baseline unbalance signal prior to machining the crack in the disk. It also showed that changes to the baseline unbalance signal due to disassembly and reassembly of the rotor assembly can be larger than originally expected. These important lessons were applied to the test plan for the full-scale disk test.

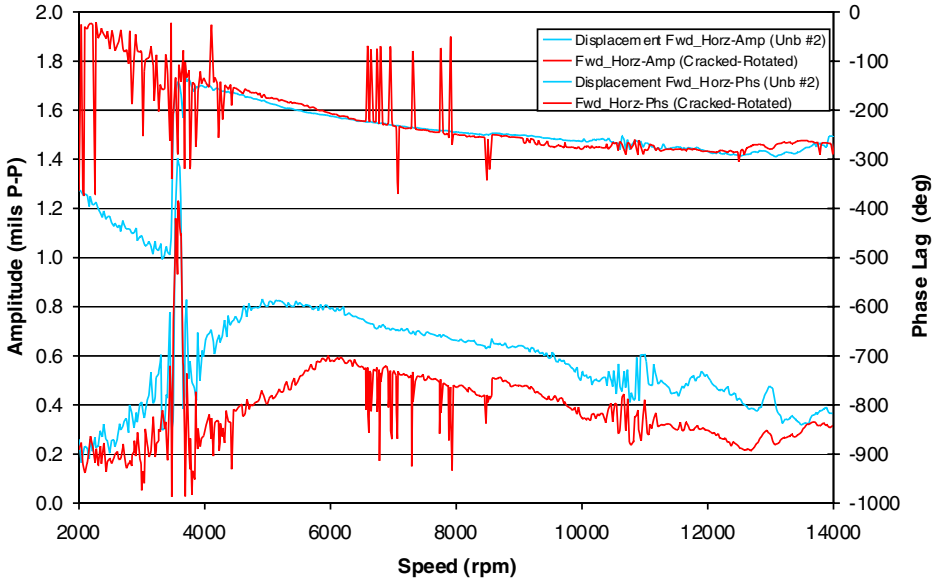

Figure 14. Horizontal Accelerometer Measurements

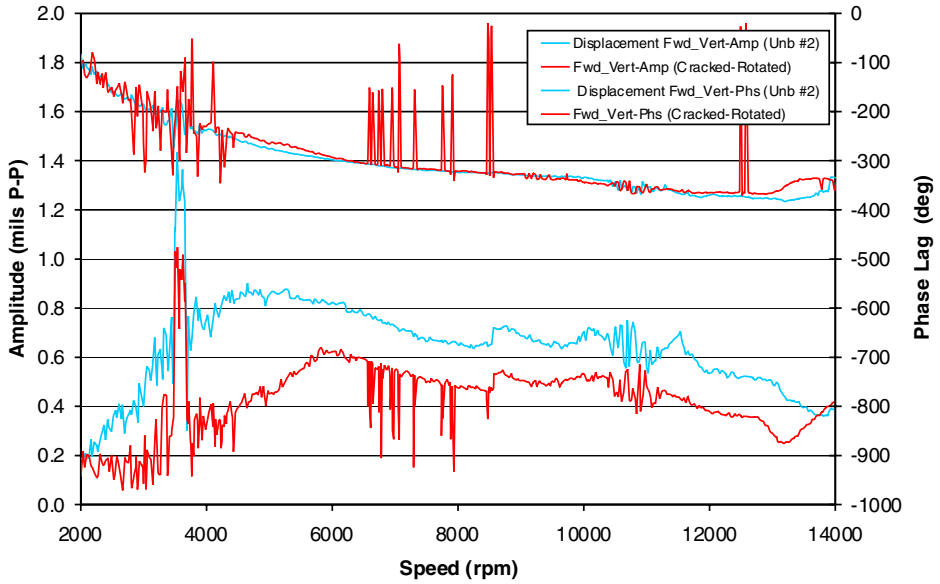

Figure 15. Vertical Accelerometer Measurements

2.3 Full-scale CFM56 High Pressure Turbine Rotor Assembly Test

The major task in this contract was the testing of the GE GR crack detection algorithm on vibration data obtained from a full-scale CFM56 High Pressure Turbine (HPT) Rotor assembly. The HPT rotor assembly was provided by GE AE, and NASA Glenn Research Center was to provide the spin rig. GE AE designed a test shaft and adapter hardware for the HPT rotor so it could interface with the NASA air turbine drive system. GE AE also designed a dual bearing support system for this rotor assembly so it could be installed in a housing that is part of NASA's spin rig. After a design review of the NASA spin rig hardware and an analysis of the NASA containment system, a decision was made to move the test to the Navy's Patuxent River spin rig facility for safety reasons. Details of the Patuxent River test are contained in the paragraphs below and in the Patuxent River final report (reference 7).

2.4 Modifications to CFM56 HPT Disk

The CFM56 HPT Disk used in this test included a full set of turbine blades. These blades are normally held in the disk's dovetail slots by retaining hardware installed on the forward and aft side of the disk. This retaining hardware is part of other engine assemblies that require special tooling, and special disassembly and reassembly procedures involving dry ice. Since it was not practical to perform these procedures at NASA Glenn or Patuxent River, a modified retaining system had to be designed which simplified the blade removal process. New forward and aft retaining rings were designed and 40 through-holes were machined into the HPT disk so bolts could be used to connect the two rings together. The HPT disk also had its forward side flange machined off so the disk could be installed as close as possible to the top cover plate of the NASA spin rig.

2.5 Design Review of Test Rig Assembly for NASA Spin Rig

The HPT rotor test rig assembly was designed by GE AE's Test Facilities Engineering organization. A sketch of this assembly is shown in Figure 16. This design was reviewed by engineers from NASA Glenn Research Center and GE AE's Chief Engineers Office, Rotating Parts Center of Excellence, Test Facilities Engineering Office, Component Test Office, and Controls Center of Excellence. The design review presentation (reference 8) included detailed review of the assembly drawing, rotordynamic analysis of the bearing design, and stress analysis of the modified HPT disk and rotor assembly. There were two major action items as a result of the design review. The first item involved a fracture mechanics analysis of the stresses in the HPT disk dovetail slot bottom for the various corner crack depths. The second item involved an analysis of the NASA Spin Rig Containment ring capability. These items are discussed in the next paragraphs.

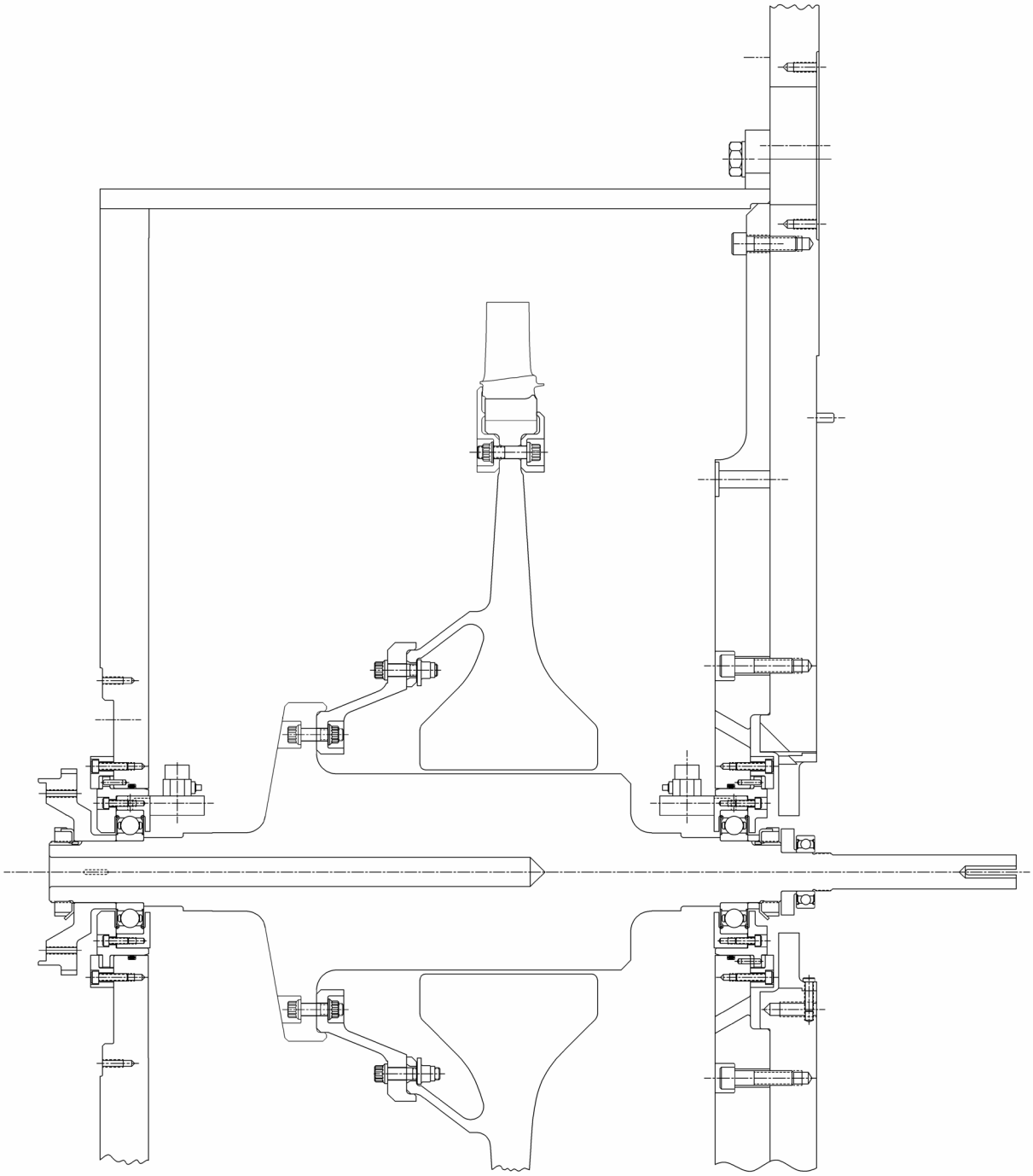

Figure 16 – NASA Spin Rig Assembly Sketch

2.6 Fracture Mechanics Analysis

The GE AE Rotating Parts Center of Excellence performed a fracture mechanics analysis of the modified CFM56 HPT disk. The ANSYS 3D finite element analysis of the dovetail slot bottom stresses included boundary conditions for turbine blade loads and rotational speeds up to 14000 RPM. The analysis initially concluded that the corner crack should be cut into the forward side of the disk since this side of the dovetail slot had more material thickness and lower stresses. The analysis then determined the number of cycles that could be performed before the various crack dimensions began to grow. For this cycle limit work, it was assumed the corner crack was a quarter-circle shape with axial length equal to its radial length. Using the properties of the disk's Direct Aged Inconel 718 material, crack growth information was obtained. This data is shown in Table 1. In this table, the label A represents the crack's axial length and the label C represents the crack's radial length. Based on this analysis, the decision was made to not cut the corner crack deeper than 0.200 inches. This would allow the disk to be tested up to 402 cycles with a safety factor of two.

Table 1. Crack Growth Data From Fracture Mechanics Analysis

INITIAL A (IN)	INITIAL C (IN)	FINAL A (IN)	FINAL C (IN)	FINAL CYCLES
0.05	0.05	0.2449	0.2868	10101
0.1	0.1	0.24987	0.27573	4801
0.15	0.15	0.26141	0.28255	2301
0.175	0.175	0.25505	0.26881	1425
0.2	0.2	0.25571	0.26852	804
0.25	0.25	0.26165	0.26744	101
0.3	0.3	0.3	0.3	1
0.35	0.35	0.35	0.35	1
0.375	0.375	0.375	0.375	1
0.4	0.4	0.4	0.4	0

2.7 NASA Containment Structure Analysis

The NASA Spin Rig consists of an above ground housing that is mounted on three support legs to the facility floor. The rig has an inner containment shield installed in the plane of the rotating disk. In order to determine if the NASA containment shield and housing could withstand the impact of a burst HPT disk, GE AE made a calculation of the translational energy of a disk fragment assuming the HPT rotor burst into three equal fragments. This analysis is shown below:

Kinetic Energy Associated with a TRI-Burst Disk Failure of CFM56-5A HPT Rotor

Assumes rotor burst into three equal fragments.
Find center of gravity of 120 degree fragment (rcg):

Mass of disk plus retainers (md): $md := 68.6 \cdot lb$ CG of disk plus retainers (rdisks):
$rdisk := 6.125 \cdot in$
From UG model - Gary Stiebing

Mass of Blades (mb): $mb := \left(\frac{80}{3}\right) \cdot .334 \cdot lb$ CG of Blades (rblades): $rblades := 12.6 \cdot in$

$mb = 8.907\,lb$

Center of Gravity for disk plus blades (rcg): $rcg := \frac{(md \cdot rdisk + mb \cdot rblades)}{md + mb}$ $rcg = 6.87\,in$

Total Mass (m): $m := md + mb$ $m = 77.5\,lb$

$rev := 2 \cdot \pi$ $rpm := 1 \cdot \frac{rev}{min}$

Rotational Speed (N): $N := 14000 \cdot rpm$

Angular Velocity (ω): $\omega := N$ $\omega = 1466 \frac{rad}{sec}$

Velocity (v): $v := rcg \cdot \omega$ $v = 10071 \frac{in}{sec}$

Total Kinetic Energy (Etotal): $Etotal := \frac{1}{2} \cdot m \cdot v^2$ $Etotal = 1.018 \times 10^7\,lbf \cdot in$

Radius of Gyration for Disk (kd): $kd := 8.016 \cdot in$

Radius of Gyration for disk and blades (k): $k := \frac{md \cdot kd + mb \cdot rblades}{md + mb}$ $k = 8.543\,in$

Per ASME Article 'The Containment of Disk Burst Fragments by Cylindrical Shells' authored by A.C. Hagg and G.O. Sankey dated April 1974 from The Journal of Engineering for Power the resulting translational kinetic energy is equal to (rcg/k)^2 multiplied by the total kinetic energy.

$Etranslational := \left(\frac{rcg}{k}\right)^2 \cdot Etotal$ $Etranslational = 6.582 \times 10^6\,lbf \cdot in$

The original plan for the NASA spin rig test was to have a new 3-inch thick Nitronic containment shield installed in the rig housing. An analysis was performed by NASA that concluded that this containment shield had the capability to contain the 6.582×10^6 lbf-in energy level from a burst disk fragment, however the shield would undergo deformation which would cause it to impact the wall of the rig housing. NASA's analysis indicated that the stress level could be 75 ksi. Since the wall is made of 304 Stainless steel, this ultimate tensile strength can be as low as 73 ksi according to Mil-Hdbk-5F. NASA concluded that for concerns of safety and damage to their facility, that it was not practical to perform the test at NASA Glenn. Alternative arrangements were made to perform the test at the Naval Air Warfare Center's Rotor Spin Facility at Patuxent River, MD.

2.8 Eddy Current Blade Deflection Analysis

An alternative disk crack detection system was devised by NASA Glenn based upon the interpretation of measurements collected from a Non-Interference Structural Measurement System (NSMS) array of optical probes. This system measures blade tip deflection of all the blades in a rotor, and seeks to detect and isolate a discernible change in damping of the specific blade located in the dovetail slot where a disk crack is introduced. There was a concern that the testing of the HPT disk with a full set of turbine blades in a vacuum spin rig housing would not provide any aerodynamic loading of the turbine blades and thus any change in blade damping would be unobservable. In order to create a deflection force of the turbine blades, NASA Glenn proposed an excitation system consisting of a ring structure on which were mounted a number of permanent magnets. The magnets are equally spaced around the circumference and near the blade tips. As the blades rotate past the magnets, eddy current forces are created which cause the blades to vibrate. Remotely changing the spacing between the blades and the magnets controls the amplitude of the forces induced in the blades. The number of magnets used, their spacing, and the rotation speed of the rotor determine the excitation frequency. GE AE performed an analysis of the blade stress associated with this blade deflection proposal assuming the trailing edge deflection would be +/- 0.006 inches. Using a Finite Element Analysis, it was determined that the blade would be at the 100% Goodman Diagram limit, and the blade would break at its leading edge root. Since the GE AE design practice allows operation up to 50% of the Goodman Diagram limit, a deflection of +/- 0.003 inches would be acceptable. This information was provided to NASA Glenn and NASA reviewed the capability of the fiber optic blade deflection measurement system. It was determined that the monitoring of blade amplitude changes of this magnitude could not be performed efficiently in real-time. It was also learned that the uneven surface of the turbine blade tip would result in a light reflection that would be unacceptable to the triggering logic used for the deflection measurement. The decision was made by NASA to terminate plans for the NSMS and the associated eddy current blade deflection system as part of the spin rig test.

2.9 Patuxent River Spin Test Preparation

The installation of the test hardware from the NASA Glenn spin rig in Patuxent River's Rotor Spin Facility Chamber Number 1 was performed by bolting the NASA rig housing top cover to the bottom of the Patuxent River spin rig cover plate. See Figure 17 taken from the Patuxent River Final Report (reference 7). The vibration data for the GE GR disk crack detection algorithm was obtained from four accelerometers mounted by the upper and lower bearings, as shown in Figure 18. A test procedure was created by the NASA/GE/Patuxent River team prior to starting the test (reference 9). This procedure used the GE AE standard Test Project Sheet format that includes a description of the step-by-step tasks required during the test. Since there was

some additional test instrumentation installed that was not defined in this TPS, a complete description of all test instrumentation is contained in the Patuxent River Final Report (reference 7).

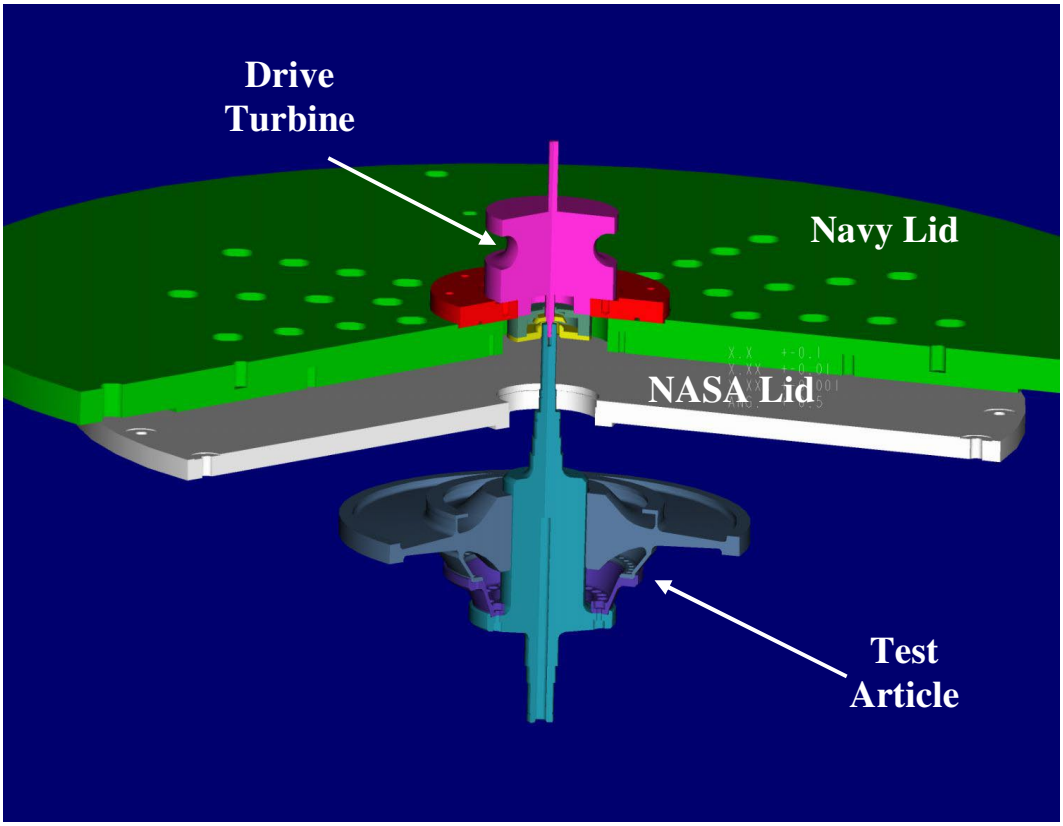

Figure 17. Test Assembly

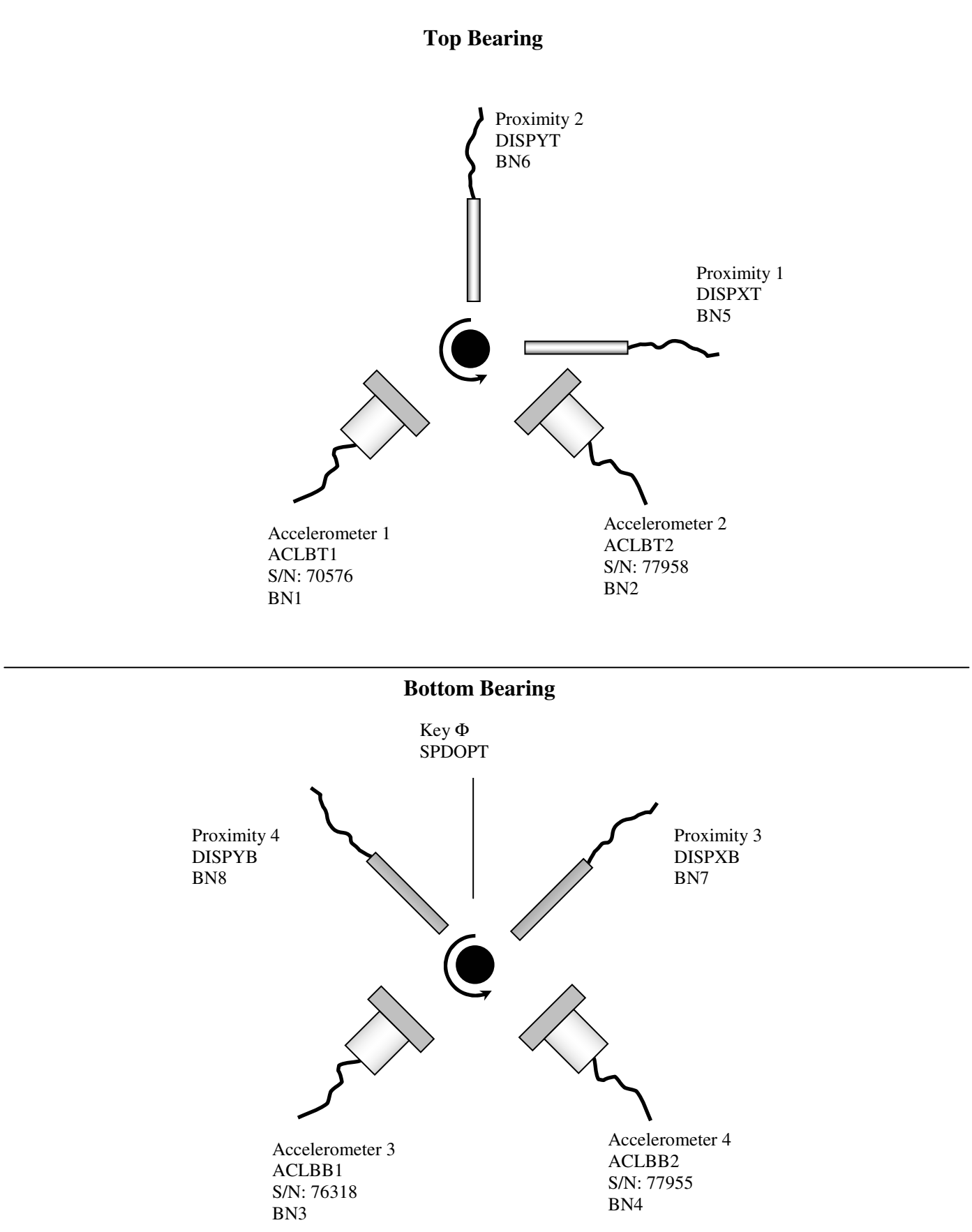

Figure 18. Crack Detection Instrumentation Labels

2.10 Preliminary Tests

Testing was initiated on November 6, 2001. Figures 19 through 22 show the synchronous (i.e., 1X) vibration response (i.e., amplitude and phase) at the four accelerometers. In these figures, the green curves indicate the initial run-up to 14 krpm, the blue curves indicate the final coast-down and the red curves indicate the run time in between the initial run-up and the final coast-down. The solid curves indicate filtered synchronous response while the dashed curves represent the overall (i.e., unfiltered) vibration. As shown in the Bode plots, the unfiltered acceleration response at all four accelerometers became "noisy" at high speeds (i.e., above 12 krpm). Inspection of the vibration levels at high speed for the top accelerometers indicated that the response exceeded the 10g limit on the accelerometers.

Figures 23 through 26 show the Waterfall plots for all four accelerometers. The color legends in the Waterfall plots follow the same logic as the ones for the Bode plots in Figures 19 through 22. In particular, Figures 23 and 24, which contain data from the two top mounted accelerometers show a high amplitude component near zero frequency (i.e., DC) due to a saturation effect from exceeding the accelerometer amplitude limit. As shown in Figures 23 through 26, the vibration data contained significant levels of 2X vibration, which is typically associated with driver to rotor coupling misalignment. The existence of high 2X components immediately raised a flag due to the potential negative effect of misalignment on the capability to observe the effect of a small EDM flaw. Similar to residual mass unbalance, rotor misalignment also increases the 1X vibration with the added effect that it is more difficult to control and repeat from one assembly to the next.

A halt to the initial testing occurred after the failure of the roll pin that transferred torque from the air turbine drive spindle to the test shaft. Figures 27 through 30 show the coast-down data immediately after the roll pin failure. As indicated in all plots, there was a significant reduction in vibration immediately after the failure. This result indicated that a significant source of vibration was transmitted from the drive spindle and not due to the residual disk unbalance.

Figures 31 through 34 show the Waterfall plots during the roll pin failure run. As shown in these figures, prior to the roll pin failure, the data indicated significant asynchronous vibration components and accelerometer saturation. After the roll pin failure, most of the asynchronous vibration was eliminated.

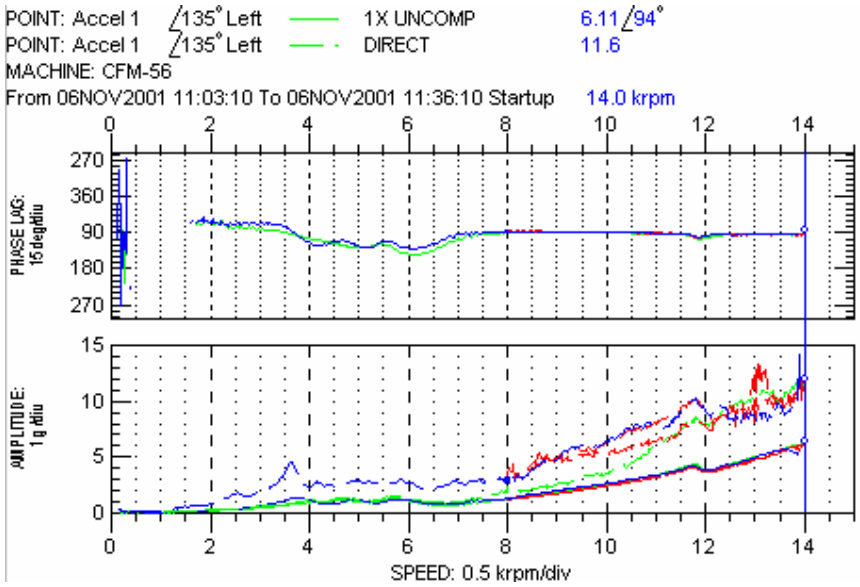

Figure 19. Vibration Response at Accelerometer #1

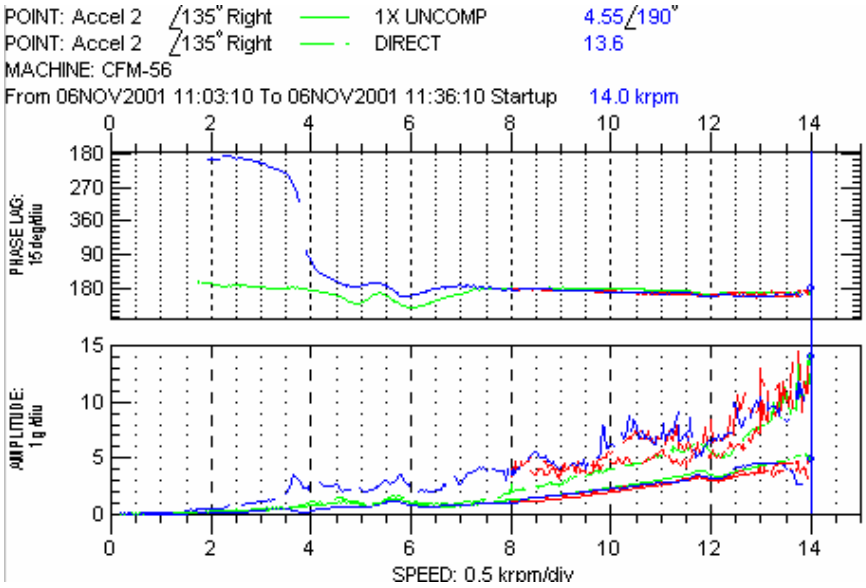

Figure 20. Vibration Response at Accelerometer #2

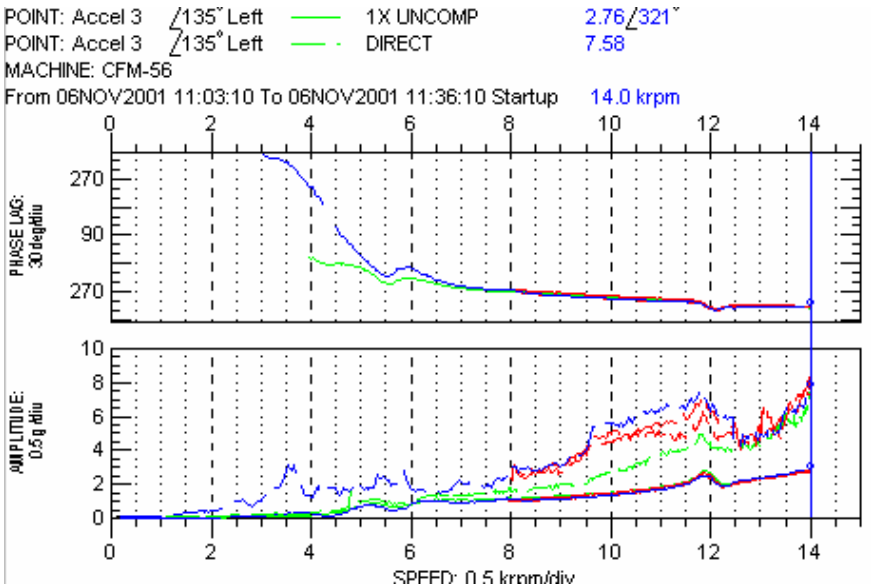

Figure 21. Vibration Response at Accelerometer #3

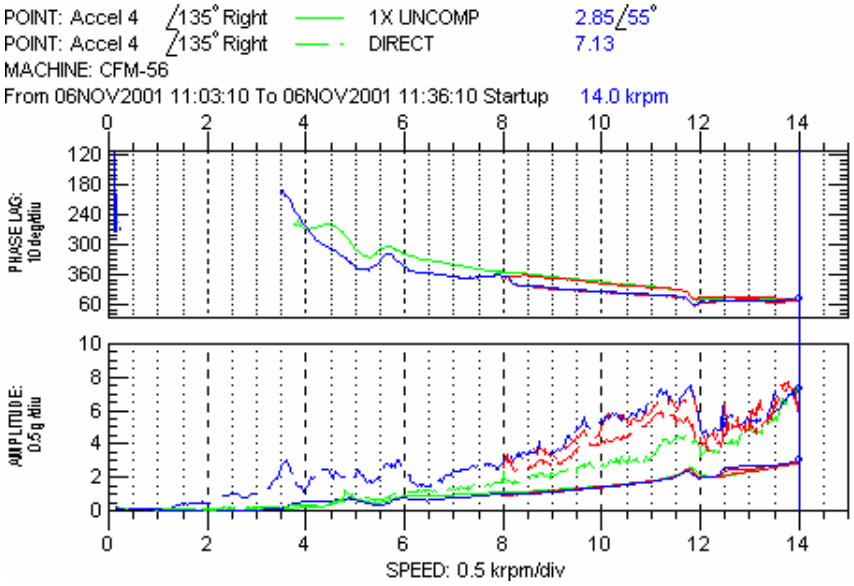

Figure 22. Vibration Response at Accelerometer #4

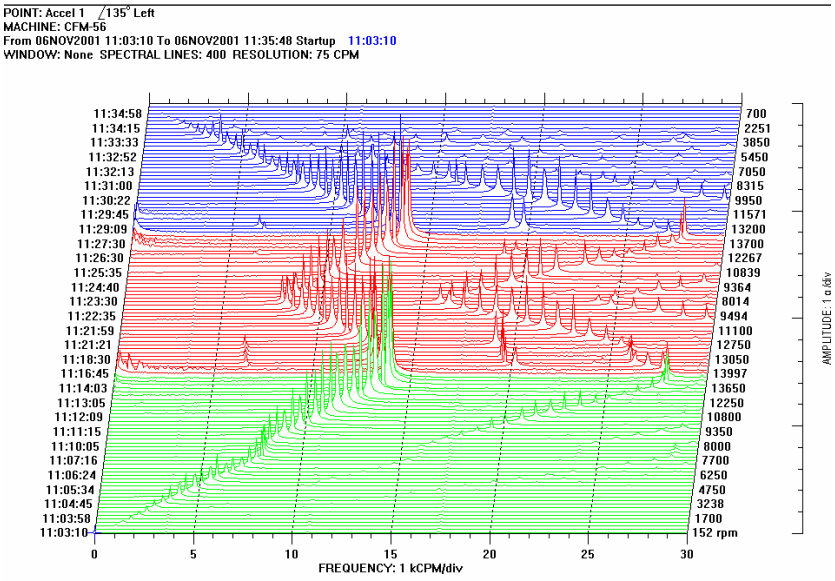

Figure 23. Waterfall Plot of Accelerometer #1

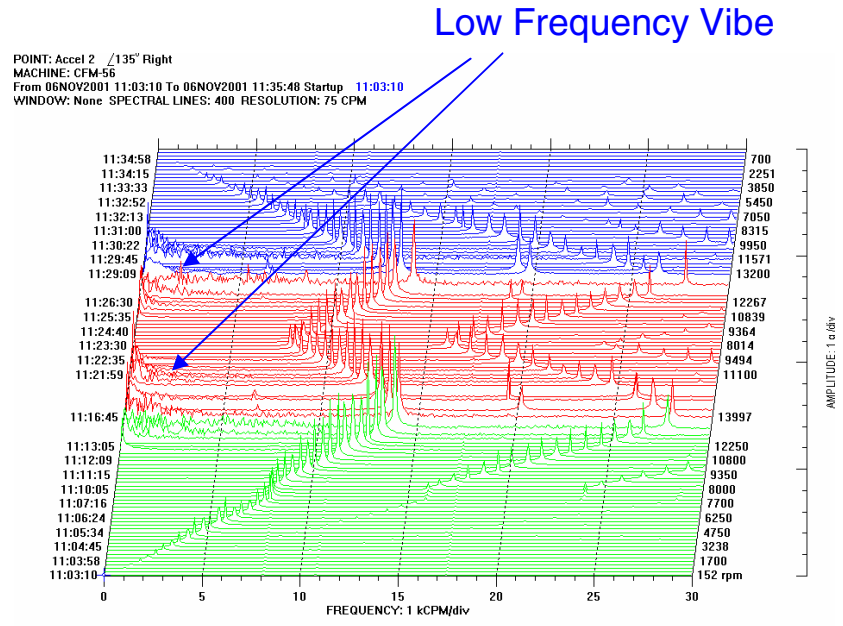

Figure 24. Waterfall Plot of Accelerometer #2

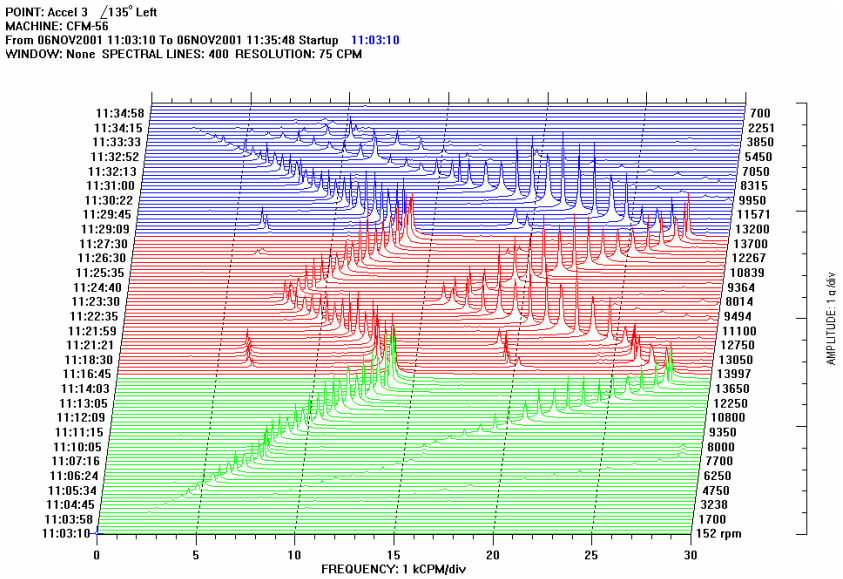

Figure 25. Waterfall Plot of Accelerometer #3

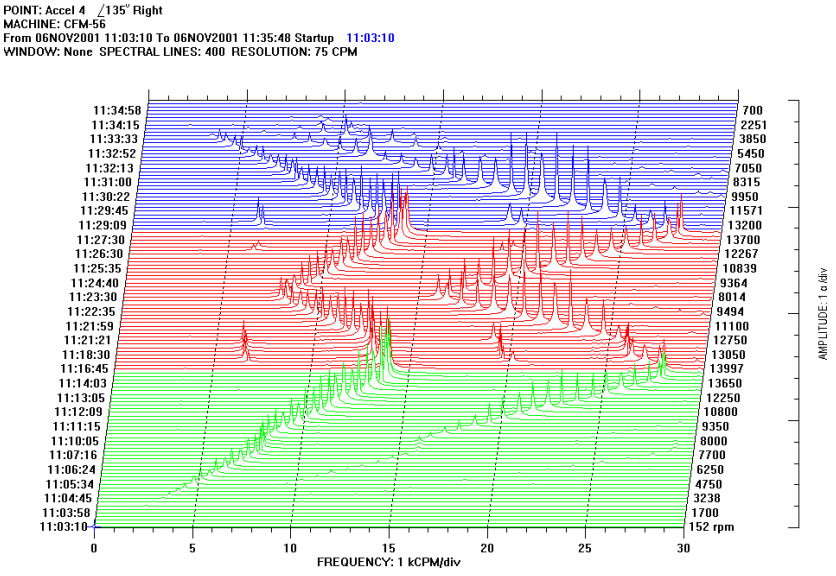

Figure 26. Waterfall Plot of Accelerometer #4

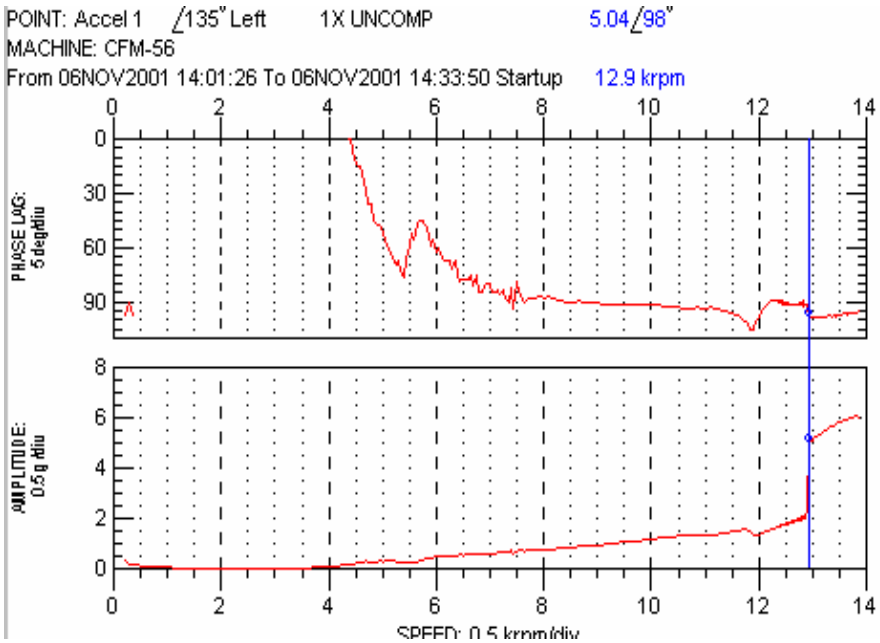

Figure 27. Coast-down Response at Accelerometer #1 During Pin Failure

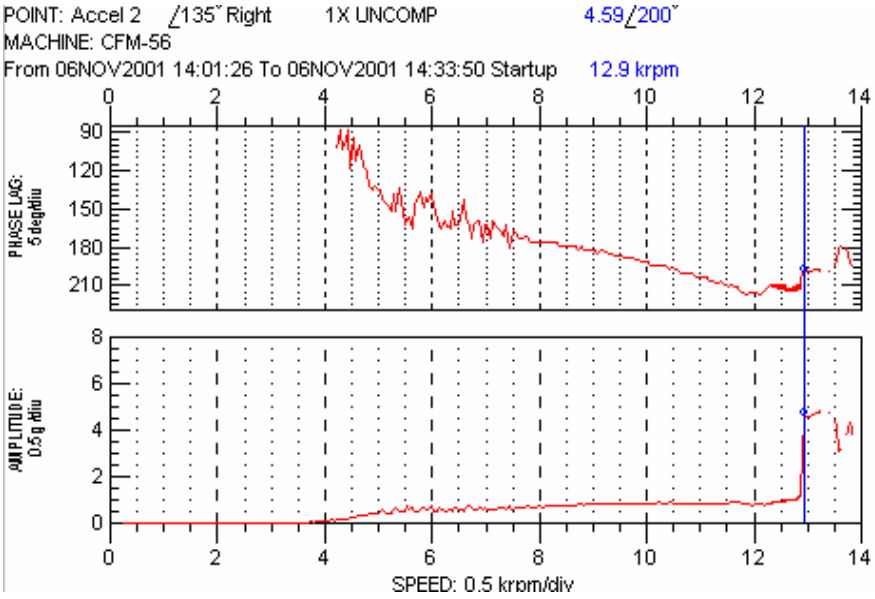

Figure 28. Coast-down Response at Accelerometer #2 During Pin Failure

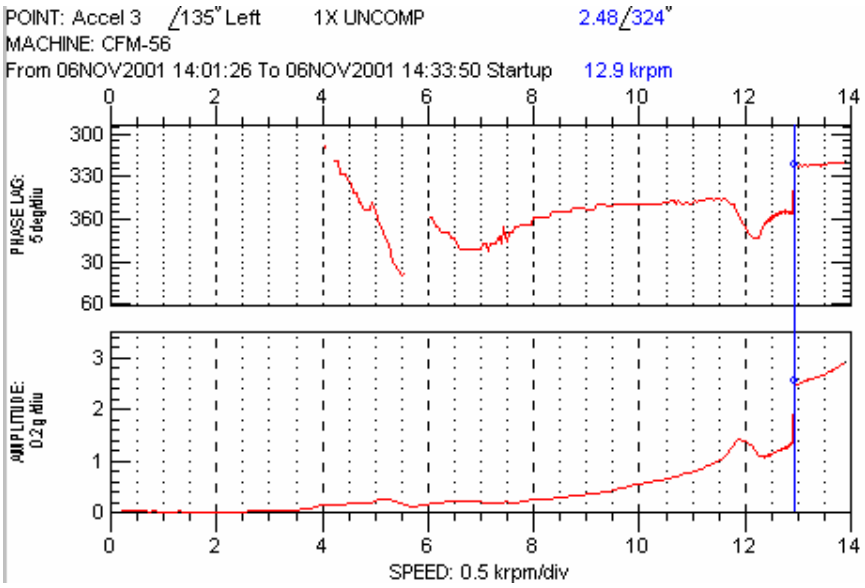

Figure 29. Coast-down Response at Accelerometer #3 During Pin Failure

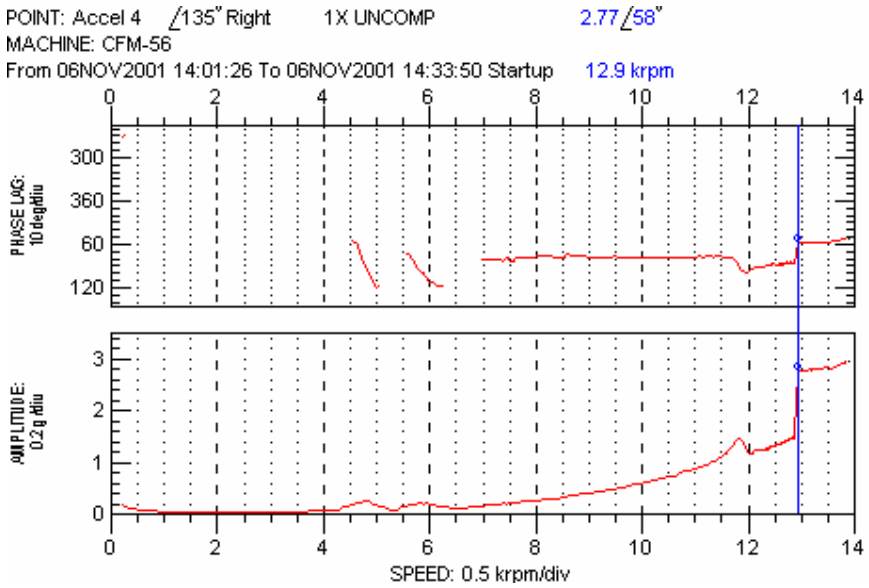

Figure 30. Coast-down Response at Accelerometer #4 During Pin Failure

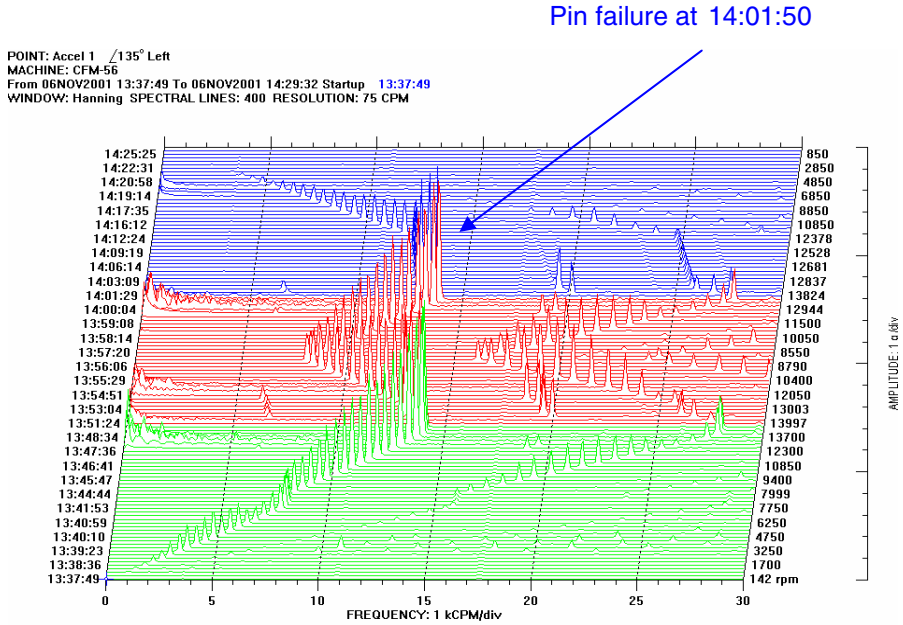

Figure 31. Waterfall Plot of Accelerometer #1 During Pin Failure

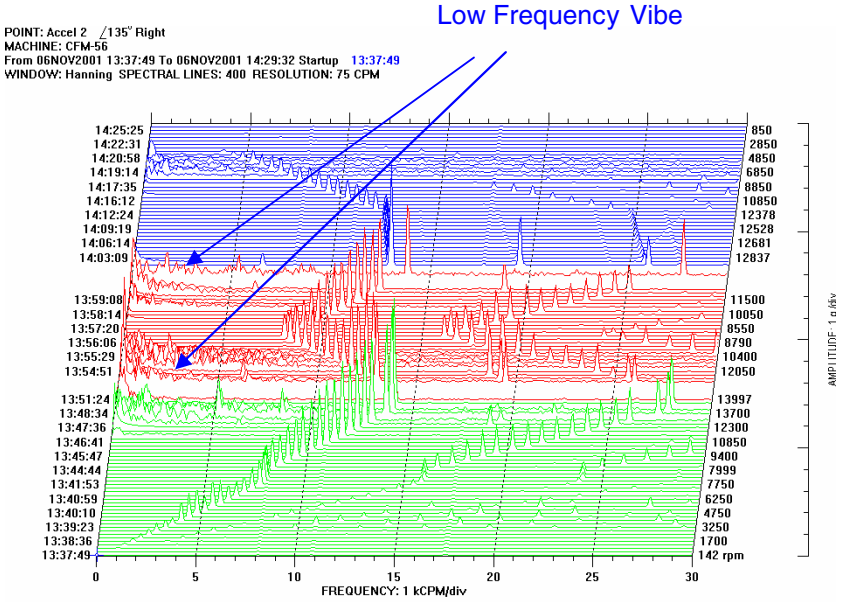

Figure 32. Waterfall Plot of Accelerometer #2 During Pin Failure

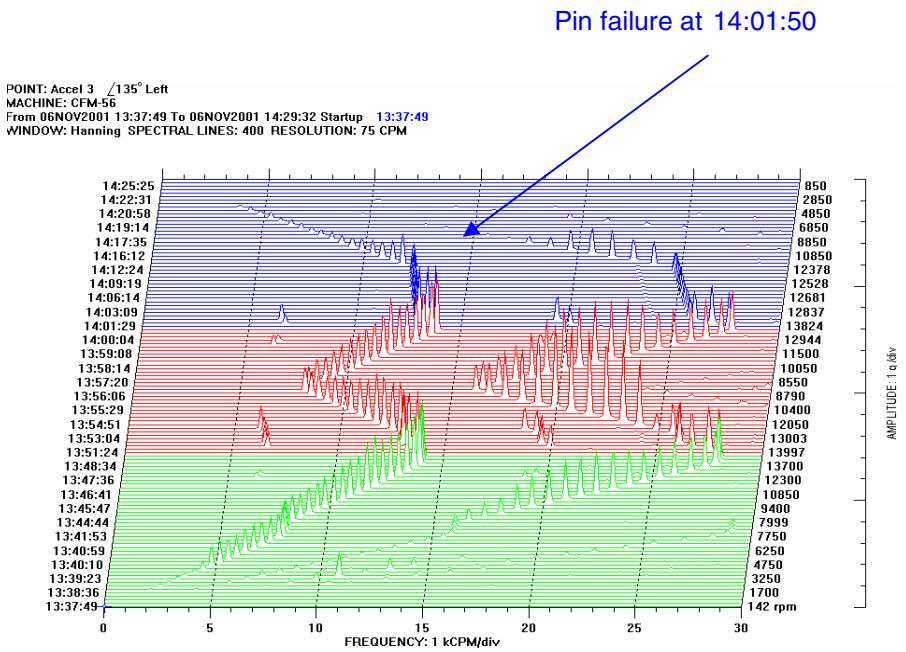

Figure 33. Waterfall Plot of Accelerometer #3 During Pin Failure

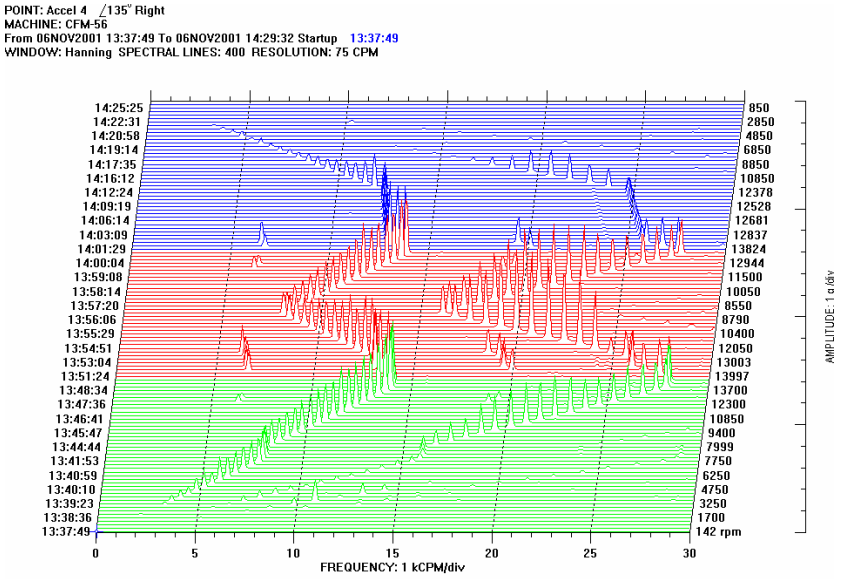

Figure 34. Waterfall Plot of Accelerometer #4 During Pin Failure

2.11 Baseline Tests

Vibration testing was resumed on December 14, 2001 using a newly designed drive spindle-to-rotor coupling attachment. Table 2 shows the testing chronology during this portion of the testing. The initial runs accounted for all seven cycles as specified in "Step 2" of the test procedure document and Table 2. Figures 35 and 36 show the synchronous acceleration amplitude during the run-up of Step 2 at Accelerometer #1 (i.e., top) and Accelerometer #3 (i.e., bottom), respectively. Figures 35 and 36 also include the average amplitude (blue curve) and the +/-3 sigma values (red curves) for Accelerometer #1 and Accelerometer #3, respectively. As shown in the figures, the baseline runs showed good repeatability. It should be noted that in these figures the nomenclature "Ampl: s2_r01" corresponds to the synchronous acceleration amplitude collected from step 2, run 1, as defined in Table 2. "Ampl: s2_r02" corresponds to step 2, run 2, and so on.

Figure 37 shows the $\pm 3\sigma$ values as a percentage of the average value for all four accelerometers during Step 2. The data in the figure can be divided into three speed ranges. Below 7 krpm, the acceleration signal is relatively small and therefore its variation is highly affected by signal noise. The speed ranges between 7-9 krpm and 11.5-12.5 krpm include the effect of structural resonance. The resonance response is highly influenced by the variation in rotor acceleration and structural damping. Both of these effects can change from run to run and therefore acceleration variation in the order of 30% could be expected. The remaining speed ranges showed potential variation in the data in the order of 10% or less. In particular, the high-speed region is the most significant from the standpoint of detecting crack-induced vibration response. The potential variation in acceleration response in this region was less than $\pm 5\%$.

Figures 38 and 39 show three acceleration run-ups in Step 4 (i.e., after the first disassembly and reassembly) for Accelerometer #1 and Accelerometer #3, respectively. For comparison, the figure also includes the average and $\pm 3\sigma$ data from Step 2 (i.e., the first seven runs). As shown in the figures, there was a significant change in the vibration response after the disassembly and reassembly. In particular, the high-speed acceleration response for Accelerometer #1 in Step 4 was more than twice the value in Step 2. It was evident that the observed change in vibration would make it difficult to detect the effect of a small flaw in the disk.

The data in Figures 38 and 39 made it clear that the disassembly and reassembly process had a significant impact in the repeatability of the acceleration response. As shown in Table 2, various tests were conducted to investigate the sensitivity of the vibration signal to different steps during the assembly process. In particular, the study included the effects of disturbing the driver-rotor alignment, the rotation of the torque coupling, and the partial disassembly and reassembly of the disk.

For simplicity, only the root-cause investigation data on Accelerometer #3 is shown. Figures 40 and 41 show the synchronous acceleration amplitude data for the average values in Steps 2 and 4 and the different cases in the root-cause investigation. As shown in Figure 40, the modification in misalignment had an impact in vibration amplitude. The increase in amplitude induced signal noise was due to accelerometer saturation. As shown in Figure 41, the removal of the turbine disk had a direct impact in the vibration response. This result is significant to the success of the project because the removal of the disk is a required step to implement the EDM flaw.

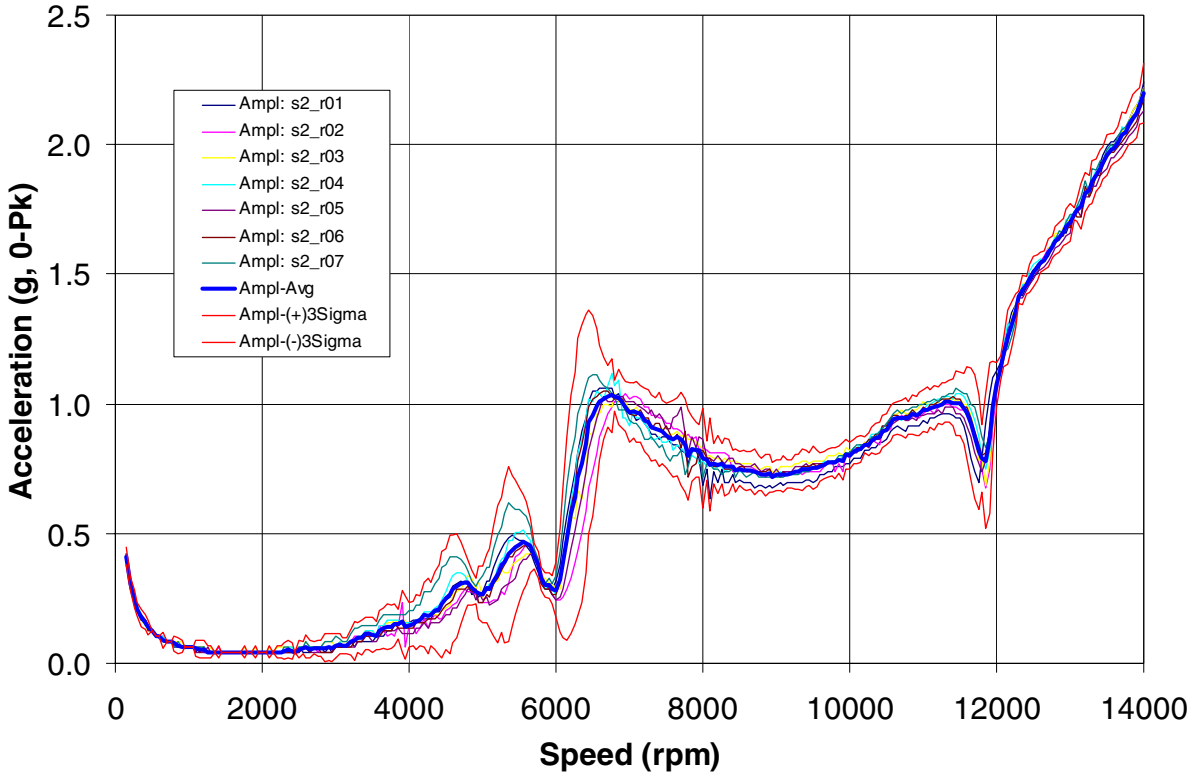

Figure 35. Vibration Amplitude During Step 2 (Accelerometer #1)

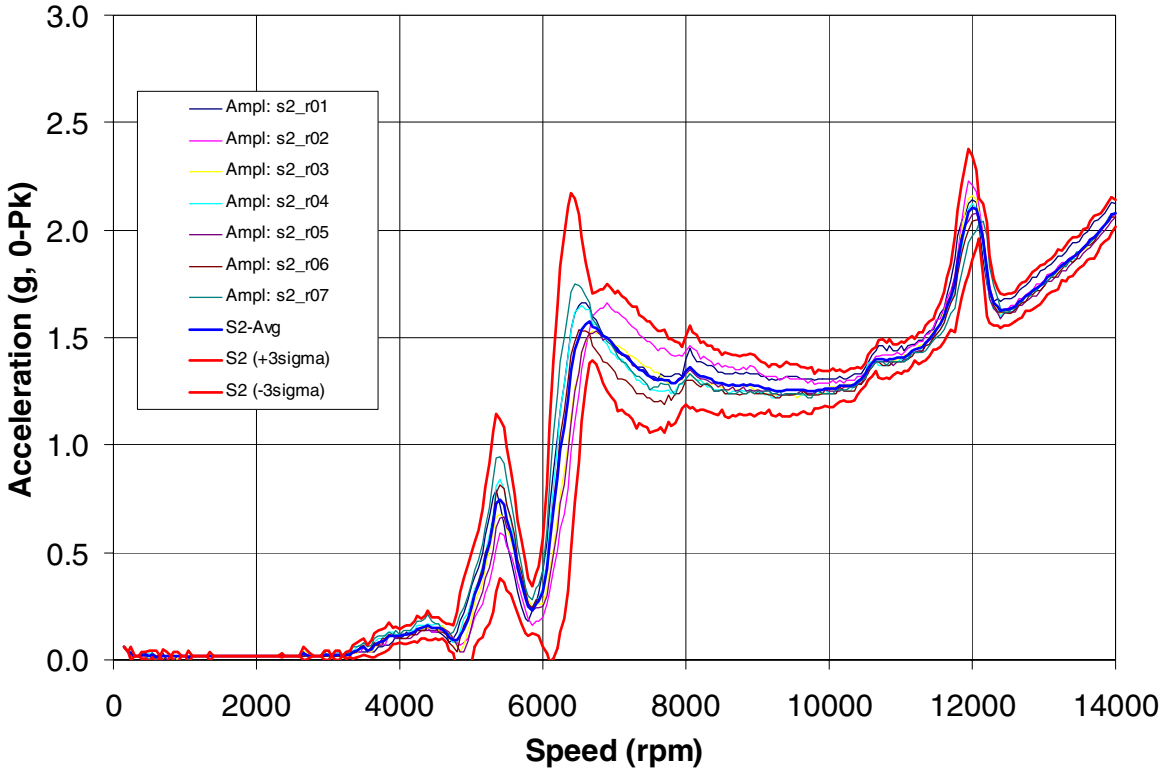

Figure 36. Vibration Amplitude During Step 2 (Accelerometer #3)

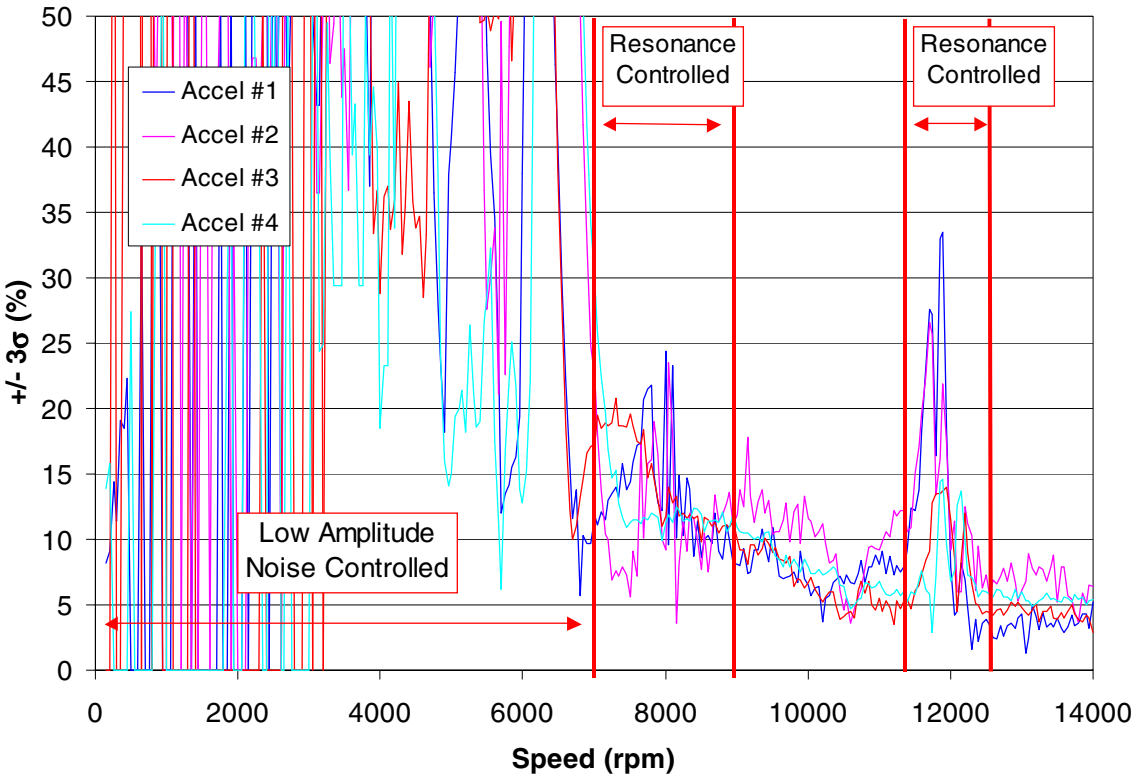

Figure 37. +/-3 σ Variation in Acceleration Amplitude During Step 2

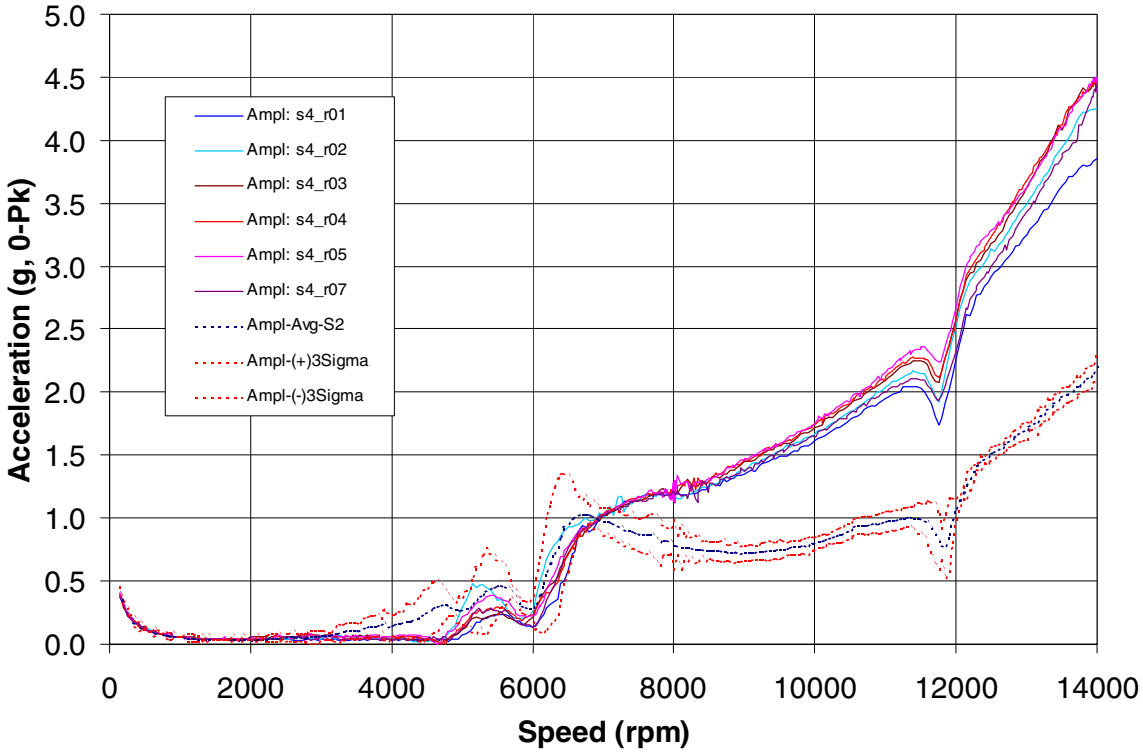

Figure 38. Vibration Amplitude Data for Early Step 4 Runs (Accelerometer #1)

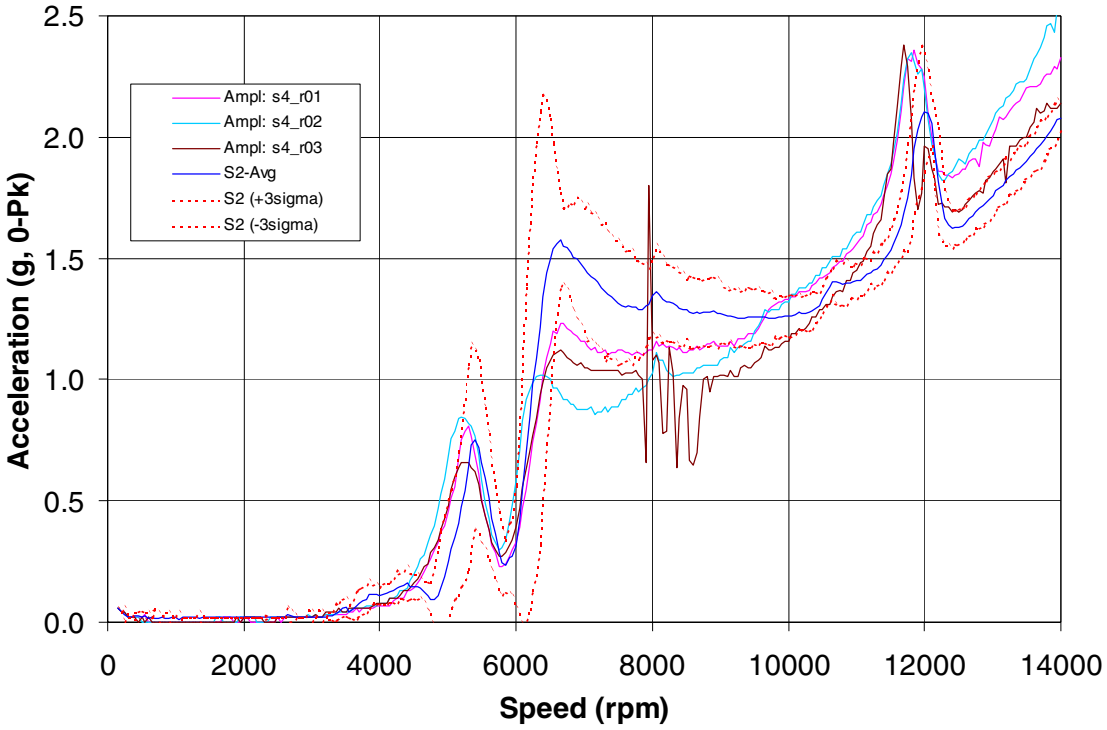

Figure 39. Vibration Amplitude Data for Early Step 4 Runs (Accelerometer #3)

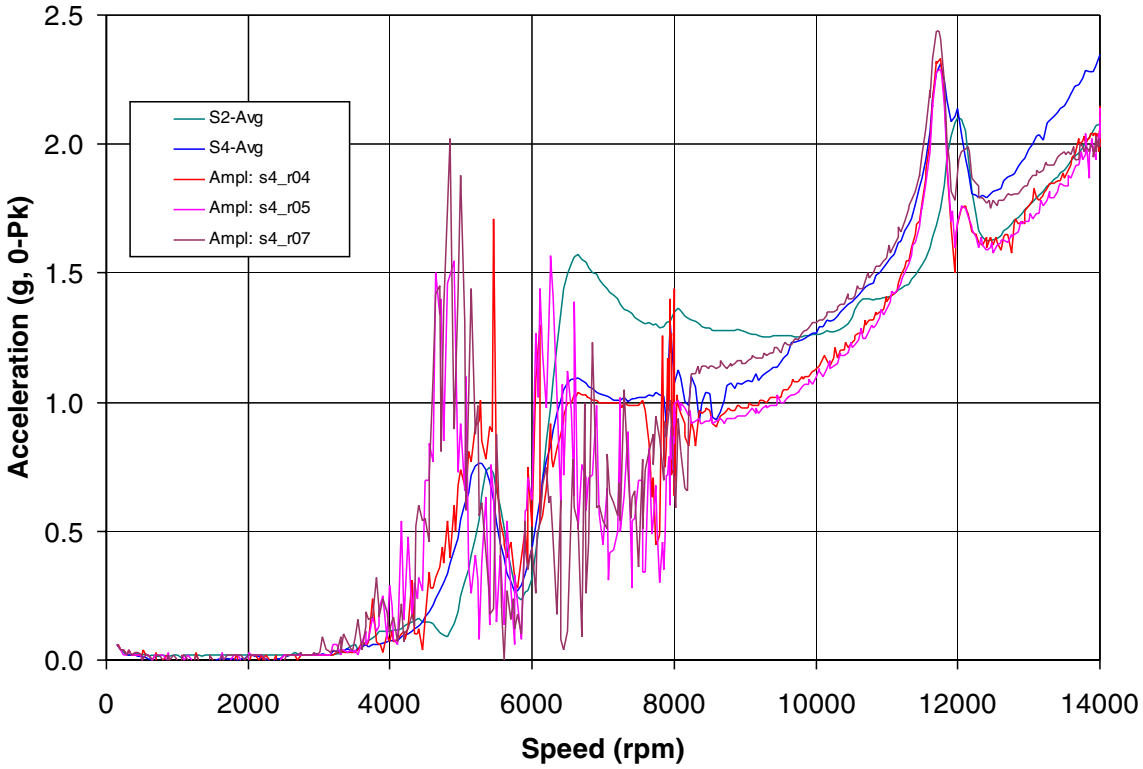

Figure 40. Vibration Amplitude Data for Early Step 4 Runs (Accelerometer #3)

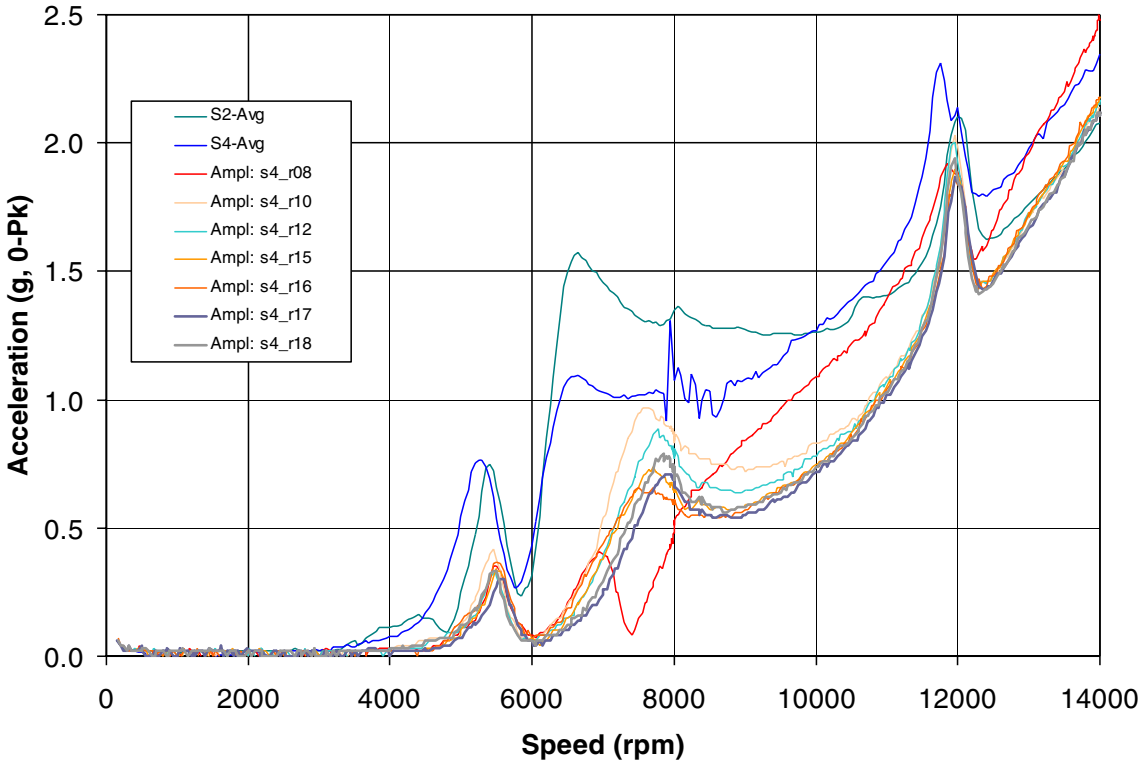

Figure 41. Vibration Amplitude Data for Later Step 4 Runs (Accelerometer #3)

Table 2. Testing Chronology

Step #	Run	Date	Description
Step 2	S2_R01	12/14/01	Original baseline
	S2_R02	12/17/01	Repeat
	S2_R03	12/17/01	Repeat
	S2_R04	12/17/01	Repeat
	S2_R05	12/17/01	Repeat
	S2_R06	12/17/01	Repeat
	S2_R07	12/17/01	Repeat
Step 4	S4_R01	01/08/02	After re-assembly: housing, disk and blades
	S4_R02	01/08/02	Repeat
	S4_R03	01/09/02	Repeat
	S4_R04	01/10/02	Disturbed alignment
	S4_R05	01/11/02	Re-centered alignment
	S4_R07	01/16/02	Torque Coupling 180°
	S4_R08*	01/17/02	After re-assembly: disk and housing
	S4_R09*	01/22/02	Repeat
	S4_R10*	01/23/02	After re-assembly: disk
	S4_R11*	01/23/02	Repeat
	S4_R12*	01/25/02	Instrumentation lead baseline
	S4_R13*	01/28/02	Repeat
	S4_R14*	01/28/02	Repeat
	S4_R15*	01/28/02	After unplug/replug inst. leads
	S4_R16*	01/2802	After inverting 1/rev signal
	S4_R17*	01/29/02	After agitating blades
	S4_R18*	01/30/02	After re-assembly chamber lid
	S4_R19	02/04/02	Housing only re-assembly

2.12 Mass Unbalance Test

As shown in the previous section, the vibration response was not repeatable. In particular, it was highly affected by the disassembly and reassembly process. An alternate approach was envisioned to detect the change in vibration due to the crack response. The approach was based on the fact that the mass unbalance effect is constant throughout the speed range while the crack effect is dominant at higher speeds due to the increased opening effect from hoop stresses. In the alternate approach, the total rotor unbalance (i.e., mass and crack-induced) would be determined from a trial mass unbalance experiment similar to the one used during rotor balancing. The total vibration due to the baseline rotor unbalance u_B and a crack-induced unbalance $u_C(\omega)$ can be expressed as

$$\vec{v}_{B+C} = \vec{H}(\omega)\times(\vec{u}_B + \vec{u}_C(\omega)), \tag{10}$$

where $H(\omega)$ is the transfer function between the disk unbalance plane and the vibration transducer. Similarly, if a trial known unbalance u_T is added to the rotor, the total vibration can be expressed as

$$\vec{v}_{B+C+T} = \vec{H}(\omega)\times(\vec{u}_B + \vec{u}_C(\omega) + \vec{u}_T). \tag{11}$$

The transfer function could be determined then from the vector subtraction of equations (10) and (11) as

$$\vec{H}(\omega) = \frac{\vec{v}_{B+C+T} - \vec{v}_{B+C}}{\vec{u}_T}. \tag{12}$$

Once the transfer function is obtained, the constant mass unbalance component could be determined from the low speed data as

$$\vec{u}_B^{\,*} = \frac{\vec{v}_B(\omega^*)}{\vec{H}(\omega^*)} \cong \frac{\vec{v}_{B+C}(\omega^*)}{\vec{H}(\omega^*)} \tag{13}$$

where ω^* is a low speed in which the crack opening effect is still negligible. The vibration due to the calculated mass unbalance can be expressed as

$$\vec{v}_B^{\,*} = \vec{H}(\omega)\times(\vec{u}_B^{\,*}) \tag{14}$$

Once the constant mass unbalance is obtained, the crack-induced unbalance could be extracted from

$$\vec{u}_C(\omega) = \frac{\vec{v}_{B+C} - \vec{v}_B^{\,*}}{\vec{H}(\omega)}. \tag{15}$$

The proposed alternate approach assumes that the mass unbalance, crack-induced unbalance and trial unbalance are located in the same plane of the disk. Furthermore, the approach also assumes

that the only type of baseline rotor excitation (i.e., without a crack) is due to a frequency-independent mass unbalance (e.g., no driver to rotor misalignment).

The applicability of the proposed approach was investigated using trial mass unbalances. Figure 42 shows the vibration amplitude at Accelerometer #1 due to two different levels of trial known unbalances at the same angular location (i.e., aligned with the key-phasor mark). As shown in the figure, the increase in the additional unbalance induced a further increase in the vibration amplitude

The ratio of the baseline vibration to the vibration from unbalance trials can be expressed as

$$\frac{\vec{v}_B}{\vec{v}_{B+T} - \vec{v}_B} = \frac{H(\omega)\times\vec{u}_B}{H(\omega)\times\vec{u}_T} = \frac{\vec{u}_B}{\vec{u}_T} = \frac{|\vec{u}_B|}{|\vec{u}_T|}\angle(\phi_B - \phi_T). \tag{16}$$

As shown in equation (16), a frequency-independent baseline unbalance would yield a vibration ratio with constant amplitude over the speed range. Figure 43 shows the amplitude of the ratios of the baseline vibration amplitude to the vibration due to the added known unbalance weights. As shown in the figure, the amplitude of the vibration response ratios was found to be frequency-dependent. The results on this figure demonstrated that the required constant mass unbalance assumption was not valid for this rotor arrangement and therefore the proposed alternate approach was not appropriate to investigate the crack-induced unbalance response.

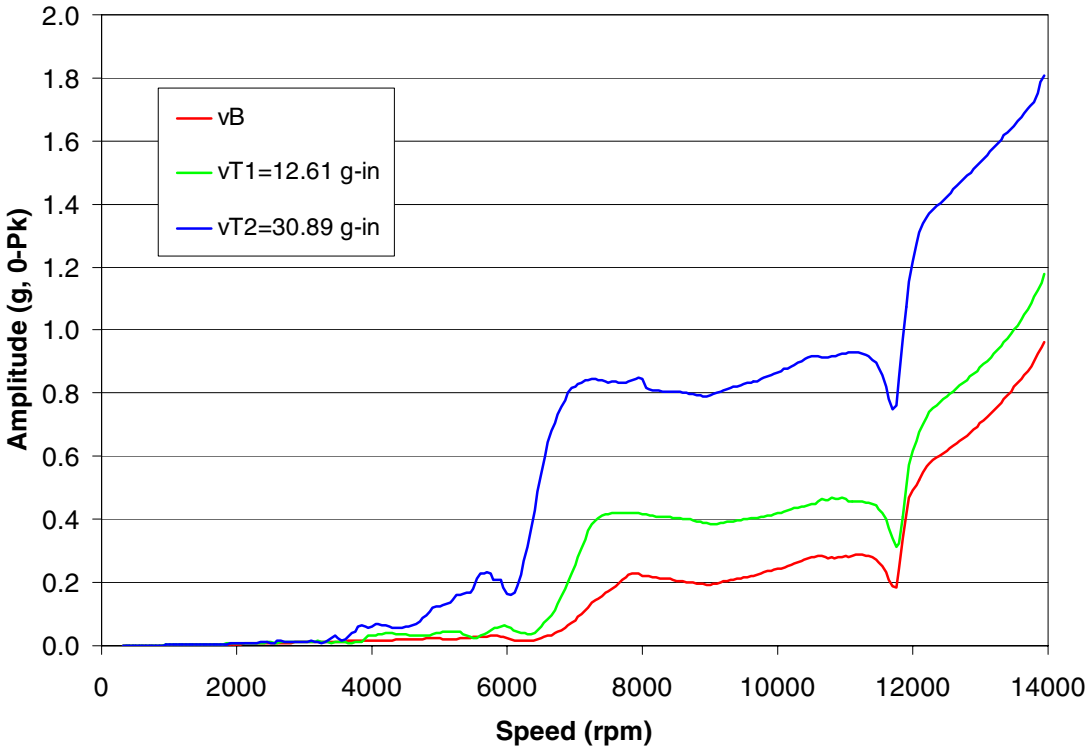

Figure 42. Vibration Amplitude Data for Baseline and Two Different Levels of Trial Unbalance (Accelerometer #1)

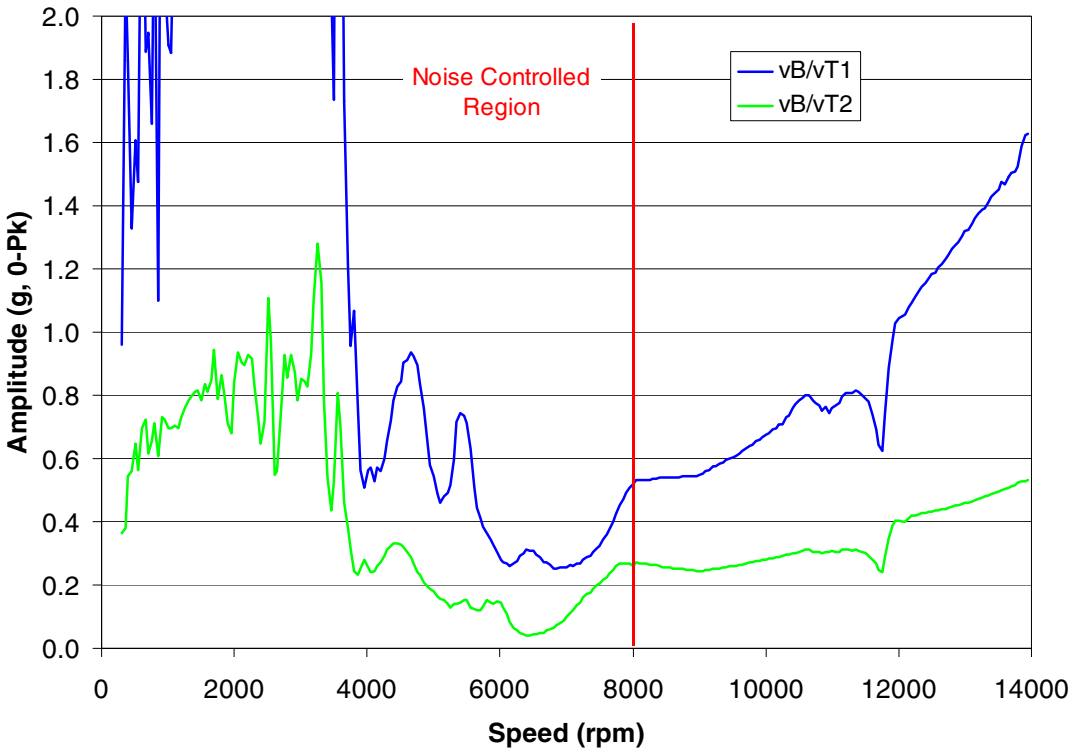

Figure 43. Amplitude of Baseline to Trial Unbalance Vibration Ratios (Accelerometer #1)

2.13 EDM Flaw Test

The CFM56 disk with the 200-mil EDM flaw (Figure 44) was tested on February 27, 2002. Figure 45 shows the synchronous acceleration amplitude for the baseline, EDM and vector difference cases at Accelerometer #1. The figure also includes the curve fitting to determine the power of the different cases. In all three cases the curve fit was performed using data in the 9-14 krpm range. Using the high-speed data only will help minimize the effect of the critical speeds in the vibration response. As shown in Figure 45, the disk with the EDM flaw had a significant increase in vibration amplitude. In addition, the fitted curve for the disk with the EDM flaw has a power smaller than the baseline. This reduction can also be seen in the vector difference (i.e., amplitude and phase) response. The resulting response has a power smaller than the baseline. This is opposite to the expected result in the case that the added vibration is due to opening of the crack as function of speed. Based on past experience with the test setup, it is more likely that the observed change in vibration is due to reassembly variability and not due to the effect of the EDM flaw.

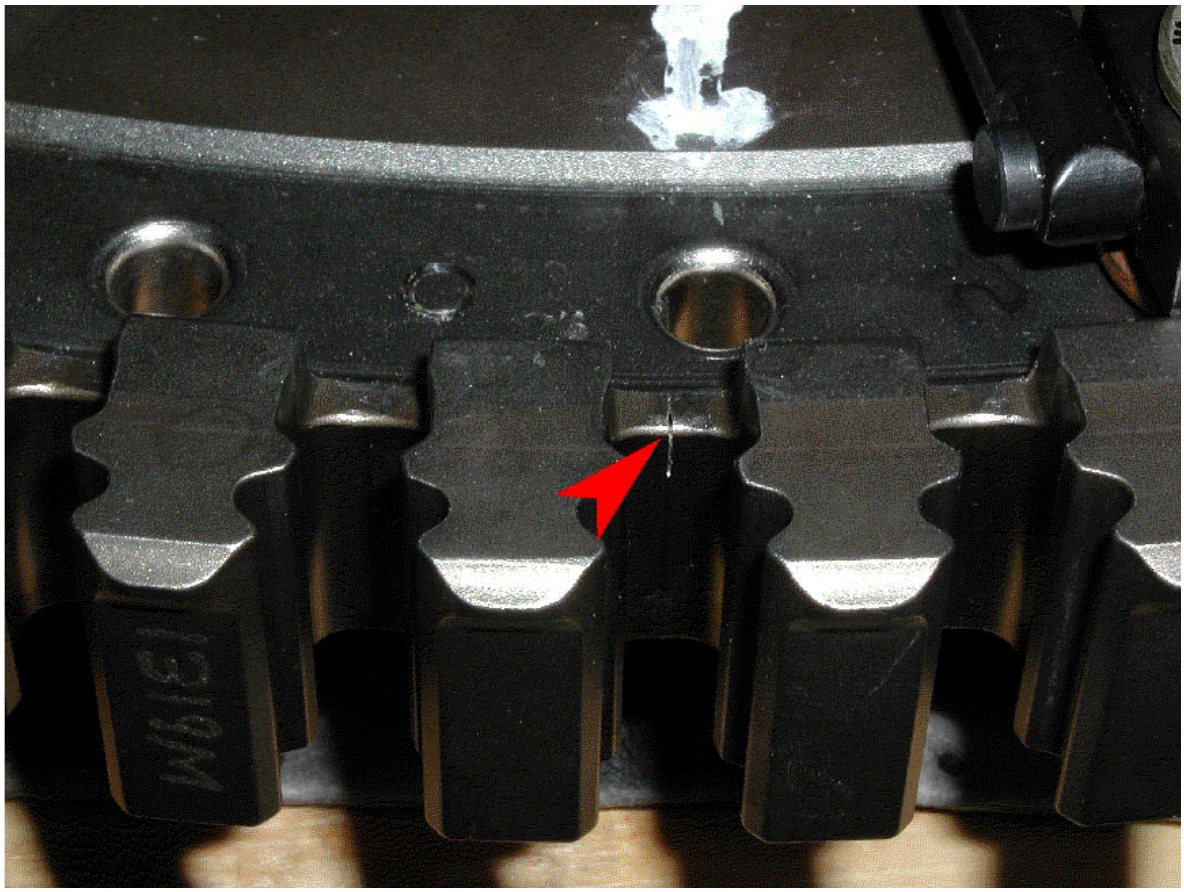

Figure 44. EDM Flaw in HPT Dovetail Slot

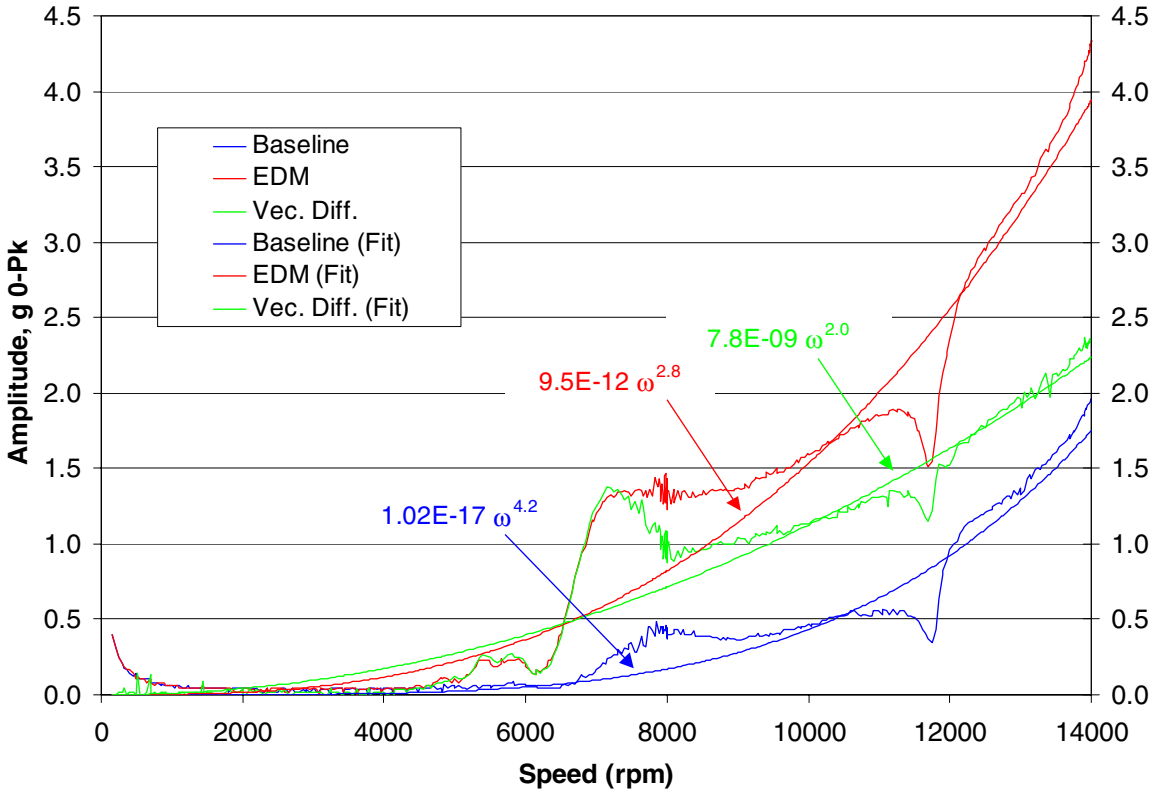

Figure 45. Vibration Amplitude Before and After the EDM (Accelerometer #1)

2.14 Radial-Mode Disk Crack Detection System Results

The sub-scale model disk test was unsuccessful in demonstrating disk crack detection. When the algorithm was applied to the data, the variation in the rotor unbalance signal seen after the 0.200-inch deep crack was machined in the disk and the rotor was re-assembled was found to be quite large. This large variation in the unbalance signal masked the vibration signal shift that was expected from the crack. This sub-scale disk test did show that changes to the baseline unbalance signal due to disassembly and reassembly of the rotor assembly can be larger than originally expected and demonstrated the importance of quantifying and minimizing the amount of this variation. These important lessons were applied to the test plan for the full-scale test. This test plan included steps to quantify the statistical variation of the baseline unbalance signal due to disassembly and reassembly of the rotor, and also defined steps to maintain uniformity in the disassembly/reassembly process to minimize this variation.

The full-scale CFM56 HPT rotor assembly test was also unsuccessful in demonstrating disk crack detection. Prior to the full-scale test, it was predicted that the crack-induced unbalance would be in the order of a small percentage of the mass unbalance. Then during the baseline tests, it was again found that the disassembly and reassembly process had a significant impact on the repeatability of the vibration signature. Although steps were taken to maintain uniformity in the disassembly and reassembly process, significant variation in the unbalance signature persisted.

For this full-scale test program, there was a requirement to perform a disassembly and reassembly of the HPT rotor assembly in order to remove the HPT disk and machine the crack into the disk's dovetail slot. The change to the baseline vibration signature as a result of the disassembly and reassembly tasks had a direct impact on the success of detecting the crack-induced unbalance. When the algorithm was applied to the data after the crack was machined into the disk, the rotor unbalance signal had varied enough to prevent the detection of the crack's vibration signature.

Throughout full-scale HPT rotor testing, it was demonstrated that the baseline vibration signature was very repeatable from one run to the next as long as no hardware disassembly/reassembly occurred. This information was significant because the intended use of the crack detection technology is within an engine environment. Here there would typically be no disassembly and reassembly of engine hardware, and an initial baseline vibration unbalance signal could be established. Then in the event that a disk crack does initiate and propagate to sufficient size, it becomes detectable by monitoring the change in the total vibration unbalance signature relative to this pre-established baseline.

3.0 Torsional-Mode Disk Crack Detection System

The PSU ARL torsional-mode disk crack detection system was initially developed for the Southern Company as a method of detecting cracks in power generation turbine blades. This system is based on the principle that if a crack of sufficient size occurs the component stiffness will change resulting in a measurable shift in the natural frequency of the component. The intent under this contract was to extend the technology to the on-line detection of aircraft engine disk cracks by monitoring shaft vibration measurements for detecting changes in system torsional natural frequencies in the presence of a disk crack. This technology was developed and tested as part of a subcontract issued by GE Aircraft Engines under this contract. The subcontract required GE AE to design, manufacture, and deliver a desktop spin rig for a sub-scale turbine wheel provided by PSU. The subcontract also required PSU to develop and test their signal detection system during a CFM56 High Pressure Turbine rotor rig test performed at GE Aircraft Engines.

3.1 Principle of Torsional-Mode Disk Crack Detection System

The PSU ARL crack detection system is based on measuring the torsional natural frequencies of a rotor disk assembly at non-invasive locations such as the shaft. The detection of cracks in turbine disks or blades is deduced by observing shifts in the coupled blade bending and shaft torsional natural frequencies. This detection system consists of a torsional vibration transducer, demodulator, analog-to-digital converter, and a zoom-capable fast Fourier transform (FFT) analyzer. The noninvasive transducer consists of an infrared fiber optic probe (with electronics and light source) which is positioned close to the shaft that is encoded with equally spaced stripes (zebra tape) as shown in Figure 46. By observing the fluctuation (via demodulation of the signal) in the time spacing of the stripes (Figure 47), various rotating assembly natural frequencies may be observed and trended. To maintain the required high dynamic range, the demodulation is performed using an analog incremental (zero crossing) demodulator or digital demodulator. The signal from the transducer is then processed using the FFT analyzer, and the component natural frequencies are identified. As the structural characteristics of rotating assembly components change, the natural frequencies will be observed to shift. Based on these shifts, appropriate action can be planned and implemented by maintenance personnel. Prior to initiating this contract, PSU ARL had performed initial demonstrations of this concept on laboratory rotor system tests that showed clear frequency shifts for a cracked "blade" (Figure 48). The assumption in this methodology is that the introduction of a crack changes component stiffness enough to result in a measurable shift in natural frequency of the component. Thus whether the cracked component is

the shaft, the disk or the blade, a rotor disk assembly natural frequency shift is actually measured. Thus, disk cracks will induce changes in torsional natural frequencies of the disk and blades and, given sufficient shift and adequate instrumentation dynamic range, may be used as a diagnostic and prognostic tool. At this time there is no means to isolate which component is faulty (cracked) using this technique alone.

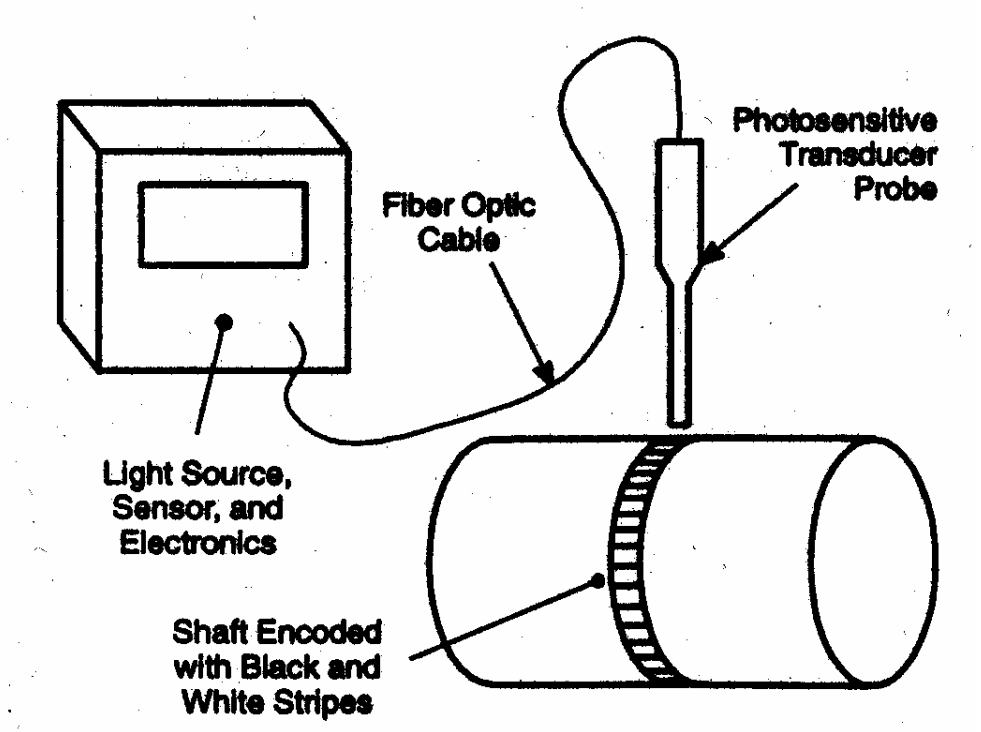

Figure 46. Schematic of Transducer Arrangement

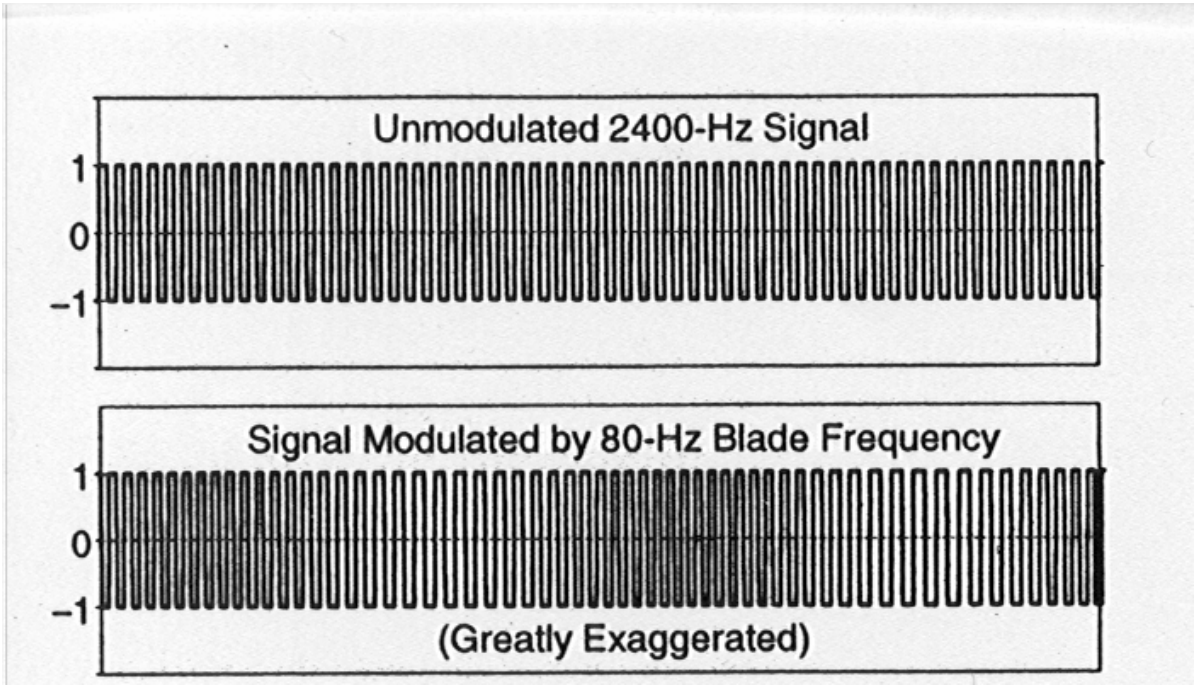

Figure 47. Modulation of Encoded Shaft Light Pulses

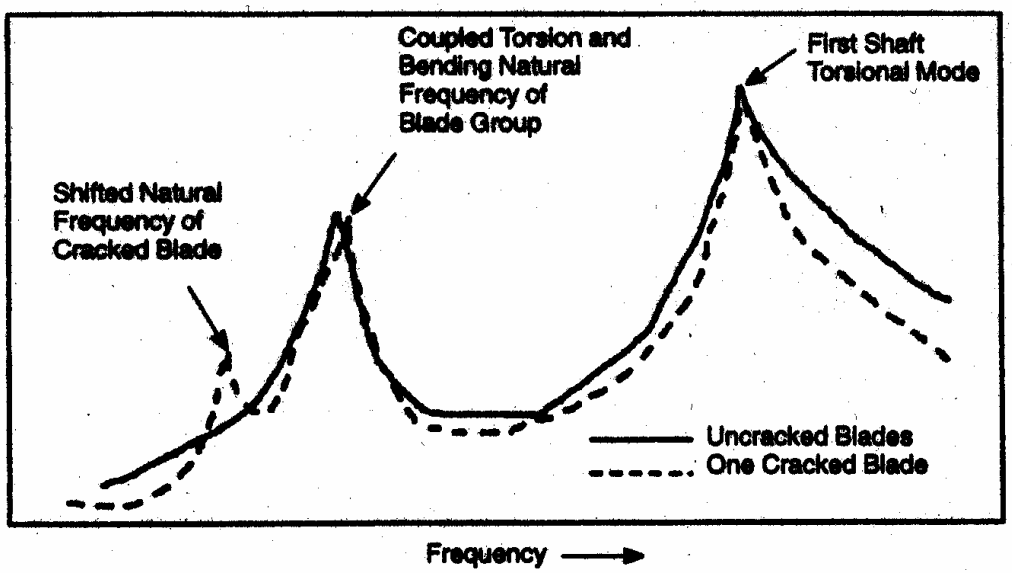

Figure 48. Previous Results of Blade Crack Detection on a Desktop Rotor

3.2 Desktop Spin Rig for Sub-scale Turbine Wheel

GE Aircraft Engine's Test Facility Engineering organization designed and manufactured a desktop spin rig for a sub-scale turbine wheel provided by PSU. This spin rig was to be used by PSU to continue development of their torsional-mode crack detection system on a sub-scale rig representative of an aircraft gas turbine engine rotor assembly. The turbine wheel contained integral blades that were proportionally similar to the blades of a full-scale CFM56 High Pressure Turbine rotor assembly.

The desktop spin rig, shown in Figure 49, consisted of the PSU turbine wheel on the left hand side of the picture, and an encoder wheel on the right hand side. The encoder wheel is attached to the turbine wheel by a shaft that is an integral part of the turbine wheel. The wheels rotate by directing facility shop air on the turbine wheel blades. The desktop rig had thermocouples installed near the two bearings for temperature monitoring, and it had a safety shield cover for protection of the facility in case of a turbine wheel failure. A picture of the rig with the safety shield installed is shown in Figure 50. PSU installed the desktop spin rig in their laboratory and reported that the desired speed of 10,000 revolutions per minute was measured using an electrical sensor installed next to the encoder wheel teeth. Sketches of this desktop spin rig assembly are shown in Figures 51 and 52. Unfortunately, due to contract cost overruns in other areas deemed to be of higher priority, actual testing using this rig was not conducted during this project.

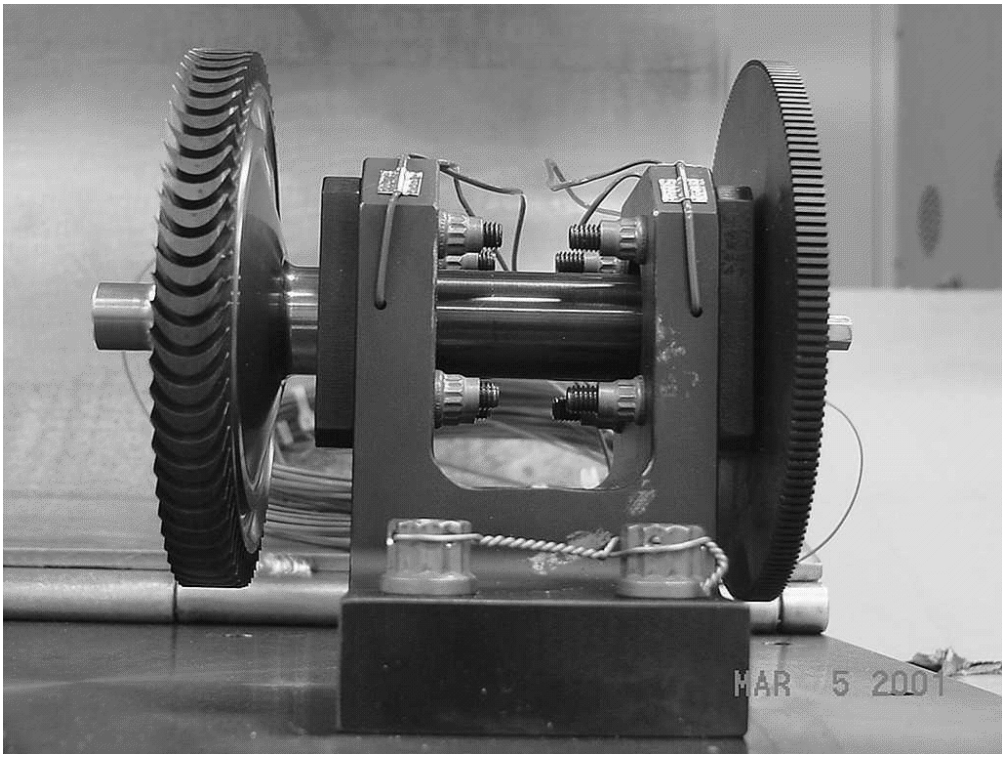

Figure 49. Desktop Spin Rig for PSU Sub-scale Turbine Wheel

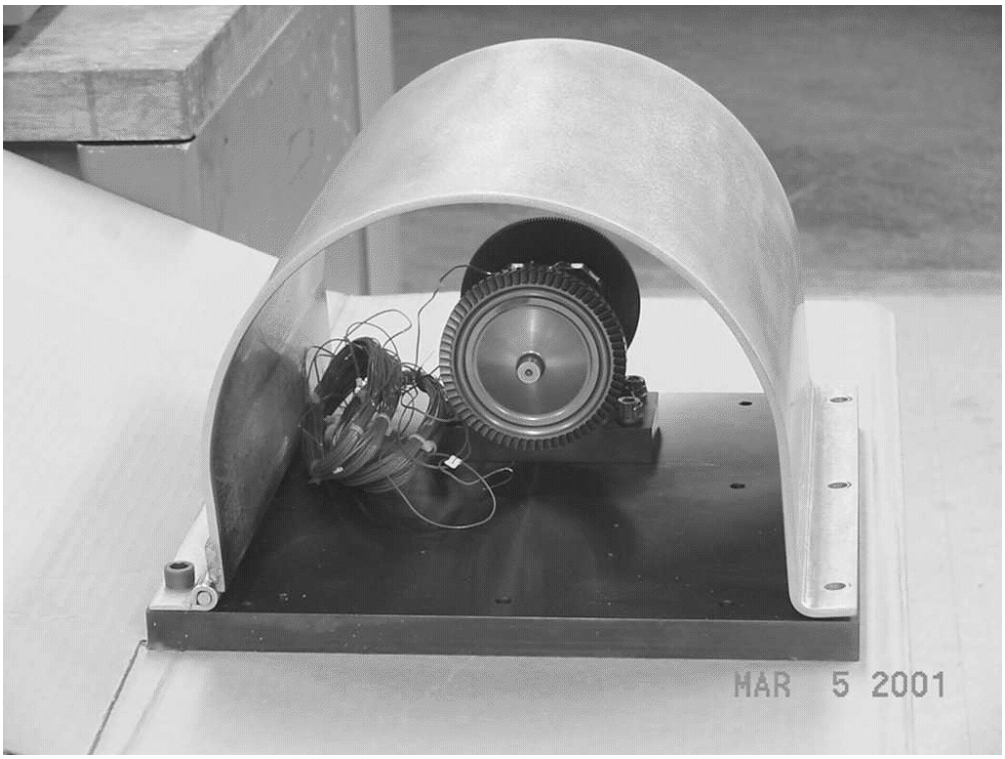

Figure 50. Desktop Spin Rig with Safety Shield Installed

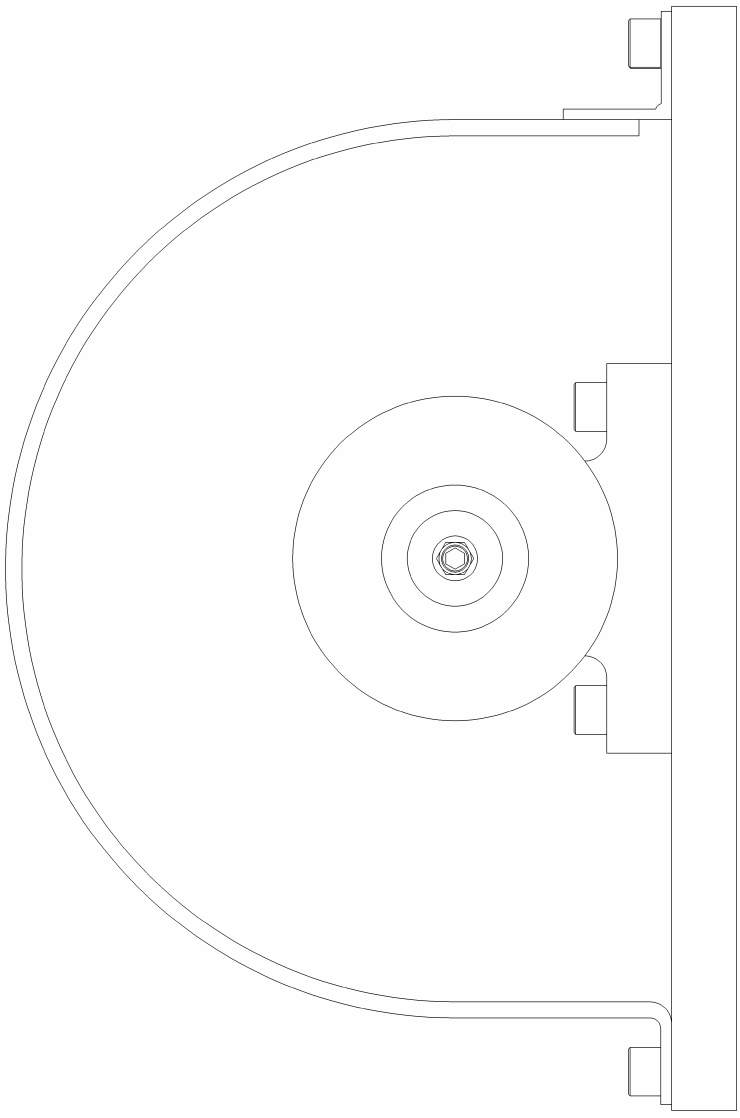

Figure 51. Desktop Spin Rig Assembly Sketch (Sheet 1 of 2)

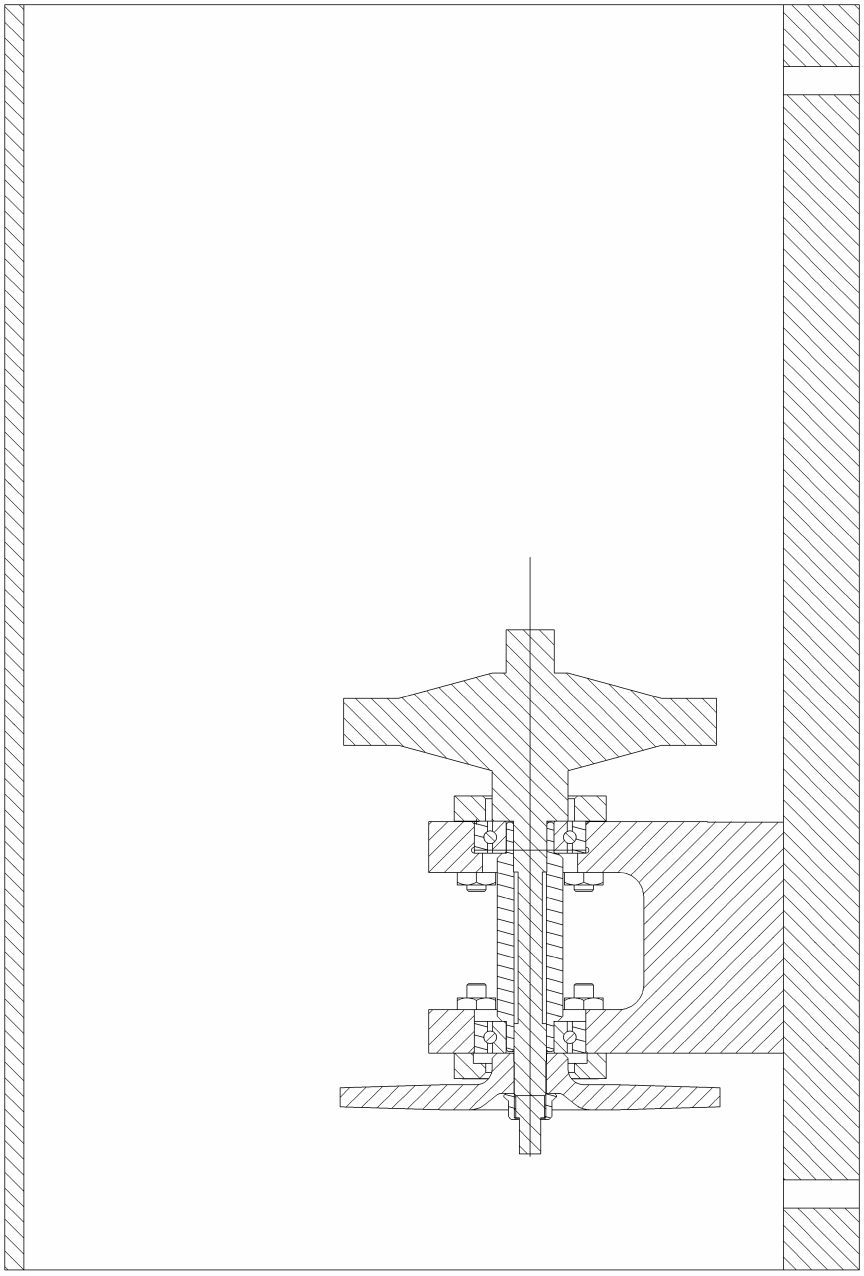

Figure 52. Desktop Spin Rig Assembly Sketch (Sheet 2 of 2)

3.3 HPT Disk Component Test of Signal Processing System

PSU ARL and GE Aircraft Engine's Test Facility Engineering organization demonstrated the PSU signal detection and processing system as part of a Warm Air Rig Test performed on a CFM56 High Pressure Turbine rotor assembly. The HPT rotor assembly was a full-scale assembly and was tested with a full-scale LPT rotor assembly in an enclosed chamber that had warm ambient and turbine cooling air capability. The test provided a realistic environment for establishing a baseline (non-cracked) measurement signature for the torsional-mode crack detection system. The test description and results are provided below.

The goal of the testing was to demonstrate the feasibility of detecting blade natural frequencies on the CFM56 HPT rotor (as modified for the testing). Figure 53 shows the HPT bladed disk used in this testing.

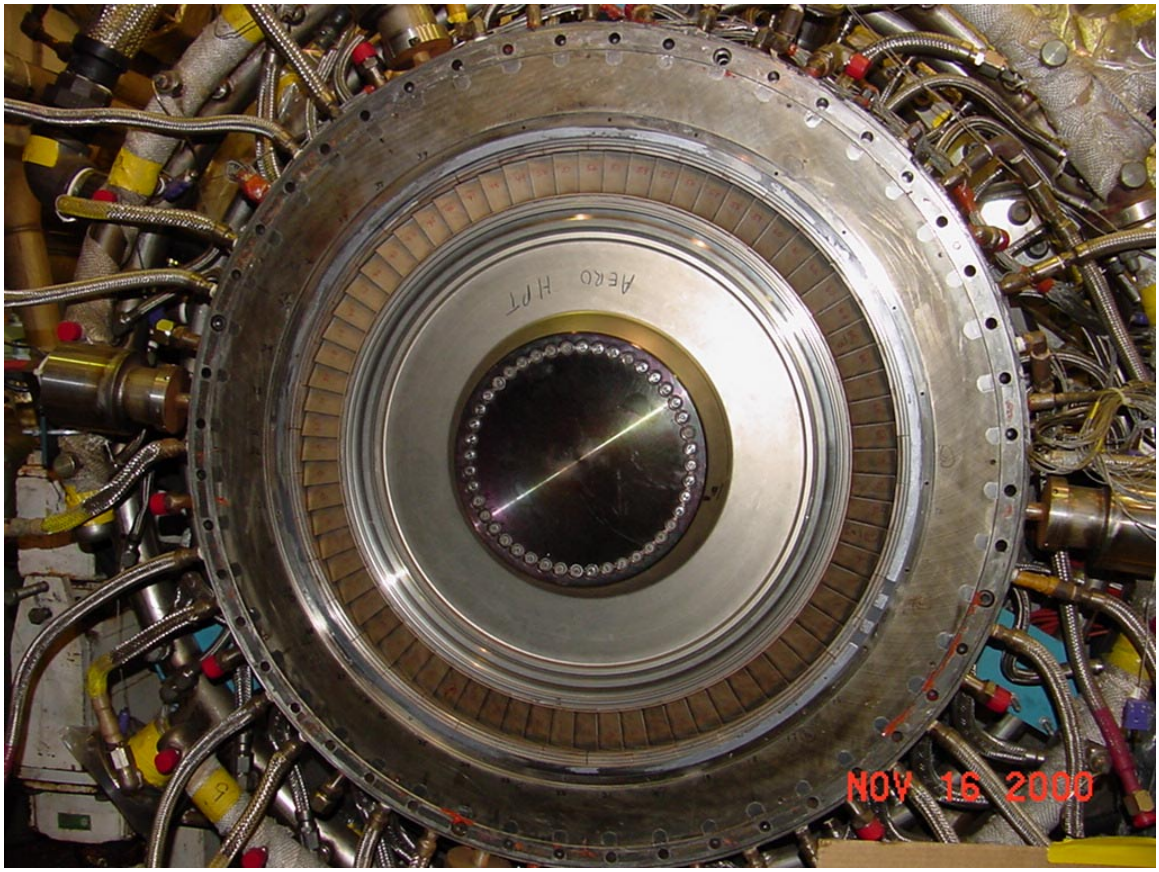

Figure 53. HPT Disk Assembly

Instrumentation**:** The HPT shaft was instrumented by applying a 200-stripe tape on the flange of the torque cell (which was as close as the tape could be mounted to the HPT disk without disassembly of the test rig) and two fiber optic probes. The tape was printed by a GE AE subcontractor, and consisted of adhesive-backed paper with a Mylar-like coating. Instrumentation and wiring was completed on 3 January 2001. Figure 54 shows the installed transducer system.

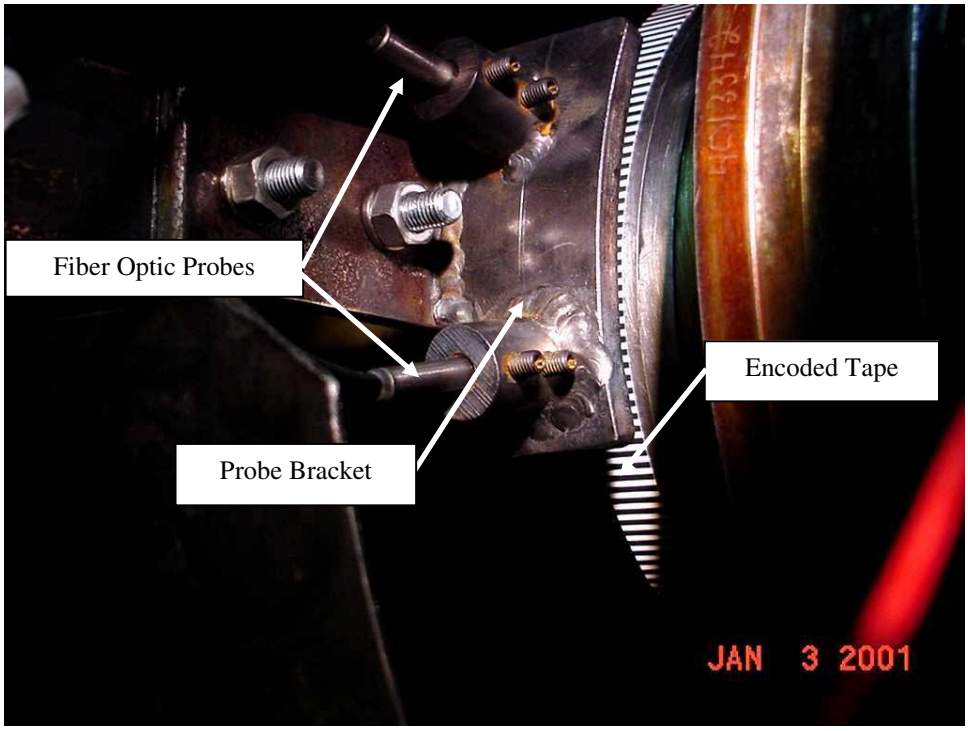

Figure 54. Transducer Installation

In addition, signals were taken from the warm air test apparatus, including the one-per-rev tachometer and the 60-tooth speed gear. The tachometer was required for the signal processing algorithms, and the 60-tooth gear was used as backup for the encoded tape. Figure 55 shows the gear. Note that the gear is actually located slightly closer to the HPT disk than the encoded tape.

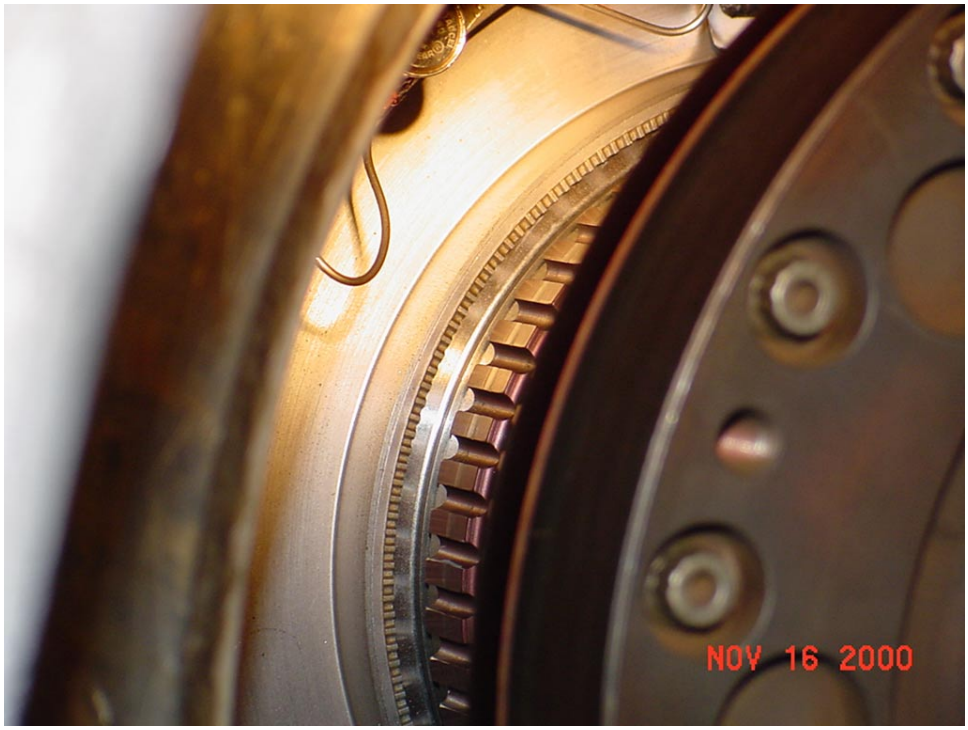

Figure 55. 60-Tooth Speed Gear

Unfortunately, during testing the tape came off of the shaft at about 5000 RPM, and no meaningful data was obtained from the tape. However, some encouraging results were obtained from the 60-tooth wheel. Figure 56 shows the spectrum of the data from the 60-tooth wheel taken at two speeds. The frequency range of the data is limited to one-half the number of teeth times the speed of the shaft, or about 4500 Hz. Note that torsional natural frequencies of the shafting system should change very little with speed, and coupled blade and shaft torsional modes increase very slightly with speed due to stiffening by axial force. So, we expect frequencies that are not shifting with speed. Clearly, there are a number below 2000 Hz, but we do not expect the blades to have frequencies below about 2000 Hz.

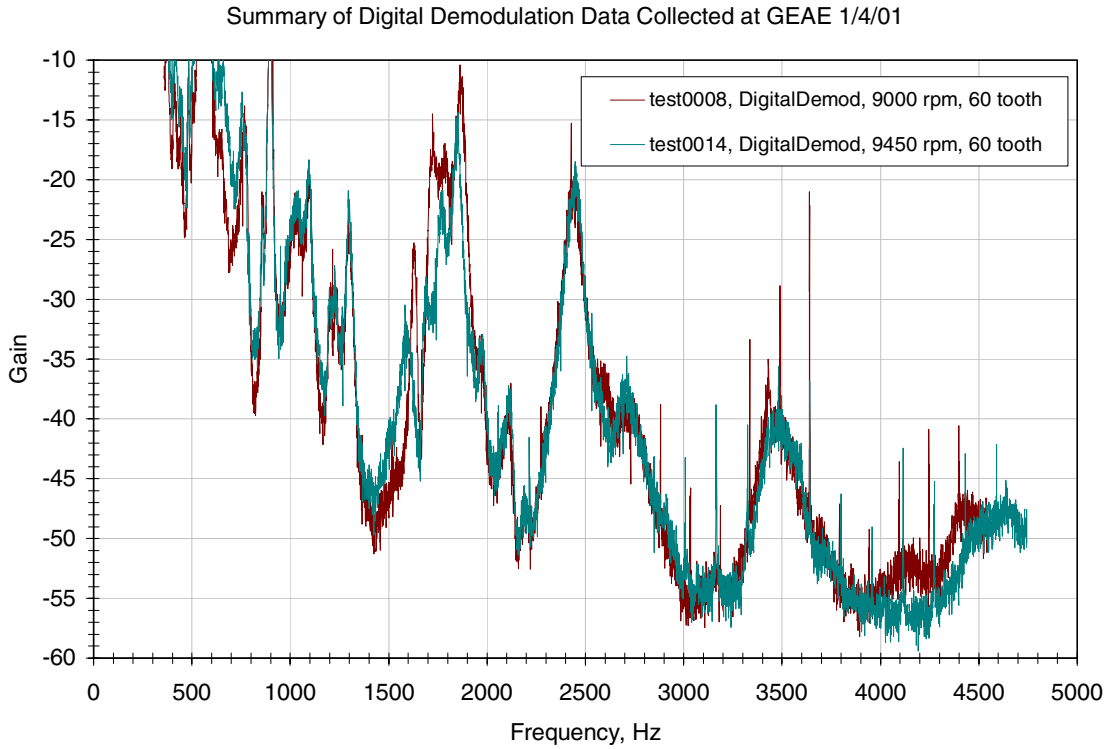

Figure 56. Demodulated Spectrum of Data from 60-tooth Wheel

GE AE performed modal testing on three blades like those installed in the test HPT disk. The results for one of the blades are shown in Figure 57. The spread of the frequencies is shown in Table 3.

Table 3. Results of GE AE Blade Modal Testing

	Mode 1	Mode 2	Mode 3	Mode 4
Blade F12	2450	3943	6038	8409
Blade C14	2413	3853	6091	8469
Blade B7	2434	3875	5994	8364
Average	2432	3890	6041	8414
Std. Dev.	19	47	49	53

Many of the peaks in the low frequency range (less than 2000 Hz) that do not change with speed may be associated with shaft torsional natural frequencies. A torsional rotordynamic model would shed light on these frequencies.

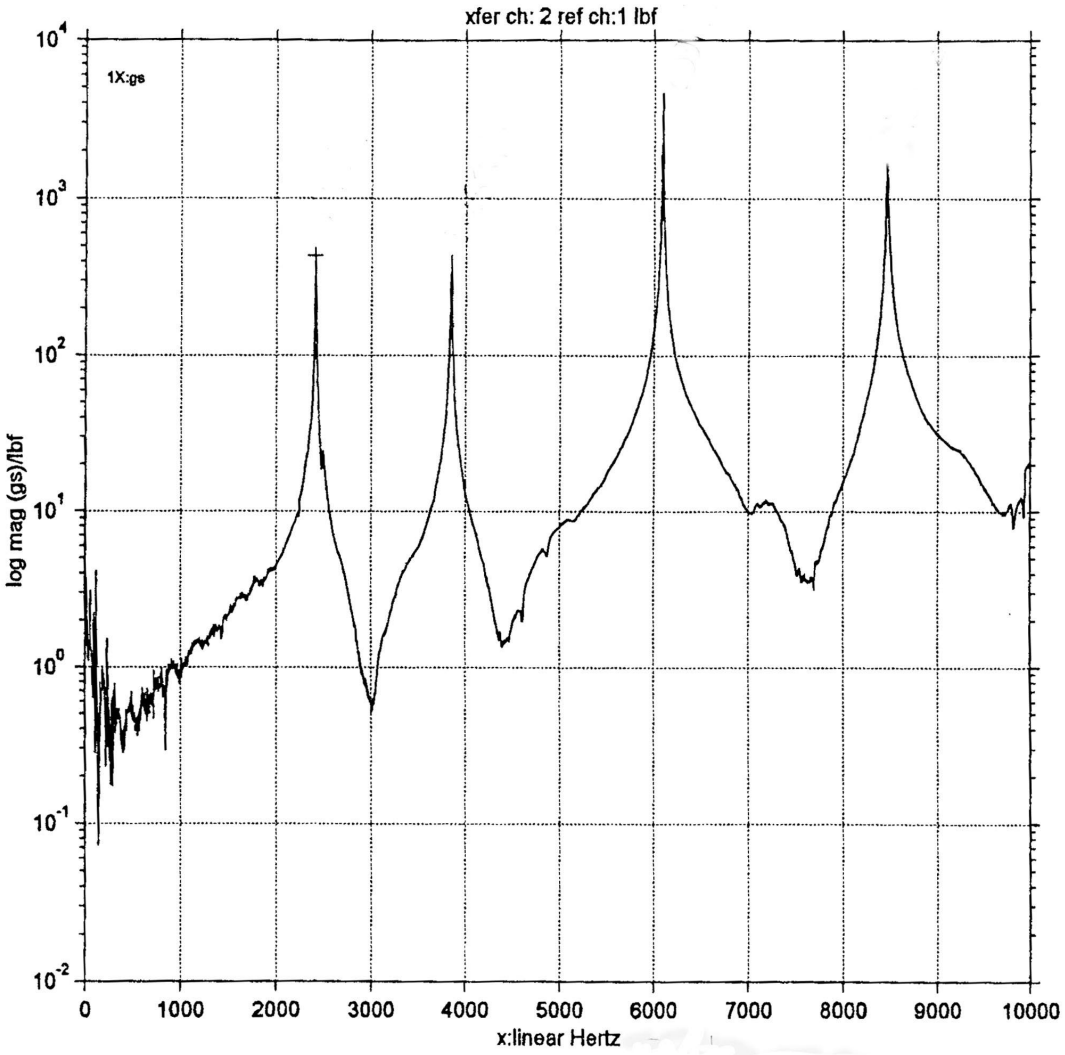

Figure 57. Modal Test Results from Blade C14

Figure 58 shows the demodulated spectrum in the range associated with the first two blade frequencies. Note that the first peak, near 2400 Hz, is very close to the lowest frequency from the GE AE blade test data. The next peak, near 3500 Hz is significantly (about 10-12%) lower than the second peak in the GE AE blade test data. Earlier experimental and analytical work, however, indicates that blade natural frequencies can be significantly altered by coupling with shaft torsional modes. In laboratory rotors, this shift was found to be more than 30%, and also found to be higher or lower than blade impact testing, depending on coupling parameters. Clarification of coupling effects requires torsional rotordynamic modeling of the rotor system, including blades.

Summary**:** The data from the 60-tooth wheel show promise, and there are definite indications of natural frequencies close to the expected blade natural frequencies. The effects of torsional coupling should be clarified by a dynamic torsional model.

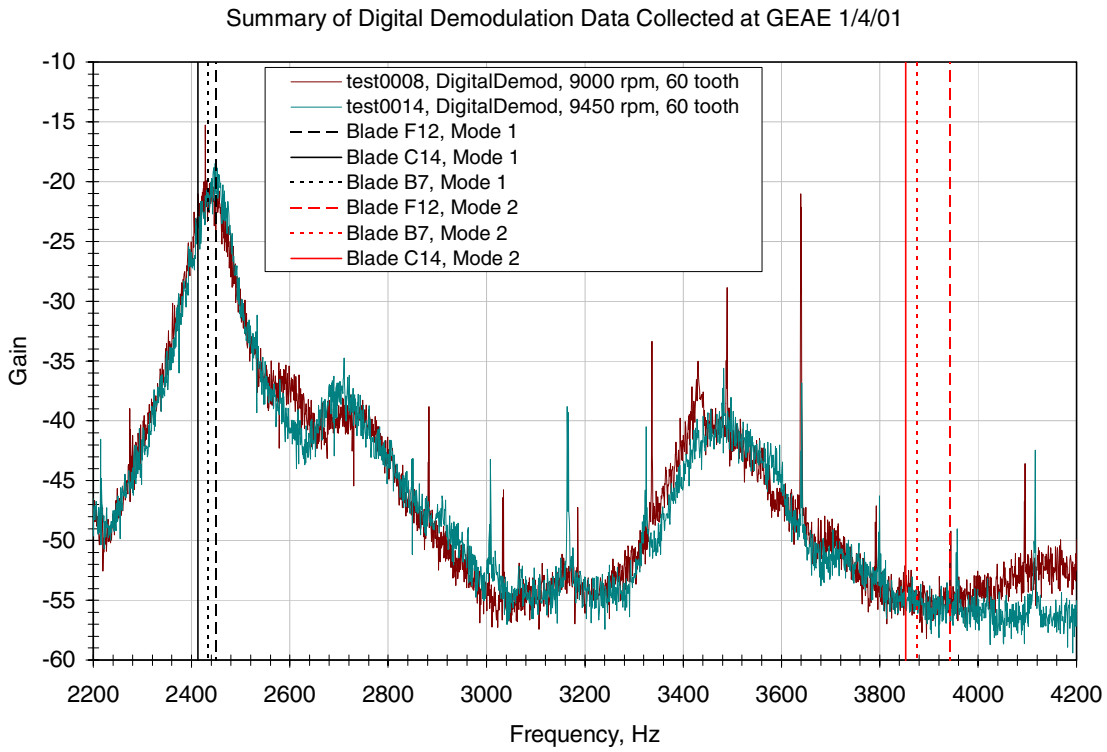

Figure 58. Demodulated Spectrum on the Blade Frequency Range

Recommendations**:** Further testing and dynamic modeling of the HPT bladed disk is recommended. This would be greatly facilitated by the addition of an encoded wheel with a higher number of pulses on the wheel to increase the analysis frequency band (currently limited to about 30 times the speed in Hz), and the dynamic range (previous testing indicates an increase of about 5 dB dynamic range for a doubling of the number of pulses on the encoded wheel). On the basis of previous research, it was also determined that coupling between blade bending/torsional modes and shaft torsional modes can cause significant effects on the natural frequency. Torsional rotordynamic modeling of the shafting system should be performed to clarify the effects of coupling.

3.4 Torsional-Mode Disk Crack Detection System Results

The results of the Warm Air Rig Test performed on a CFM56 High Pressure Turbine rotor assembly demonstrated the feasibility of detecting blade natural frequencies in the torsional domain. These encouraging results are tempered by the uncertainty associated with the effects of coupling on the blade natural frequencies. Finite element rotordynamic modeling should be performed to clarify these effects. This technique could be used for the detection of a crack in the disk at the root of a blade, or a crack in the blade itself. However, in order to assess the value of this technique for the CFM56 HPT, experimental and analytical work is required to assess (1) the shift in natural frequency expected for a significant or a propagating crack(s); (2) the detectability of this shift in a single blade in the context of a multi-blade, multi-row installation; and (3) correlation of crack characteristics with normal blade natural frequency shift.

4.0 Model-Based Fault Tolerant Control

The GE AE Model-Based Fault Tolerant Control work is an innovative technique that improves the control system's fault detection and isolation performance over the current techniques of hardware redundancy and simple "Math models" or local correlation models by analytically estimating a failed sensor value from other sensor measurements. This work has been developed under previous contracts with the Air Force, DARPA and NASA. It is being advanced under NASA Aviation Safety Program funding to address safety significant propulsion system malfunctions such as engine surge/stall and loss of thrust control (LOTC) that may result in in-flight engine shutdowns or aborted takeoffs. Under this contract GE AE first conducted a search of revenue service engine shutdown data in order to obtain candidate engine fault events that could be improved using a model-based fault tolerant design. A simulation of one revenue service fault condition was then made and tested with new control logic for the accommodation of the simulated fault condition.

4.1 Engine Field Event Study

At the initiation of this task information on recent engine field events, including in-flight shut down (IFSD), loss of thrust control (LOTC), aborted takeoff (ATO), overspeed, and surge/stall events were collected and analyzed. In particular, failures in critical control and gas-path components such as speed sensors, variable stator vanes (VSVs), and compressor inlet temperature (CIT) sensors were considered. As the fault information was collected, it was analyzed and classified by possible cause. The findings of this effort are shown in Table 4. Note that all events detailed in this report have been processed through GE's Product Support Engineering (PSE) organization. Measures have been put in place to prevent recurrences of these incidents in the future.

Table 4. Engine Field Event Analysis

Event	Cause	Notes
Crew reported aircraft yawed to right. Engine stall with flames reported to be seen from the exhaust of ENG2. Engine power level brought back to idle with normal engine indications. Flight crew elected to secure engine. Due to previous events, outstation engine change is planned. Three previous events: (vibes, high EGT, yaw), (yaw, stall, and flames), (dual channel T25 fault) .	T25 sensor	IFSD; detected potential T25 sensor problem (40° cold shift and intermittent behavior);
No event narrative available at this time	T25 sensor fault	Printed data copies
Several events on this engine; initial indications were of a "VBV position error" fault during takeoff with engine instability; next, VBV and VSV position error faults were reported; eventually VBV position and N2 errors were reported with engine surge, each time during takeoff	N2 sensor fault	In-flight surge; sensor value dropout caused VSVs to open relative to intended steady-state schedule; initially FADEC and HMU were replaced
No event narrative available at this time for three other known events; however, limited data on the event is available	N2 sensor fault	
In climb, at 6k ft, pilot observed fluctuations of 10% in N1, around 80/90% of N1. Pilot heard a compressor stall; reduced to 79% N1, no trouble for 1.5 hours. Then heard 3 or 4 compressor stalls, reduced N1 to 65%; no trouble for remainder of flight. No warning messages.	T12 sensor fault	LOTC; T12 replaced; no complaint since
Experienced several engine stalls when reducing power from takeoff to climb; rollback to 50% N1 with self recovery; performed air turnback	Unexpected dirt accumulation	Stalls during throttle reduction; high levels of deterioration; T25 compensation contributed
Air turn back at 15K ft after T/O. Stall on ENG2 without significant parameters shift. After thrust reduction all parameters were normal until landing. All equipment checked o.k. During a run the engine suffered another stall with flame out on idle.	T2 sensor fault (?)	Engine removed for test cell. No further information available yet.
Approx. 30-40 minutes after takeoff, ENG OIL FILTER message was generated. Pilot reduced power, but message remained. Engine was shut down and A/C returned to airport.	Oil filter delta pressure sensor fault	IFSD; no evidence of oil filter contamination; channel B sensor out of range; A and B channels disagree; no indicated increasing oil filter DP trend
During climb a stall was heard with some yaw. Engine N1 dropped from 104% to 92% and then recovered. Approx. 15 min.	VSV Actuator Fault	Engine sent to test cell…unable to recreate stalls.

later during climb from 30K to 31K ft another stall occurred with similar N1 drop and fireball from exhaust. IFSD performed. Troubleshooting of engine to find cause for stalls led to replacement of VSV Actuator. Data showed VSV pos faults and VSV pos drifting at time of stall.		
During climb crew noted warning ENG2 N1 overspeed. N1 reached 102.5% for 2 to 5 seconds. Second N1 overspeed occurred and engine was shutdown. N1 ENG2 Max: 112.6%; N2 ENG2 Max: 107.9%	Fuel-ECU fault	Overspeed
Engine removed for EGT temperature exceedance. Post flight report indicated "ENG2 FADEC SYS FAULT" with details of "VSV ACT/HMU" Dual Channel Fault. Airframer reports there were three warnings listed prior to this IFSD within one month.	FADEC fault	EGT exceedance
While in cruise at 39K ft, auto throttle tripped off and ENG1 accelerated to T/O power with N1 overspeed (Max N1=103.5, Duration=41min). Descended and shutdown engine. Engine cooled down and then restarted without problems. Problem isolated to ECU. Warning "ENG1 FADEC" with associated CFDS message "ECU" was set at the time of event (Dual channel PS3 also set during event). Appears to be internal ECU failure.	Fuel-ECU fault	
During decent (33K ft) auto throttle disengaged and the engine sustained an uncommanded acceleration into an overspeed condition (Max N1=102.1). Engine would not respond to throttle then shutdown. Action for this event was to replace the ECU.	Fuel-ECU fault	
ENG1 Max N1 obtained for T/O was 83%. Due to N1 shortfall rejected T/O. No faults noted. The CIT sensor had cold shifted due to a manufacturing problem. The CIT shift apparently depressed the accel schedule sufficiently to cause the engine to hang at 83% N1.	Fuel-ECU fault	CIT sensor SV findings confirmed sensor "cold shift".

4.2 Event Modeling

At the completion of the engine field event analysis one fault was selected and modeled for model-based controls and diagnostics development and demonstration purposes. The event selected was the first T25 (compressor inlet temperature) sensor fault described in Table 4 above. Further description of this fault and its modeling is described below.

First, a set of field event data files pertaining to the faulted T25 sensor case were obtained and analyzed. For this particular event there was an apparent 40°C cold shift in the T25 measurement on the #2 engine. Actual data files from the flight were provided and used for analysis. The T25 measurement 40-degree cold shift caused the engine to stall and as a result the pilots were forced to perform an IFSD. This engine had experienced three faults (events or maintenance messages) within the previous month. The first occurrence was when the engine stalled during climb and began to eject flames, which forced the crew to bring the throttle to idle. The second occurrence was when maintenance reported a dual channel T25 fault, but the next day the T25 resistance checked OK on both channels. The third engine fault was when once again during climb the engine stalled and flames were seen coming from the exhaust. Upon analysis PSE was able to indicate a T25 sensor problem (40° cold shift). It was later determined that in addition to or instead of a constant 40° cold shift, the sensor value was fluctuating intermittently.

The T25 sensor provides a measurement that is essential in the calculation of the corrected core speed. As shown in the equation below, corrected core speed (N2R) is calculated based on the measured core speed (N2), the measured compressor inlet temperature (CIT or T25), and the measured inlet temperature (T2 or T12).

$$N2R = \frac{N2}{\sqrt{T25/T2}}$$

As a result of the T25 fluctuations, corrected core speed was also fluctuating. Because N2R is used in the VSV scheduling, the VSV position changed rapidly, causing a loss in compressor stall margin.

Originally it was thought that modeling the T25 sensor with a 40-degree cold shift would simply involve adjusting the temperature output of the sensor by –40°C. After meeting with PSE engineers it became apparent that it was necessary to force the signal coming from the T25 sensor to fluctuate, a fact that was not immediately apparent from the data that was available at the time. Figures 59, 60 and 61 show the flight conditions from one of the events. Figure 59 plots the aircraft altitude, Figure 60 plots the aircraft Mach Number, and Figure 61 plots the aircraft Power Lever Angle (PLA), also known as the aircraft throttle angle.

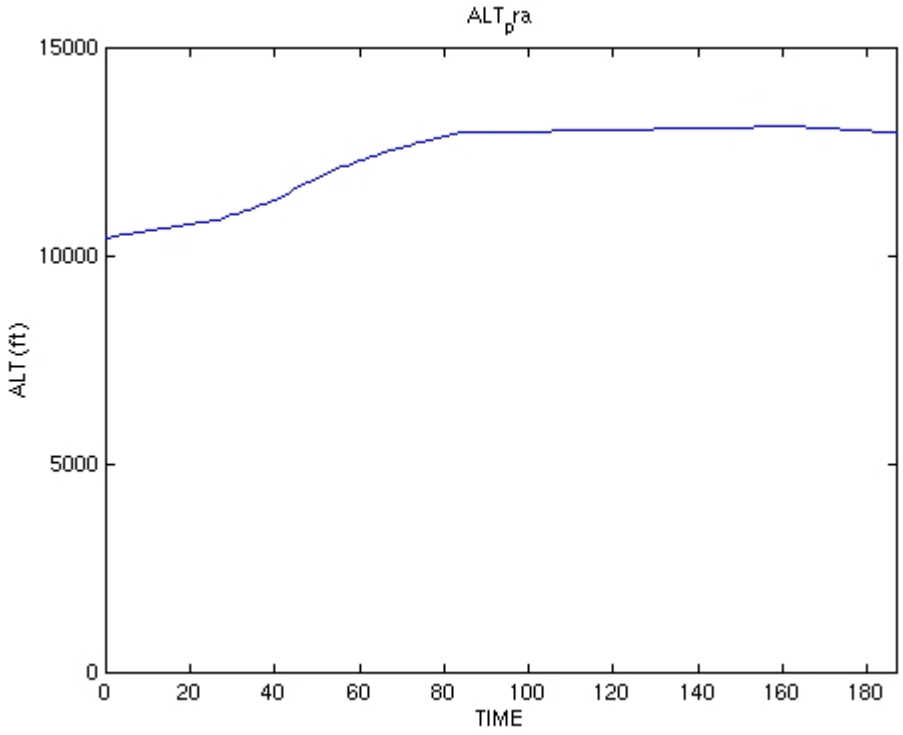

Figure 59. Aircraft Altitude During Faulty T25 Event

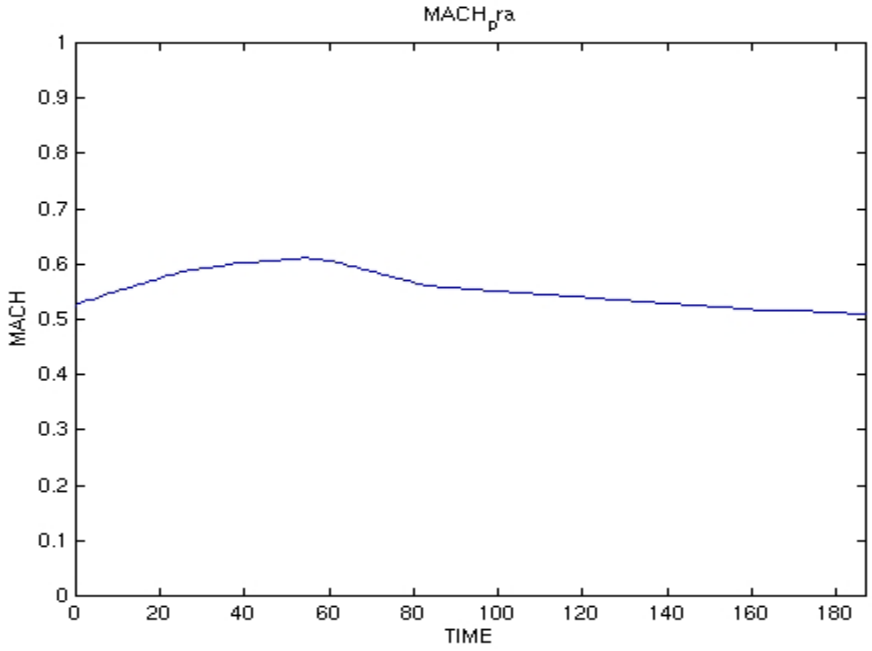

Figure 60. Aircraft Mach Number During Faulty T25 Event

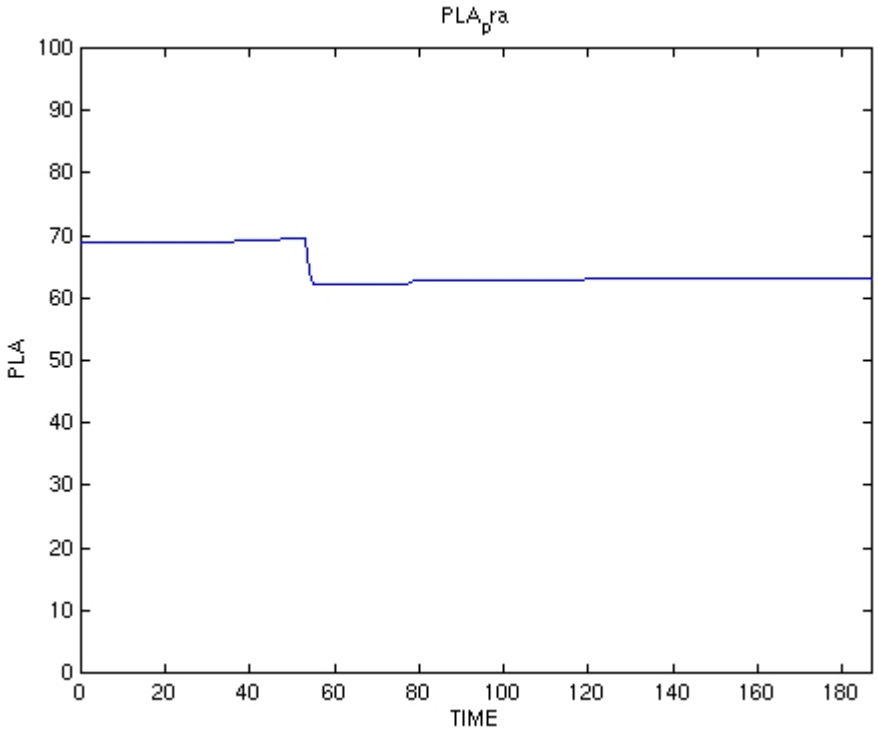

Figure 61. Aircraft Power Lever Angle During Faulty T25 Event

Figure 62 shows data for the T25 sensor on each engine of the aircraft. Data from the good T25 sensor installed on Engine 1 is shown in green and data from the faulty T25 sensor installed on Engine 2 is shown in blue.

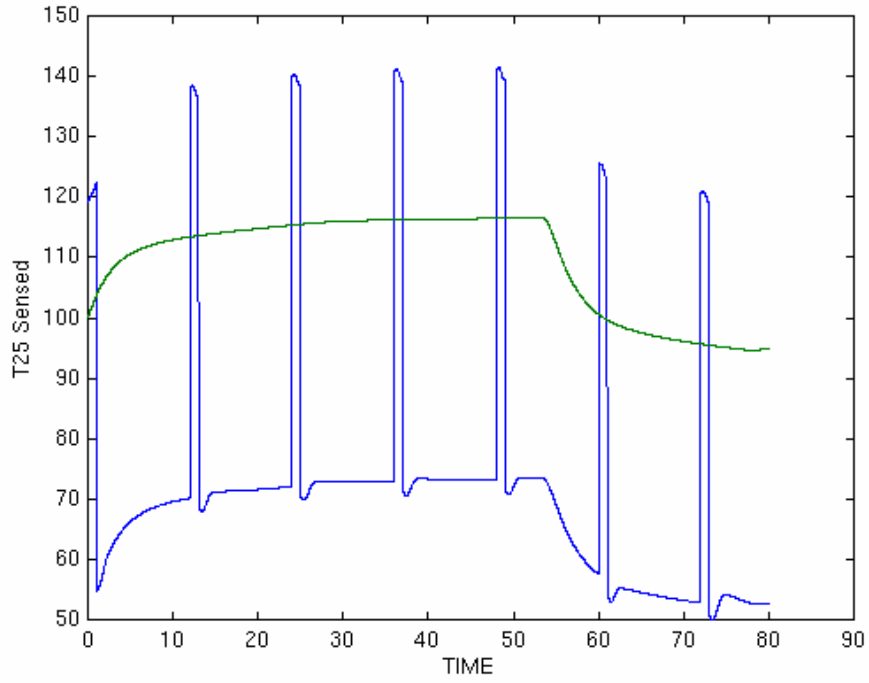

Figure 62. T25 Signals from Engine 1 and Engine 2 During Faulty T25 Event

Finally, Figure 63 shows the resulting core stall margin on an engine with a good T25 sensor (Eng 1) vs. a faulty T25 sensor (Eng 2).

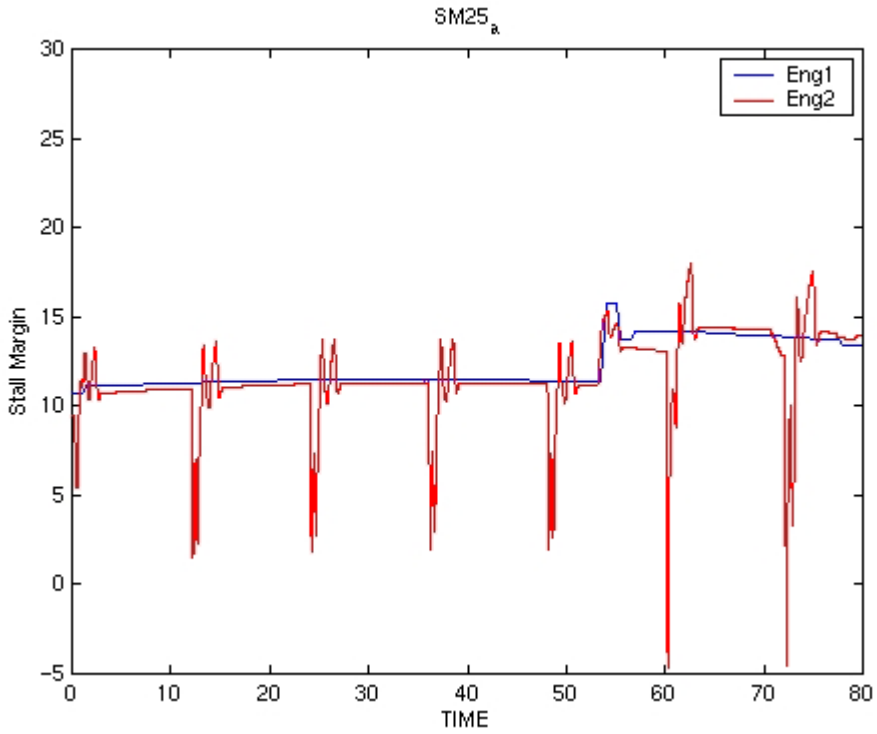

Figure 63. Stall Margin Calculations for Engine 1 with Good T25 sensor and Engine 2 with Faulty T25 Sensor

These plots show that core stall margin may drop significantly when a T25 sensor fault goes undetected. There were many opportunities in this profile for the core to stall before 50 seconds; for example, a crosswind gust coinciding with a drop in stall margin could have combined to cause a stall. At 60 seconds, the stall margin actually drops below zero, indicating a stall (although this is not reflected in the model data after 60 seconds). Some liberty has necessarily been taken in recreating this event.

4.3 Accommodation Strategy

The fault accommodation strategy developed under Aviation Program (Phase I) was based on correlation analysis of Compressor Stall Margin (SM25) and various significant engine parameters such as rotor speeds, temperatures and pressures. Results of this analysis are shown in Figure 64.

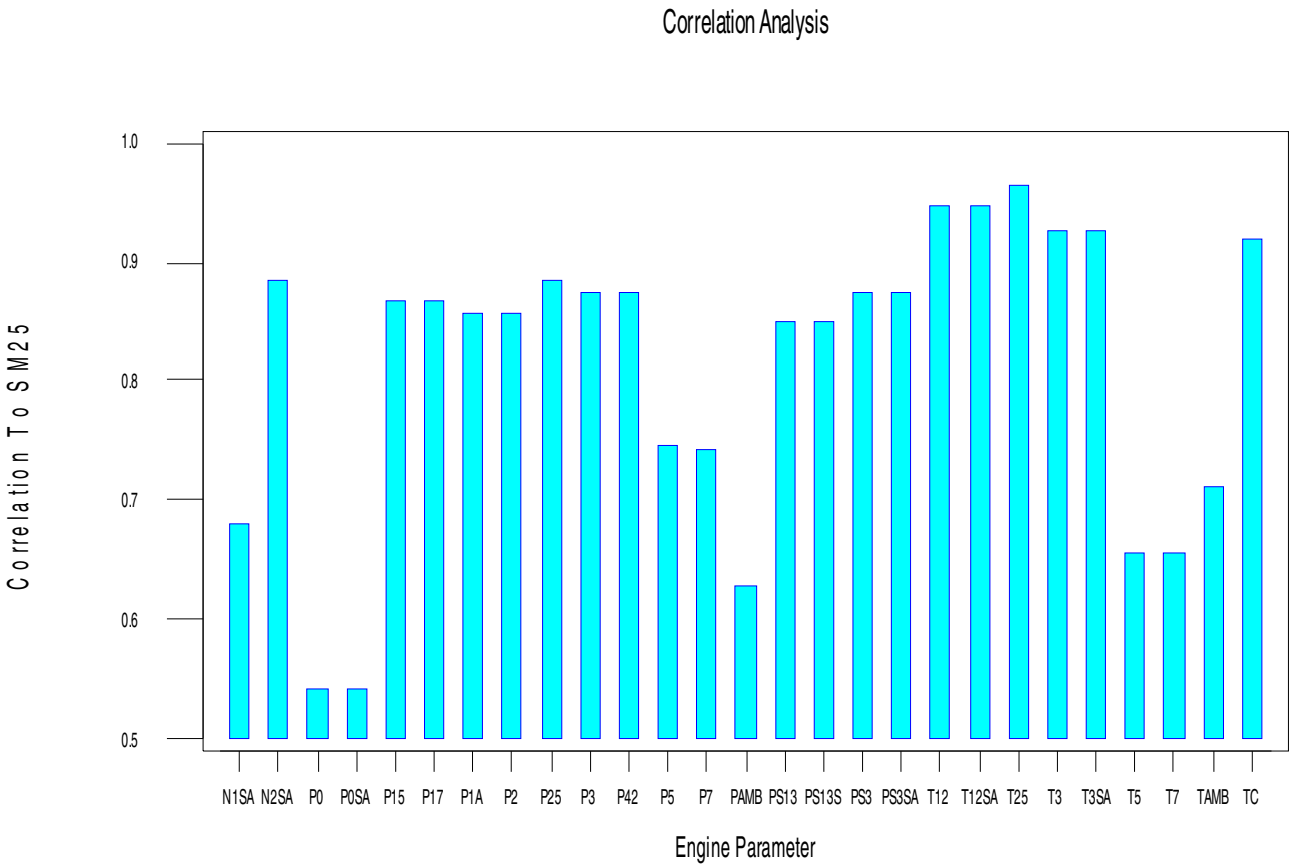

Figure 64. Correlation Analysis of Compressor Stall Margin & Engine Parameters

This analysis established a strong correlation between the compressor stall event and the corresponding CIT (T25) sensor fault in the field event. The correlation analysis was based on 500 simulated engine data points for engine parameters.

The Model-Based Fault Accommodation strategy then focused on generation of a simple T25 sensor model, which would be used to schedule compressor VSVs, in the case of an actual fault in the T25 sensor. The set of independent parameters for the T25 sensor model were chosen based on the correlation analysis of Compressor Inlet Temperature (CIT or T25) and other available sensor parameters. Various combinations of Rotor speeds (N1 and N2), Fan Inlet Temperature (T12), Compressor Exhaust Temperature (T3) and a Bias term were used to generate numerous Linear Regression Models (LRMs) for the CIT sensor. The results of the T25 correlation analysis are shown in Figure 65 and the resulting LRMs are shown in Table 5.

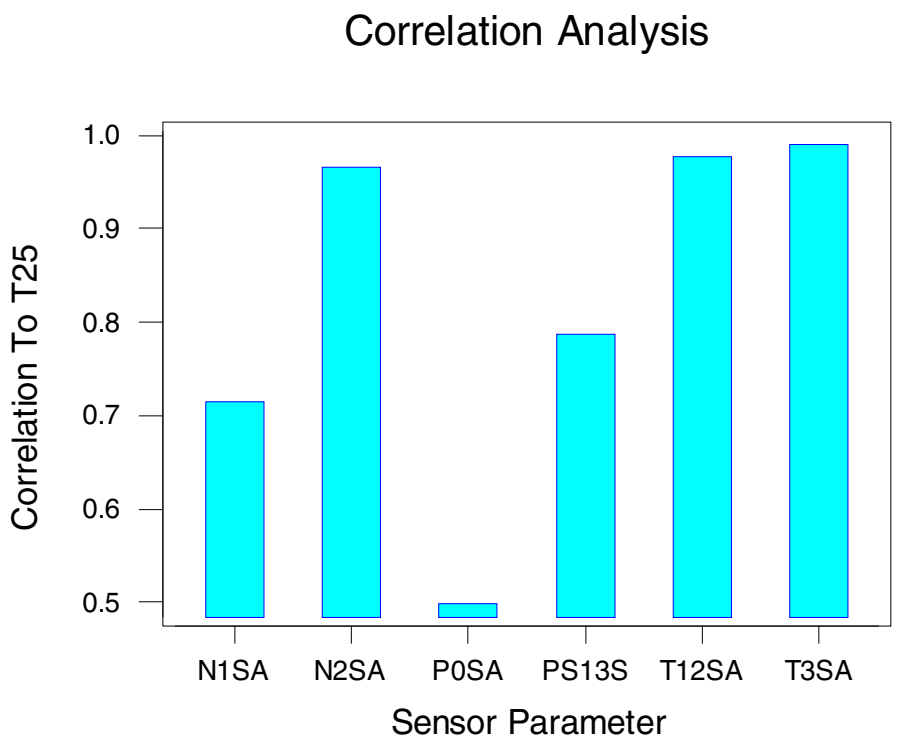

Figure 65. Correlation to T25 for Various Regressor Variables

Table 5. Linear Regression Models for T25 Sensor

Regressor Number		Regressor Variables				Gain Matrix (10 Engines)
1	T12SA	T3SA				[0.8016 0.1637]
2	T12SA	T3SA	Bias			[0.3675 0.495 -138.1369]
3	T12SA	T3SA	N1SA	N2SA		[0.9098 0.121 0.0234 -0.0054]
4	T12SA	T3SA	N1SA	N2SA	Bias	[0.9988 -0.099 0.0367 0.0075 -143.587]
5	T12SA	T3SA	N2SA			[0.499 0.505 -0.0101]
6	T12SA	T3SA	N2SA	Bias		[0.4423 0.504 -0.0061 -56.6634]
7	T12SA	T3SA	N1SA			[1.3507 -0.2947 0.0475]
8	T12SA	T3SA	N1SA	Bias		[0.8665 0.0933 0.0253 -72.3932]

4.4 Accommodation Strategy Implementation and Simulation

LRM use for fault accommodation was evaluated in a simulation environment by replacing the faulty measured feedback control value of T25 with an LRM generated estimate of T25. All eight LRMs shown in Table 5 were found to produce estimations of T25 with suitable accuracy for accommodation of the intermittent T25 sensor fault. A set of sample simulation results using the LRM # 4 in the table above is shown below. The LRM for T25 is represented as:

$$T25 = 0.9988\ T12SA - 0.099\ T3SA + 0.0367\ N1SA + 0.0075\ N2SA - 143.57$$

Figure 66 shows time histories of fan stall margin (SM12) for the cases of 1) no fault, 2) a faulted T25 measurement used for feedback control, and 3) a faulted T25 measurement accommodated via the LRM #4 generated estimate. Figure 67 shows the same information for compressor stall margin (SM25). The accuracy of the LRM is illustrated by the close agreement between the no fault and the accommodated fault cases. It should be noted that the accommodation results presented here do not include fault detection and isolation logic. Rather it is assumed that the T25 sensor fault has been correctly detected and isolated, and these results are the accommodated results using the LRM estimated value of T25 for feedback control.

4.5 Model-Based Fault Tolerant Control Results

The results of the model-based fault tolerant control task revealed several findings. The field event study demonstrated that there are various root-causes for in-flight engine shutdowns, loss of thrust control, and aborted takeoff events. In some cases a stack-up of events contribute to the overall problem as was the case for the T25 sensor fault analyzed in this report which consisted of sensor bias, intermittent sensor behavior, and a degraded engine condition all of which combined to result in an engine surge event. The model-based fault tolerant control approach is particularly well suited to address gas-path faults such as sensor faults, actuator faults, moderated gas-path damage, or a combination of these events. The Linear Regression Model (LRM) accommodation results illustrated the analytical redundancy contained within the available gas path measurements and the potential benefits of model-based fault tolerant control for fault accommodation.

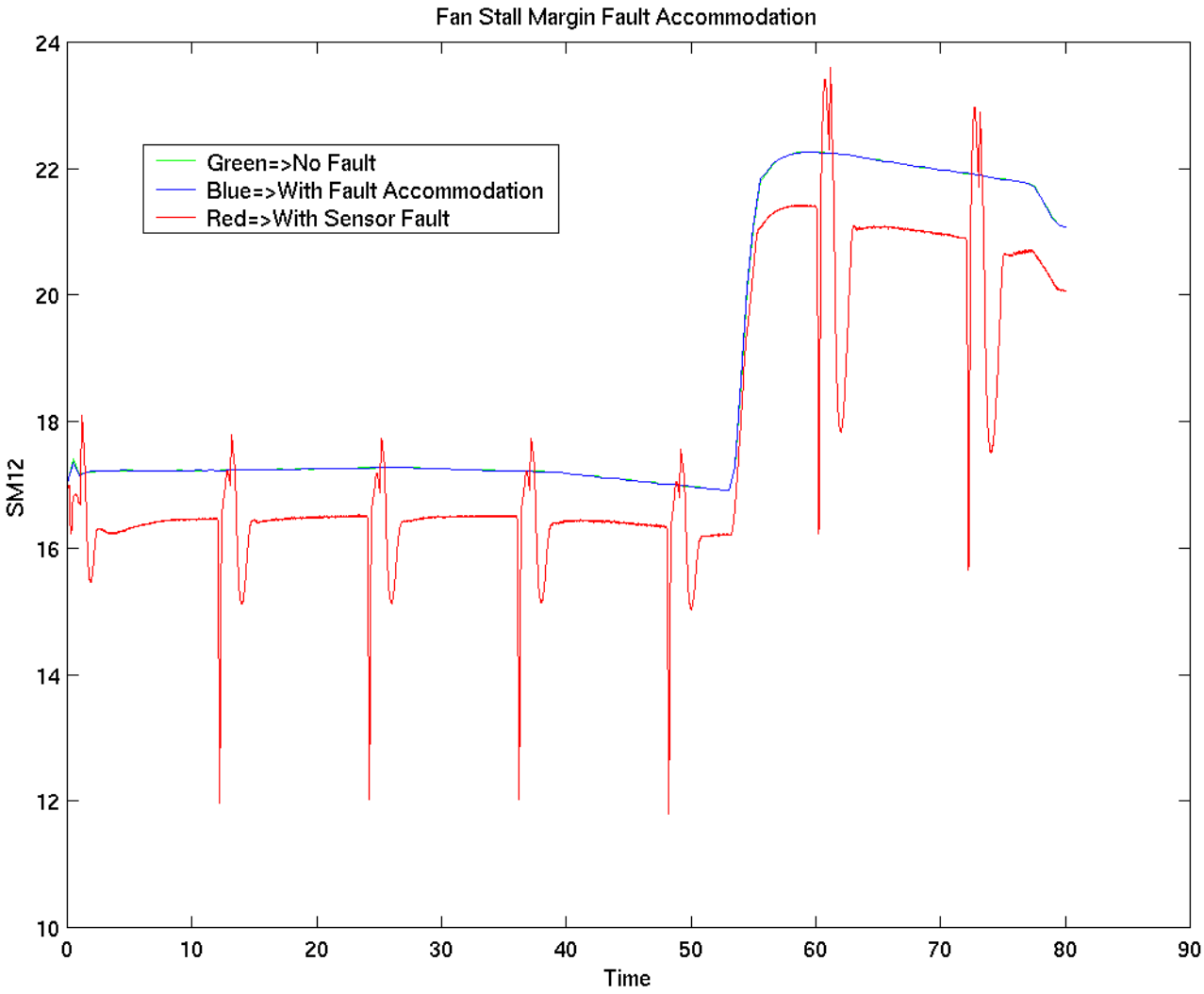

Figure 66. Fan Stall Margin Fault Accommodation Using LRM #4

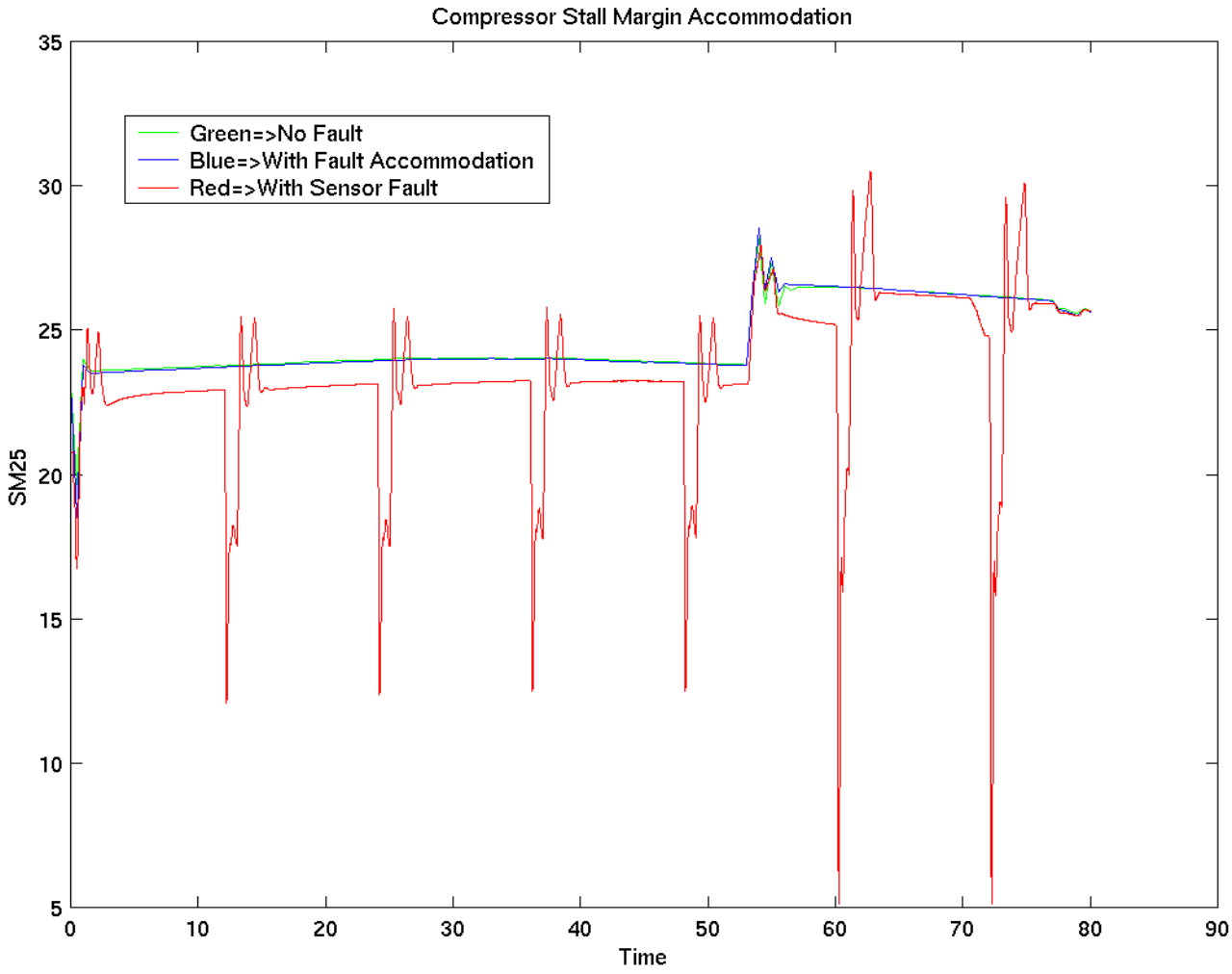

Figure 67. Compressor Stall Margin Fault Accommodation Using LRM #4

Conclusions and Future Work

The GE GR radial-mode disk crack detection system was tested on a sub-scale model turbine disk and a full-scale turbine disk to evaluate its ability to detect the presence of seeded disk cracks. Although successful crack detection was not demonstrated, several important lessons were learned. The disassembly and reassembly of the hardware necessary to artificially machine a crack into the disk introduced a significant variation in the baseline vibration response of the system. Since the crack detection system monitors for a shift in the vibration unbalance signal relative to a pre-established baseline, the disassembly/reassembly process would introduce a variation that would mask any contribution due to the crack contained in the accelerometer measurements. However during the baseline tests of the full-scale turbine disk, it was demonstrated that the residual disk unbalance vibration signature was repeatable within individual hardware re-builds. This information was important since the intended use of the disk crack detection algorithm is within an actual engine operating environment. Here the residual disk unbalance of an engine is not expected to change during normal operation allowing an initial baseline vibration signature to be established. Then if a disk crack were to initiate in the future, there would be a higher probability of the crack detection system successfully detecting the crack. In order to confirm this, the GE GR crack detection algorithm was selected to participate in a follow-on effort under the NASA Aviation Safety Program which includes evaluating the technology as part of a NASA/FAA/DoD engine test scheduled for the fall of 2002. During this test, the engine will be cycled until a small crack machined in the fan disk propagates to failure.

The PSU ARL torsional-mode disk crack detection system was demonstrated on a full-scale turbine disk test as part of this NASA Aviation Safety Phase I Program. There is no further development work planned for this technology at this time.

The work performed by GE AE in this NASA Aviation Safety Program contract demonstrated the concept of Model Based Fault Tolerant Control for a single sensor fault. This work is being enhanced in a follow-on effort under the NASA Aviation Safety Program to develop MBFTC technology to accommodate sensor, actuator and gas path faults such as high pressure turbine and compressor damage.

References

1. Thomson W.T. and Dahleh, M.D., *Theory of Vibration with Applications*, 5th Ed., Prentice-Hall, Englewood Cliffs, New Jersey (1998).

2. Cook R.P., Malkus D.S. and Plesha, M.E., *Concepts and Applications of Finite Element Analysis*, 3rd Ed., John Wiley and Sons, Inc., New York (1989).

3. Imam, I. and DeLorenz, H.G., *Method and Applications for Detecting Axial Cracks in Rotors for Rotating Machinery*, U.S. Patent 4,751,657 (1988).

4. Tada H., Paris P. and Irwin, G., *The Stress Analysis of Cracks Handbook*, 2nd Ed., Del Research Corp., St. Louis, Missouri (1985).

5. NASA TM X-73307, *Astronautics Structures Manual, Vol. III* (1975).

6. ISABE XV Conference Paper "A Physics-Based Approach for the Detection of Cracks on Rotating Disks" presented on September 5, 2001

7. Naval Air Warfare Center Aircraft Division, Patuxent River, Maryland Letter of Test Results "NASA Crack Detection Evaluation Test Program" dated April 10, 2002.

8. Design Review Presentation for NASA Spin Pit Interface to CFM56 HPT Rotor Assembly made on November 30, 2000

9. Test Project Sheet titled "Spin Rig Testing of High Pressure Turbine Assembly: dated October 25, 2001.

REPORT DOCUMENTATION PAGE

Form Approved
OMB No. 0704-0188

1. AGENCY USE ONLY (*Leave blank*)	2. REPORT DATE	3. REPORT TYPE AND DATES COVERED
	June 2003	Final Contractor Report

4. TITLE AND SUBTITLE

Propulsion Health Monitoring for Enhanced Safety

5. FUNDING NUMBERS

WBS–22–708–30–05
NAS3–99203

6. AUTHOR(S)

Mark G. Butz and Héctor M. Rodríguez

7. PERFORMING ORGANIZATION NAME(S) AND ADDRESS(ES)

General Electric Aircraft Engines
One Neumann Way
Cincinnati, Ohio 45215

8. PERFORMING ORGANIZATION REPORT NUMBER

E–13853

9. SPONSORING/MONITORING AGENCY NAME(S) AND ADDRESS(ES)

National Aeronautics and Space Administration
Washington, DC 20546–0001

10. SPONSORING/MONITORING AGENCY REPORT NUMBER

NASA CR—2003-212291

11. SUPPLEMENTARY NOTES

Mark G. Butz, General Electric Aircraft Engines, Cincinnati, Ohio 45215; Héctor M. Rodríguez, General Electric Global Research Center, Niskayuna, New York, 12309. Project Manager, Donald L. Simon, U.S. Army Research Laboratory, NASA Glenn Research Center, organization code 0300, 216–433–3740.

12a. DISTRIBUTION/AVAILABILITY STATEMENT

Unclassified - Unlimited
Subject Category: 07 Distribution: Nonstandard

Available electronically at http://gltrs.grc.nasa.gov

This publication is available from the NASA Center for AeroSpace Information, 301–621–0390.

12b. DISTRIBUTION CODE

13. ABSTRACT ***(Maximum 200 words)***

This report presents the results of the NASA contract "Propulsion System Health Management for Enhanced Safety" performed by General Electric Aircraft Engines (GE AE), General Electric Global Research (GE GR), and Pennsylvania State University Applied Research Laboratory (PSU ARL) under the NASA Aviation Safety Program. This activity supports the overall goal of enhanced civil aviation safety through a reduction in the occurrence of safety-significant propulsion system malfunctions. Specific objectives are to develop and demonstrate vibration diagnostics techniques for the on-line detection of turbine rotor disk cracks, and model-based fault tolerant control techniques for the prevention and mitigation of in-flight engine shutdown, surge/stall, and flameout events. The disk crack detection work was performed by GE GR which focused on a radial-mode vibration monitoring technique, and PSU ARL which focused on a torsional-mode vibration monitoring technique. GE AE performed the Model-Based Fault Tolerant Control work which focused on the development of analytical techniques for detecting, isolating, and accommodating gas-path faults.

14. SUBJECT TERMS	15. NUMBER OF PAGES
Aircraft engines; General aviation aircraft; Systems health monitoring; Flight safety	81
	16. PRICE CODE

17. SECURITY CLASSIFICATION OF REPORT	18. SECURITY CLASSIFICATION OF THIS PAGE	19. SECURITY CLASSIFICATION OF ABSTRACT	20. LIMITATION OF ABSTRACT
Unclassified	Unclassified	Unclassified	